The official bi-monthly publication of Bhabha Atomic Research Centre

# BARC newsletter

May-June 2023 ISSN: 0976-2108

- Thermal Reactors
- Genetic Algorithm
- Picosecond laser
- Radionuclide Therapy

25 years of Operation Shakti
heralding a new era in the spirit of
Atoms for Peace


**BARC Newsletter**
**May-June 2023**
**ISSN: 0976-2108**

G20 भारत 2023 INDIA

INTERNATIONAL YEAR OF MILLETS 2023

editorial

# *Heralding a new era in the spirit of Atoms for Peace*

India - a nation blessed with a huge aspiring population - time immemorial has made no secret of its wish to take centre stage for safeguarding the interests of global commons. As a matter of policy, soon after becoming an independent nation, India crafted the policy of state-controlled planned economy with science and technology playing a pivotal role for ushering in an era of equitable national development.

"In a broad view of human history, it is possible to discern three great epochs. The first is marked by the emergence of the early civilizations....., the second by the industrial revolution ... and the third by the discovery of atomic energy and the dawn of the atomic age... Each epoch marks a change in the energy pattern of society," Dr. Homi J. Bhabha said in his presidential address to the maiden UN Conference on Peaceful Uses of Atomic Energy in Geneva, 1955.

Around the dawn of the new century, India proactively demonstrated its nuclear technology prowess, which characterised its true aspiration to position itself as an equal and responsible partner in transforming the course of mankind towards shared prosperity and peaceful coexistence.

The series of nuclear tests conducted on May 11$^{th}$ and 13$^{th}$ in 1998, under the Operation codenamed 'Shakti,' was a testament to India's growing stature as a global power having advanced scientific and technological knowhow. Decades of restrictions imposed on the country over sharing of nuclear technologies did not deter its forward march albeit provided necessary impetus for achieving greater indigenization in wide spectrum of sophisticated technologies.

Countries which initially stood in disagreement over India's new coveted status, soon acknowledged the country's uncompromisingly strong nuclear non proliferation record to strike an "enduring" relationship. The diplomatic efforts that followed soon after the successful nuclear tests played a positive role in resetting India's relationship with the technologically superior West.

Years of painstaking efforts by nuclear energy fraternity amid difficult conditions, finally paved way for forging new partnerships with the West for broad based tech sharing and co-development. India is now an active member of all major international bodies that work to address non proliferation of sensitive technologies having military applications, such as the Missile Technology Control Regime (MTCR), the Wassenaar Arrangement, and the Australia Group. It secured a country-specific waiver from the Nuclear Suppliers Group (NSG) in 2008.

India's science and technology landscape has clocked many unique feats in the last more than 25 years. New reactors coming up in fleet construction mode in the next decade-and-a-half period with the active involvement of private sector would ensure significant expansion in nuclear energy capacity generation within the country. The incremental growth in capacity would mostly come from indigenously developed 700 MWe capacity pressurized heavy water type reactors (PHWRs).

The Bhabha Atomic Research Centre (BARC), through its strong multidisciplinary R&D culture, continues to play a pivotal role in the expansion of nuclear energy and allied activities in the country. This issue of newsletter presents newer outcomes from a range of R&D works in BARC. We take this opportunity to thank everyone for their committed efforts that contributed positively to the preparation and timely release of this issue of newsletter.

# *From the Annals of History... *From the Annals of History...

## Text of Vajpayee's letter to Clinton

Dear Mr President,

You would already be aware of the underground nuclear tests carried out in India. In this letter, I would like to explain the rationale for the tests.

I have been deeply concerned at the deteriorating security environment, specially the nuclear environment, faced by India for some years past. We have an overt nuclear weapon state on our borders, a state which committed armed aggression against India in 1962. Although our relations with that country have improved in the last decade or so, an atmosphere of distress persists mainly due to the unresolved border problem. To add to the distress that country has materially helped another neighbour of ours to become a covert nuclear weapons state. At the hands of this bitter neighbour we have suffered three aggressions in the last fifty years. And for the last ten years we have been the victim of unremitting terrorism and militancy sponsored by it in several parts of our country, specially Punjab and Jammu & Kashmir. Fortunately, the faith of the people in our democratic system as also their patriotism has enabled India to counter the activities of the terrorists and militants aided and abetted from abroad.

The series of tests are limited in number and pose no danger to any country which has no inimical intentions towards India. We value our friendship and cooperation with your country and you personally. We hope that you will show understanding of our concern for India's security.

I assure you that India will continue to work with your country in a multilateral or bilateral framework to promote the cause of nuclear disarmament. Our commitment to participate in non-discriminatory and verifiable global disarmament measures is amply demonstrated by our adherence to the two conventions on biological and chemical weapons. In particular we are ready to participate in the negotiations to be held in Geneva in the conference on disarmament for the conclusion of a fissile material cut-off treaty.

I enclose for your information the text of the press statement issued after the nuclear tests were carried out today. I close with the expression of my highest consideration for your

Yours sincerely,

A-BOMB CLUB

I REALISE YOU'RE MAKING THE WORLD AN UNSAFE PLACE ?!?

## The Indian Express

newspapers and, barring New York Post, condemned by most

## Indians overseas swell with patriotic pride over nuclear tests

## "Indian scientists are t

## People from all quarters hail nuclear tests

## Buddha smiles once again after 24 years, but this time more powerfully

## NRIs HAIL N-TESTS

'Govt is the best judge in matters concerning security matters'

भारत की दलील संतुष्ट, सहयोग

HEY, YOU KNOW THE ORDER AROUND HERE! NOW YOU WILL HAVE TO FACE SEVERE PUNISHMENT!

NO SMOKING

'Post-Pokhran India needs to be taken more seriously as eco power'

best in the world"

Courtesy of "The Asian Age, The Financial Express, The Indian Express, The Times of India, Navbharat Times (Hindi) and The Observer"

**“India considers technology as a tool of the nation’s progress, not a means to assert its dominance*.**

*Prime Minister of India Shri Narendra Modi said during his address on the occasion of National Technology Day 2023

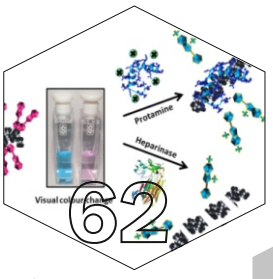


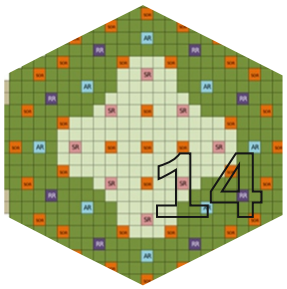


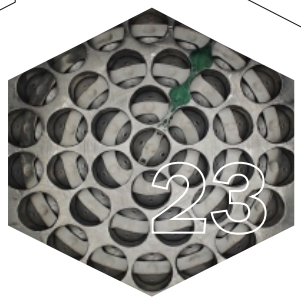


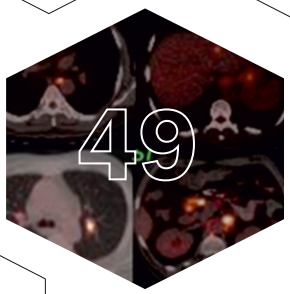

# CONTENTS








**FORTHCOMING ISSUE**

## Applications of CFD in Chemical Engineering, Materials Science and Safety

- **Hydrogen Recombiner - Benchmarking & Performance Evaluation.**
- **Artificial Compressibility Method for Incompressible Flow Solver.**
- **Safety Evaluation for Nisargruna Biogas Plant - Fire, Explosion & Toxicity.**
- **Numerical Simulations to Understand & Evaluate Spread of Aerosols.**
- **Short notes on journal articles published in CFD domain by BARC.**

This page intentionally left blank

# Nuclear Reactors

1

# Physics of Thermal Reactors: Excitements and Challenges

**Umasankari Kannan***

*Reactor Physics Design Division, Bhabha Atomic Research Centre, Trombay – 400085, INDIA*

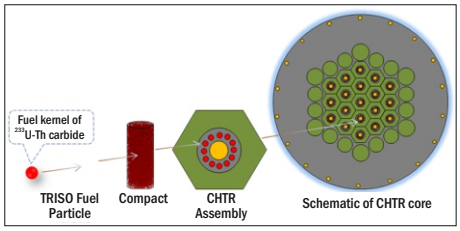


*Schematic of fuel particles and the CHTR core*

ABSTRACT

Physics of reactors is exciting and engaging due to its multi-disciplinary nature. Probing the nucleus has unleashed the potential of the atom and the role of the fascinating neutral particle-the neutron! The understanding of the complex phenomena of energy transfers within the nucleus along with the interplay of the isolated neutron, has thrown open several opportunities for energy generation. The discovery of fission chain reaction was a great Eureka moment for the world and this idea has been successfully exploited. As we look back at the 80 years since the Chicago Pile, we have come a long way and successfully designed and operated several types of nuclear reactors. Of the total power reactors in the world, more than 90% is based on thermal neutron energy spectrum. The physics characteristics of thermal reactors are governed by the complex neutron transport in a scattering medium to achieve the desired neutron spectrum. The new generation reactors usually have to cater to four major aspects i.e. sustainability, better fuel utilization, inherent safety and better economics. This article aims to run through the design challenges in these new reactor designs where advanced fuels are used to achieve the objectives listed above and the neutron spectrum is tuned to achieve higher a degree of safety. Thus, we must use newer materials and traverse through uncharted regimes. This article is kept simple to make even readers from other fields also to appreciate these features of physics of reactors.

KEYWORDS: *Thermal reactors, PHWR, Nuclear fission, Gen-IV reactors, MSBR, Thorium, IPWR*

## Introduction

Currently, there are 449 power reactors operating in the world, of which more than 350 are Light Water Reactors (LWRs) [1]. Out of these, 306 are Pressurised Water Reactors (PWR) and 56 are the boiling water type BWRs. These constitute about 81% of the total operating reactors. There are 50 reactors using heavy water and are called Pressurised Heavy Water Reactors (PHWRs). Reactors based on fast spectrum constitute about 12% The different types of reactors operating in the world are shown in Fig.1. India currently has 19 PHWRs, 2 PWRs and 2 BWRs and considerable experience has been gained in operation, design, and safety of all the thermal reactor types.

Uranium-235 is the only fissile material available in nature and has been exploited for power production. The fission of U-235 with thermal neutrons is the workhorse of most of the reactors operating in the world. The basic physics is governed by the achievable neutron spectrum and the behavior of neutron interactions in the energy and space domains of interest. The interplay of all the emitted particles with the different materials in a reactor result in more complex behavior. Thus, the modelling of the physical phenomena will have to be very realistic and as accurate as possible.

The major objectives of current generation nuclear reactors are better fuel utilization, enhanced safety and economics of power generation. The neutronics is also interlinked with heat removal and other engineering aspects such as selection of materials, irradiation behavior, radiological assessment, fuel cycle and final safe disposal [2]. This article will attempt to detail the challenges in reactor design encompassing all these multiple stages of nuclear energy production.

*Author for Correspondence: Umasankari Kannan
E-mail: uma_k@barc.gov.in

## Today's Designs

In its GEN-IV forum, IAEA has focused on several types of reactors with Molten Salt Breeder Reactor (MSBR), Super Critical Water Reactor (SCWR) and Very High Temperature Reactor (VHTR) as potential thermal reactor designs [3]. Sodium and lead cooled fast reactor designs are also considered. The objectives for all these types of reactors have also been lucidly elaborated. Molten salt Breeder reactor is designed to use thorium-based fuel where the nuclear properties of the bred U-233 can be efficiently used for power production in a breeder configuration. With the engineering advances in using super critical water as coolant, the fuel

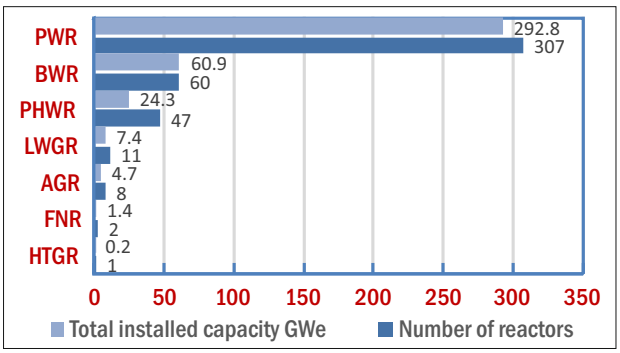


*Fig.1: Operating reactors in the world by their types. https://www.world-nuclear.org*

*Table 1: Comparison of fuel utilization of thermal reactors.*

| Reactor Type | Reactor Power Electric / Thermal / Fission (MW) | Feed enrichment in equilibrium cycle (%) | Discharge Burnup Gwd / Te | Cycle length | Equivalent mined uranium Tonne / Twhr (e) |
|---|---|---|---|---|---|
| BWR | 1330/ 3990/ 4070 | ~2.4 | 22.0 | 24 months | 25.0 |
| PWR | 1280 / 3800 /3900 | ~3.3 | 33.0 | 12 months | 23.38 |
| VVER | 1000 /3000 /3150 | ~3.92 | 43.0 | 295 days | 22.26 |
| PHWR -220 | 220/750/802 | 0.71 | 6.7 | On power fuelling | 22.67 |
| PHWR -540 | 540/1760/1830 | 0.71 | 7.0 | On power fuelling | 20.17 |

utilization can be enhanced again by exploiting the uranium and water combination to achieve an effective neutron spectrum. Very high temperatures are required to use the process heat to disassociate water. The high temperature reactors design with gas cooled or liquid metal cooled offer themselves as good candidates for hydrogen production. It is once again emphasized that the physics of these reactors are very different and the challenge is to design systems with a prudent choice of fuel and material composition to achieve the desired objectives.

BARC is engaged in design of advanced reactors based on thorium utilization such as Advanced Heavy Water Reactor (AHWR) and Molten Salt Reactors (MSR) and High Temperature Reactors (HTR) for hydrogen production [3]. An advanced light water reactor IPWR based on enriched uranium for longer operating cycle is also being developed. As mentioned earlier, the physics of these systems are challenging and mostly must balance the competing objectives. For example, the active length of fuel in AHWR and power distribution in the core had to be optimised for effective heat removal through natural circulation. In an MSR, the fuel and coolant being liquid requires a different approach for simulation of near homogenous systems and achieve effective heat removal and take care of radiological aspects throughout the core and design associated engineered systems. To achieve breeding through online refuelling requires management of constant excess reactivity throughout the burnup or operating cycle. MSRs also advocate use of advanced materials to arrest corrosive nature of these molten salt mixtures. Advanced LWR designs on the other hand are looking towards enhanced fuel utilisation or longer cycle lengths which is achieved by high strength fuel clad materials for higher burnups. Advanced CANDU reactors have addressed the undesirable feature of positive void coefficient issue with ingenious fuel design and interleaving of coolant channels.

### *Comparison of fuel utilization*

The parameters defined by the Gen-IV international forum are fuel utilization, margin of safety, proliferation resistance. As an important design feature, fuel utilization can be compared for all reactors by estimating the energy produced per unit mass of fuel. In Table 1, few currently operating thermal reactors are compared on an equal footing of equivalent mined uranium[a] required to produce energy of 1 Terrawatt-hr (e) [4]. The lower the mined uranium required,

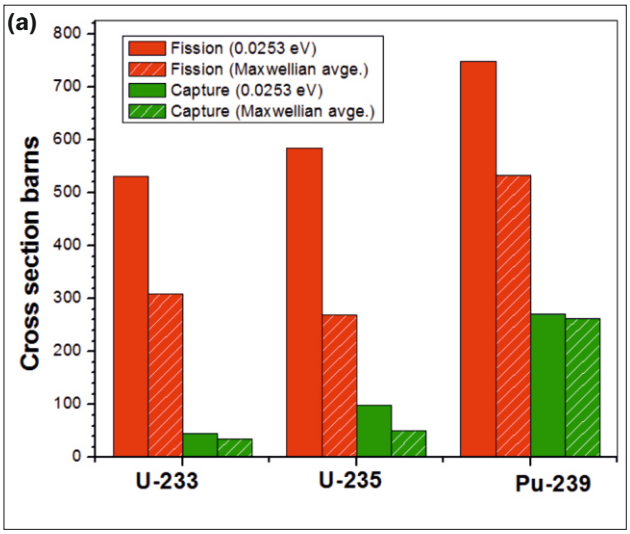


*Fig.2 (a): Comparison of fission and capture cross section of U-233, U-235 and Pu-239 at thermal energies.*

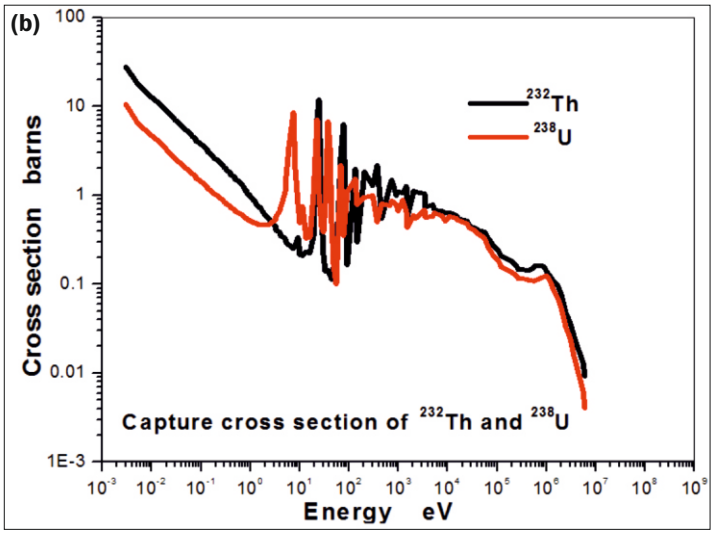


*Fig.2 (b): Energy dependence of capture cross section of Th-232 and U-238.*

[a]*Equivalent mined uranium for any reactor or fuel cycle is defined as the amount of uranium required to produce 1 TWhr (e) of electricity considering 0.2% enrichment tails.*

the better would be the fuel utilization. Another quantity, fissile inventory ratio (FIR) can also be defined which gives an idea of how the fissile content has burnt and gives a measure of remaining fissile content in the discharged fuel which also includes conversion and production of other fissile material usually Plutonium in the Uranium fuelled reactors. It is defined as the amount of fissile content in discharged fuel to that in the initial fuel. The FIR is about 0.72 for a PHWR at discharge of 7.0 GWd/Te and 0.35 for a PWR at a discharge of 45 GWd/Te [5].

It can be seen from Table 1 that PHWRs give the best fuel utilization with respect to mined uranium. In water cooled reactors, which use enriched uranium, energy is required to enrich the uranium too.

### *Fuel cycle and fuel performance*

The fissile isotope/nuclide available in nature is U-235 and constitutes 0.71 % in weight in natural uranium. Pu-239 and U-233 can be produced in reactors by neutron interactions. The basic neutronic cross section[b] of three fissile isotopes are compared in Fig.2a. Pu-239 and U-233 have higher cross section in thermal/Maxwellian spectrum and so advanced fuel cycles are based on U-Pu or Th-U233 fuel. In Fig.2b, the neutron capture cross section of the fertile species or precursor to the fissile isotope i.e. U-238 and Th-232 is compared. The Capture-to-Fission ratio is least in U-233 in thermal energies and fission contribution is larger than U-235. This means that U-233 is the best fuel in thermal spectrum reactors.

Eta (η) is the regeneration factor[c] which is measure of how many neutrons are produced in a fission reaction. The spectrum dependent eta values are compared for fissile nuclides in Table 2. In order to aid to fissile breeding, this factor should be greater than 2.0 in the reactor spectrum. Fig.3 shows the plot of eta (η) as a function of energy for the three types of fissile nuclides, namely, U-233, U-235 and Pu-239. Here again it is seen that U-233 has a flat characteristic throughout the complete energy range. In thermal spectrum U-233 has the highest eta (η) and this should be exploited for in-situ conversion or breeding [4]. It also goes to say that Pu-239 is the best option for fast reactors.

The fuel and spectrum are chosen based on these physical properties and used to design reactors for better fuel utilization. A few thermal reactor designs are compared in

*Table 2: Fissile requirement in thermal reactors.*

| Reactor Type | BWR* (1330 MWe) | PWR* (1300 MWe) | PHWR* (600 MWe) |
|---|---|---|---|
| **Fuel** | Enriched $UO_2$ | Enriched $UO_2$ | Natural $UO_2$ |
| **Fuel loading (Heavy Metal) Te** | ~148 | ~101 | ~85.5 |
| **Average core enrichment %** | 1.9 | 2.8 | 0.71 |
| **Feed fissile content %** | 2.6 | 3.3 | 0.71 |
| **Fissile content in the core Te** | 2.81 (U-235) | 2.82 (U-235) | 0.61 (U-235) |

**Source Glasstone and Sesonske*

*Table 3: Comparison of eta in thermal and fast spectrum for fissile = nuclides.*

| Isotope | Thermal spectrum Maxwellian average | Fast spectrum Fission spectrum average |
|---|---|---|
| $^{233}U$ | 2.3 | 2.41 |
| $^{235}U$ | 2.077 | 2.32 |
| $^{239}Pu$ | 2.109 | 2.834 |

Table 3 with respect to the fissile requirement and average U-235 contents in the core. It is seen that a 600 MW (e) PHWR usually uses 85 Te of natural $UO_2$ fuel. The spent fuel from a PHWR will have 0.25% (2.5 g/kg) U-235 and about 0.3% (3 g/kg) of plutonium. On the other hand, discharged fuel from PWR has about 0.8% U-235 and 0.6% plutonium [5,6]. It would be prudent to reuse these fissile contents remaining in the discharge fuel by reprocessing and enhance the fuel utilization by recycling into these reactors.

With respect to the discharged fuel, it is important to estimate the radiotoxicity so that the fuel can be safely disposed. In Fig.4 the radiotoxicity of discharged fuel of a

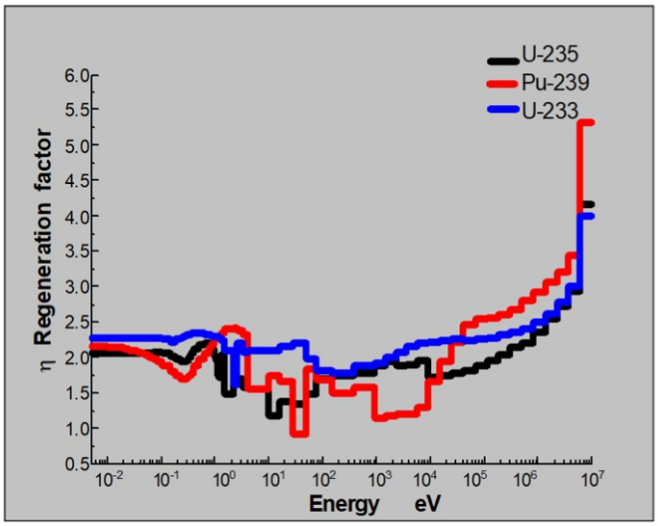


*Fig.3: Variation of with energy for fissile isotopes.*

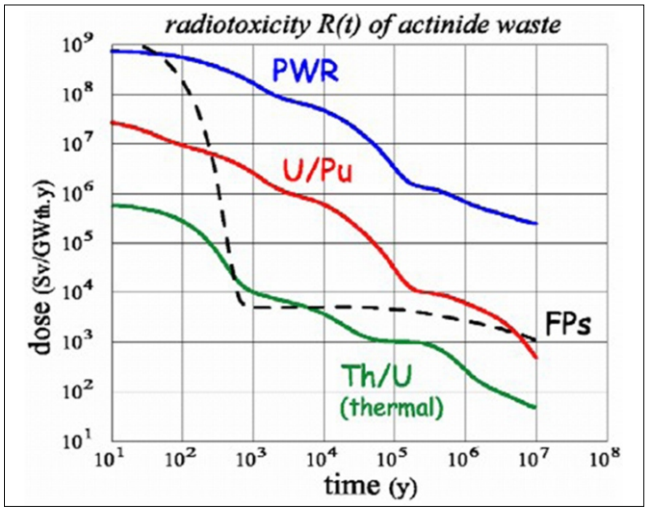


*Fig.4: Radiotoxicity of actinide wastes in Uranium and Thorium fuel cycle.*

[b] *Reaction cross section is measured in barns which is $10^{-24}$ $cm^2$. Physically this can be understood as the effective area offered by a nucleus for any type of reaction.*

[c] *Regeneration factor is defined as the number of neutrons produced per neutron absorbed.*

typical PWR is compared with that of (U,Pu) and (Th,U) cycle. When thorium is used as the initial fuel, the radio toxicity of the spent fuel is much less than in the discharged fuel of uranium cycle, which is clearly seen in Fig.4. Thorium being lower in the periodic table, the concentration of higher actinides produced in the thorium-based fuel during its residence time in a reactor and subsequent cooling is lesser than that of the uranium fuel of the same burnup.

### *How thermal is a thermal reactor?*

It is interesting to investigate the average neutron energies in thermal reactors. The moderator-to-fuel ratio plays an important role in defining the effective collisions with neutrons and thus has a bearing on fuel utilization and safety parameters. Most of the safety parameters such as temperature coefficient of reactivity, coolant void reactivity depends on the spectrum. In order to exploit the neutronic properties to designer's advantage, it is important to tune the neutron spectrum. For example, in AHWR, a harder neutron spectrum is achieved by reducing the lattice pitch and the void coefficient is made negative by neutron captures in Th-232 and Pu-239. The average neutron energy in AHWR is about 0.45 eV as compared to that in PHWR which is about 0.08 eV [7]. Physics design aims at optimizing the fuel performance w.r.t net reaction rates, i.e. maximize the fissile production and fertile captures for breeding. In thermal reactors the objective is to maximize thermal fission reaction rates. Table 4 presents the epithermal-to-thermal neutron flux ratio and it is highest in a PWR which is obvious because in a light water environment, the separation between the pins is adjusted so as to minimize neutron absorption.

*Table 4: Spectral indices in thermal spectrum reactors.*

| | PHWR | AHWR | PWR | BWR |
|---|---|---|---|---|
| Average neutron energy eV | 0.08 | 0.45 | 5.5 | 2.44 |
| Epithermal-to-Thermal ratio | 0.52 | 1.82 | 7.5 | 5.2 |
| Fissions below 0.625 eV (%) | 96 | 80 | 73 | 83 |
| Average thermal flux n/cm$^2$/s | 2.1 x 10$^{14}$ | 7.3 x 10$^{13}$ | 6.1 x10$^{13}$ | 2.5 x 10$^{13}$ |

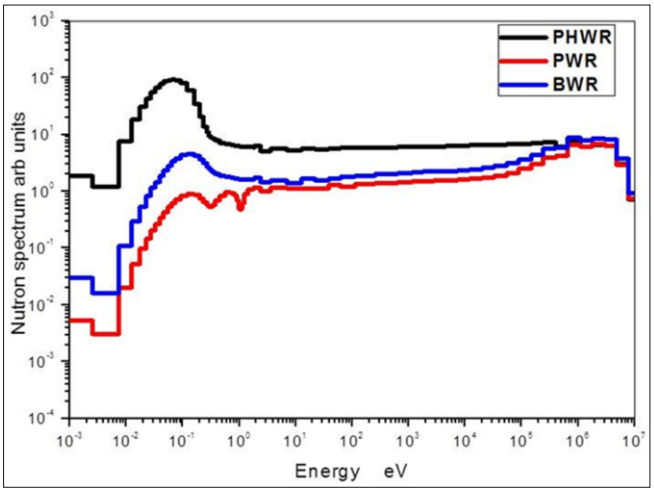


*Fig.5: Comparison of neutron spectrum in PHWR, PWR and BWR.*

The neutron spectrum has been compared for PHWR, BWR and PWR in Fig.5. The normalization is that the total flux is unity. The effect of 0.3 eV fission resonance of Pu-239 is more prominent in the PWR due to the fact the plutonium build-up rate is faster in PWR than other thermal reactors.

### Neutron Transport and Neutron Life Cycle

The aim of reactor physics simulation is to determine two most fundamental quantities that are the neutron flux and the k-effective[d] which is measure of neutron multiplication in the core. The neutron transport in any medium is defined by the inter collision distance or relaxation length. It may be noted that collision with fuel atoms could result in fissions and thereby production of more neutrons. In reactor physics terms this is seen as a measure of distance travelled by uncollided neutron and translates to migration length[e] when neutrons of all energies are considered. This factor coupled with the physical dimensions of the reactor determine the neutronic stability of the core. The neutron cycle in a thermal reactor may be perceived as a neutron born as a fission neutron undergoing successive collisions, and finally absorbed by a fissile atom. The different processes that happen with neutrons can be estimated in a probabilistic simulation by accounting of different probable reactions and estimating the neutron

*Table 5: Neutron induced cross section of some actinides at thermal energies.*

| | | $^{232}$Th | $^{233}$U | $^{234}$U | $^{235}$U | $^{236}$U | $^{238}$U | $^{239}$Pu |
|---|---|---|---|---|---|---|---|---|
| Cross sections at (0.0253 eV) 2200 m/s | $\sigma_c$ barns | 7.336 | 45.24 | 100.89 | 98.69 | 5.1319 | 2.6826 | 270.33 |
| | $\sigma_f$ barns | 0.00 | 531.21 | 0.067 | 585.09 | .0471 | 1.68E-05 | 747.40 |
| | $\alpha$ | - | 0.085 | - | .169 | - | - | 0.36 |
| | $\nu$ | - | 2.49 | 2.36 | 2.437 | 2.37 | 2.493 | 2.88 |
| | $\eta$ | - | 2.30 | - | 2.077 | - | - | 2.114 |
| Maxwellian averaged (1.0E-05-0.1 eV) | $\sigma_c$ barns | 6.88 | 43.21 | 94.39 | 92.266 | 4.84 | 2.529 | 273.56 |
| | $\sigma_f$ barns | 0.00 | 497.84 | 0.063 | 539.63 | 0.044 | 1.58E-05 | 721.32 |
| Maxwellian averaged (1.0E-05-10 eV) | $\sigma_c$ barns | 3.45 | 35.18 | 115.88 | 50.60 | 39.14 | 18.019 | 262.70 |
| | $\sigma_f$ barns | | 308.67 | 0.0730 | 269.14 | 0.0457 | 1.57E-05 | 532.63 |

[d] *K-effective is the multiplication factor in a medium where neutron fission chain reaction occurs and is a measure of the processes of production and destruction of neutrons.*

[e] *Migration length is the distance over which a neutron travels without getting absorbed.*

density. The various governing processes are fission, capture and scattering reactions. Each of these processes would create a change in the neutron population with respect to space, energy and time. Deterministically, the neutron balance equation is set up and the different production and loss mechanisms of neutrons are quantified. The life time of the neutron is characterized by the slowing down of neutron in a medium. The prompt neutron lifetime[f] for an infinite medium is defined as the inverse product of velocity and the macroscopic absorption cross section which is a material property of the medium. In an LWR, the average prompt neutron life time is about 0.2 ms and in a heavy water reactor this is one order higher about 2.5 ms.

### *Nuclear cross section sets for nuclear reactor design*

Neutron-induced cross section for all the types of reactions occurring in a reactor is a major input required for reactor design. Although the measured cross sections are available at discrete energies and fitted into continuous energy data using both theory and experiments, the data required for deterministic simulation will be reactor specific energy weighted neutron reaction cross sections. The weighting is carefully performed so as to conserve the reaction rate over the energy bins considered [8]. A summary of the various neutron interaction cross section both at specific energies and spectrum averaged values for major actinides are presented in Table 5 just to understand the interplay of cross section and the ambient neutron spectrum.

It is also to be noted that with a different thermal spectrum as seen in different thermal reactors, these cross sections would be different. The energy dependent cross section for some fissile isotopes is in relation with a typical neutron spectrum of AHWR as an example is given in Fig.6.

Availability of validated nuclear data for different nuclides and at all energies of interest is a challenging task. Mega facilities like CERN neutron time-of-flight (n_TOF) are required to experimentally determine the reaction cross section. The experimental data is required to be qualified and undergoes rigorous evaluation through best estimate approach before it becomes usable by reactor designers [8].

However, Monte Carlo codes use continuous energy cross section set which reduces one level of uncertainty of spectrum averaging.

### *Material challenges for advanced reactors*

Newer reactors such as Gen-IV reactors, AHWR, Metal fuelled fast reactors or MSRs use advanced fuel such as (U,Pu)MOX, (Th,Pu)MOX, U-Pu-Zr alloys or molten fluoride salts for features such as higher fuel utilization, irradiation stability and high temperature performance. These compounds are challenging to model as their physical and chemical properties themselves are not well known and material testing reactors using cutting edge technology are not available today. BeO is used a as a reflector in many thermal reactors, the scattering properties and irradiation behavior of BeO as a compound is not well understood even today. Both deterministic simulations and experiments are required to generate data for such materials. When designers target high burnups, the fuel clad material is also required to withstand the fission gas pressures and larger residence time. New alloys are being studied and

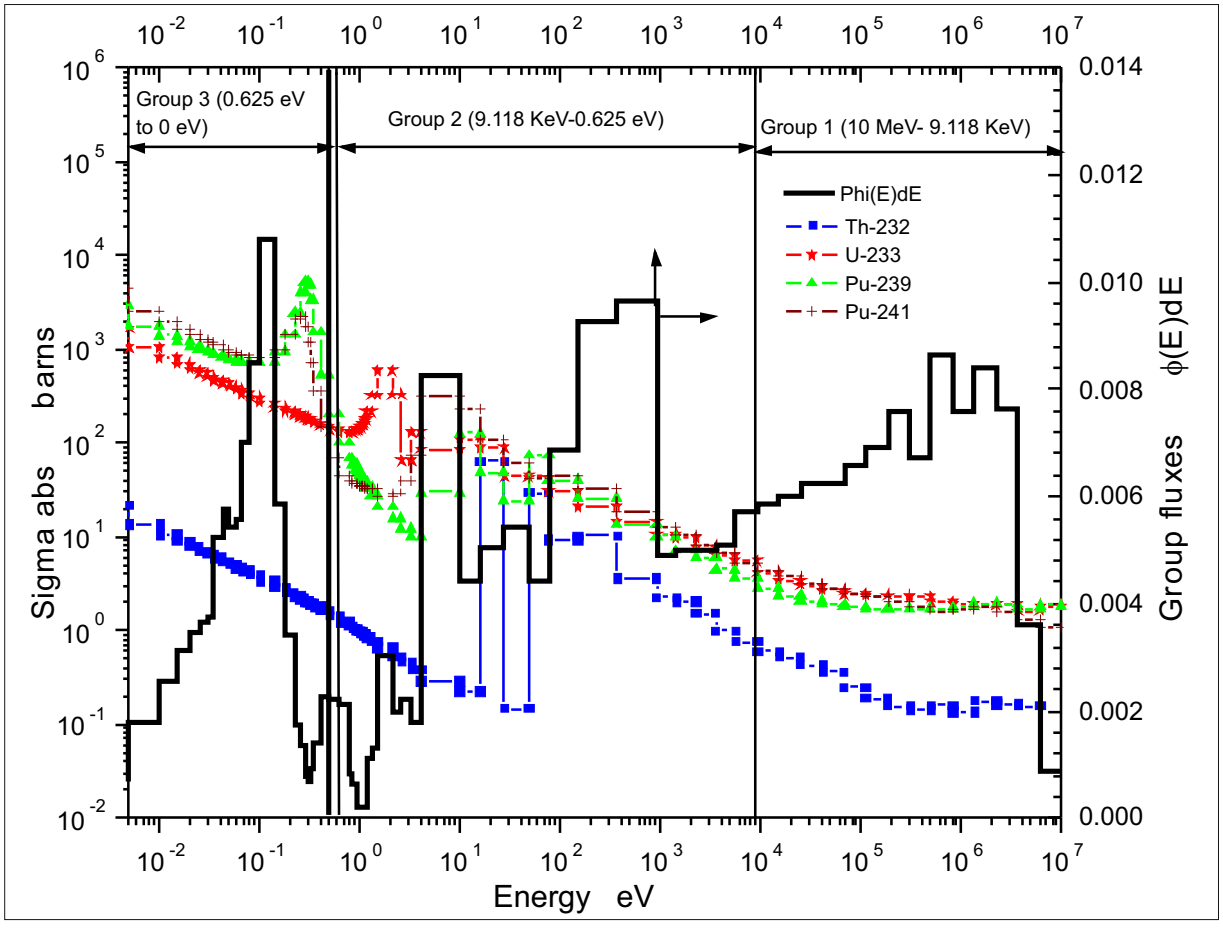


*Fig.6: Energy dependent absorption cross section of $^{232}$Th, $^{233}$U, $^{239}$Pu and $^{241}$Pu in relation to the neutron spectrum in AHWR.*

[f] *Prompt neutron life time is a measure of life of a neutron in a medium which is characterised by scattering, multiplication and captures. For finite medium, the quantity is derived from moderation or slowing down and can be measured.*

experiments are performed in accelerated environment to study radiation damage. M5, an alloy of Zr has been used a clad material in PWRs. An innovative idea of using pyrocarbon as moderating material in AHWR was suggested to reduce the effective moderation and to tune the neutron spectrum to achieve better safety performance [9]. In MSR, the candidate material for the vessel is Hastelloy and some high temperature reactors use Niobium. The choice of these structural material is dictated by the competing effect of neutron absorption and mechanical strength for the design pressure and temperature conditions.

With respect to enhanced safety, accident tolerant fuels are being designed where both better fuel matrix to withstand internal gas pressures and better clad to retain fission products are used.

## Advanced Reactor Designs

BARC is engaged in design of advanced reactors catering to different objectives of power generation. All the basic concepts of neutron physics discussed above have been prudently used in design of advanced reactors such as Advanced Heavy Water Reactor (AHWR), Indian Pressurised Water Reactor (IPWR), High Temperature (HTR), Molten Salt Reactors (MSR) etc. In this article some of these designs and their physics challenges are discussed.

### *AHWR challenges*

The AHWR is a 920 MWth, vertical pressure tube type thorium-based reactor cooled by boiling light water and moderated by heavy water designed to maximize power production from thorium [10, 11]. This is a unique reactor designed for large scale commercial utilization of thorium and integrated technological demonstration [12]. The objective has been to design an advanced reactor system utilizing thorium with several passive safety features incorporated. The aims of the design are to achieve relatively higher fraction of power from Th-$^{233}$U, self-sustenance in $^{233}$U, a high discharge burnup with minimum makeup fuel and the inherent safety feature of negative void reactivity coefficient [13]. Plutonium is used as makeup fuel to achieve high discharge burn up and self-sustaining characteristics of Th-$^{233}$U fuel cycle [11].

Light water coolant in a pressure tube system makes the void reactivity positive. The cluster design is mainly dictated by the objective of achieving negative void reactivity. The cluster design has undergone several levels of iteration. Also, from the heat removal considerations the cluster has been designed to have two axial enrichments in the outermost pins to obtain minimum critical heat flux ratio(MCHFR) with adequate margins [12]. The optimized equilibrium core cluster designed from all these competing objectives is presented in Fig.7a. The core layout is shown in Fig.7b. The breeding of U-233 in the cluster is clearly shown in Fig.7c.

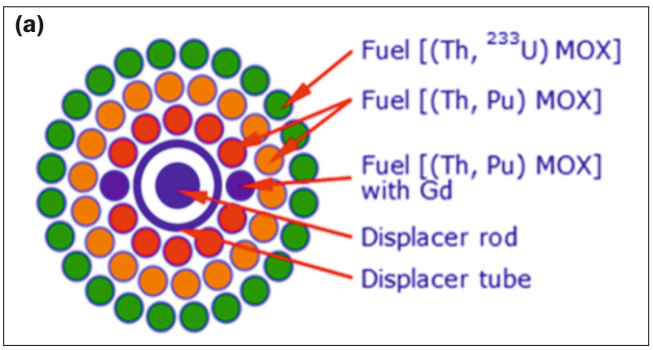


*Fig.7(a): Optimized AHWR equilibrium core fuel cluster.*

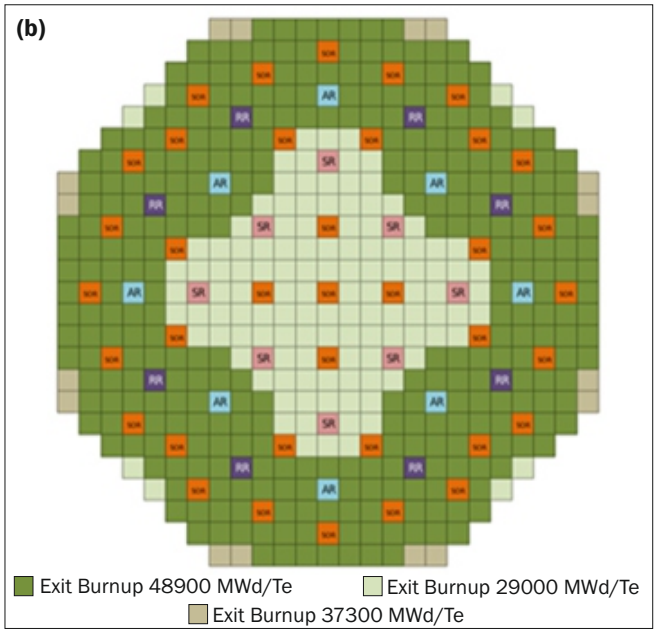


*Fig.7 (b): . Equilibrium core layout of AHWR .*

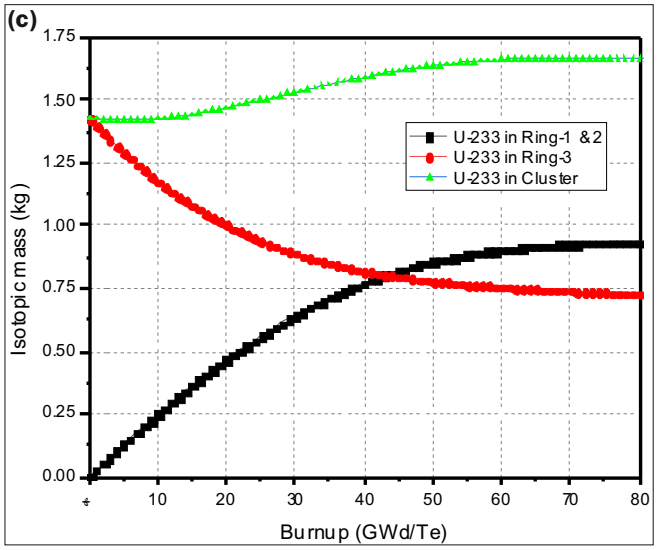


*Fig.7 (c): U-233 breeding in the equilibrium fuel cluster of AHWR.*

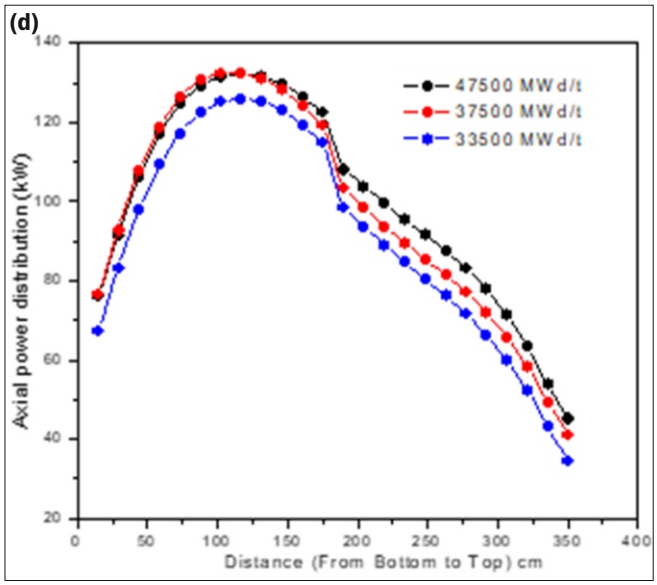


*Fig.7(d): Axial power distribution in the three burnup zones in AHWR equilibrium core.*

*Table 6: Design features of AHWR core.*

| | |
|---|---|
| Power to the coolant, MWth | 920 |
| Power from $^{233}U$, % | 75 |
| Total number of channels | 513 |
| No. of Fuel channels | 452 |
| Lattice type, pitch, mm | Square, 225 |
| Average discharge burnup, MWd/Te | 40000 |
| Active fuel length, mm | 3500 |
| ***Fuel material*** | |
| (For Pu topped variant) | (Th,U233)MOX and (Th,Pu)MOX |
| (For U235 topped variant) | (Th,LEU)MOX |
| Fuelling scheme | On power fuelling or Mini-batch |
| Fuelling rate | 73 channels/ year |
| ***Pressure tube*** | |
| Material | Zr-2.5%Nb |
| Inner Diameter/ Wall Thickness (mm) | 120/ 4 |
| ***Calandria tube*** | |
| Material | Zircaloy-4 |
| Outer Diameter/ Wall Thickness (mm) | 168/ 2 |
| ***Heat removal aspects*** | |
| Average heat rating, kW/m | 10.8 |
| MCHFR at 20% over power | 1.7 |
| ***Control and safety devices*** | |
| Control rods (CRs), Nos. | 24 (8 ARs, 8 RRs, 8 SRs) |
| Shut Down System-1 | Mechanical Shut-off rods ($B_4C$) 37 Nos. |
| Shut Down System-2 | Liquid poison injection (Gadolinium Nitrate solution) |

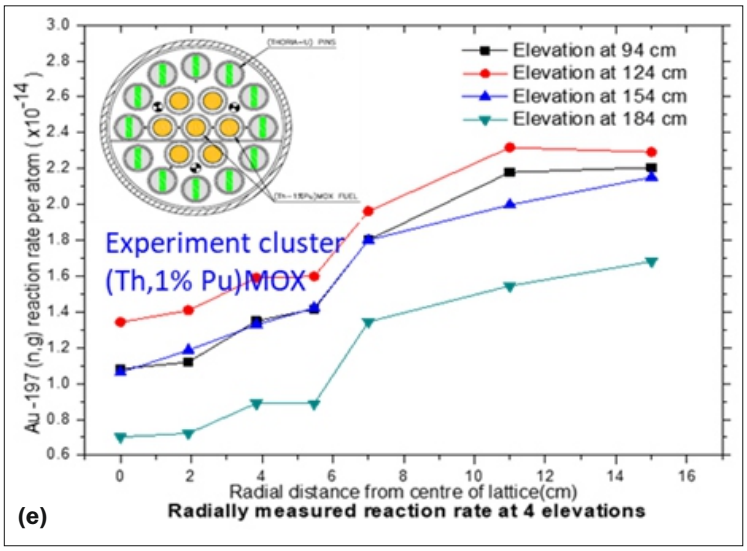



*Fig.7(e): Radial power distribution across experimental cluster at different elevations.*

*Fig.7(f): Arrangement of HDP blocks for measurement of coolant void worth for different void fractions in experimental (Th,Pu)MOX cluster.*

A uniform radial core power distribution that is preferred from natural convection standpoint is obtained by multi-zone fuelling. The number of fuel channels is large at 452 due to low core height of 3.5 m [14]. This increases the core or calandria radius as compared to a typical PHWR of similar thermal power. In order to achieve power distribution conducive for heat removal through natural circulation and achieve better thermal margins, a bottom peaked power distribution is desirable. This has been achieved by using differential enrichment in top and bottom of the fuel cluster and it is illustrated in Fig.7d. The basic design features of AHWR is presented in Table 6.

Several experiments have been performed in the AHWR critical facility to qualify thorium-based fuel and validate the neutronic codes and nuclear data used for design [15]. Integral parameters such as critical heights, level coefficient of reactivity, reactivity worths etc. were measured in Thoria, (Th, Pu) MOX and (Th, LEU) MOX fuel clusters and compared with theoretical estimates. Experiments for measurement of safety parameters such as coolant void worth, flux profile across the cluster were designed and performed. Axial and radial neutron fluxes were measured in the experimental thoria based cluster and coolant void worth in the (Th, Pu) MOX experimental cluster

also was measured recently [16]. The experimental measurements were in good comparison with calculated parameters and these were used to validate the design codes used for AHWR. Some results are shown in Fig.7e. The experimental arrangement for measurement of fractional coolant voids is shown in Fig.7f. The AHWR physics design has been indigenously evolved and the inherent safety has been demonstrated through several experimental programs.

### *Physics design of IPWR and its challenges*

The Indian Pressurised water Reactor (IPWR) is being designed with enriched uranium fuel and light water as coolant in a hexagonal lattice arrangement. The core design has been achieved by optimising the U-235 content with an objective to achieve a target discharge burnup of about 45 GWD/T in a multi-cycle batch fuelling mode [17]. The rated power was aimed at 900 MW(e) or 2700 MWth. The burnup reactivity control during the cycle is achieved by soluble boron. IPWR has been designed as per current safety standards where all the reactivity coefficients are negative. Another important objective of IPWR was to have neutron monitorability at all phases of operation in the core, namely cold, hot conditions, xenon free, transient conditions and over the complete operating cycle from beginning to end of cycle of fuel residence time.

The challenge was to achieve longer cycle length and use of neutron absorber Gadolinium as integral fuel burnable absorber. Fuel assembly has been profiled with different U-235 content and Gadolinium to achieve better local peaking factor and fuel burnup. The IPWR fuel assembly is presented in Fig.8a. The short-term and long-term reactivity control requirement in IPWR is achieved by control rods having neutron poison and chemical shim in the form of soluble boron respectively. With respect to the core design, soluble boron content at beginning-of-cycle has been minimized to achieve negative feedback coefficients through the heating phase and over the cycle. The fuel management patterns are being developed using both traditional schemes and heuristic approach. The optimized loading pattern of the equilibrium cycle of IPWR is shown in Fig.8b. The experience in designing IPWR has been effectively used to design an LWR core for lower power to be used in Small Modular Reactor (SMR). Table 7 shows certain salient features of the equilibrium cycle of IPWR. The IPWR design conforms to the current PWR standards of long cycle length and improved safety.

*Table 7: Design features of IPWR core.*

| | |
|---|---|
| Rated Power MW(e)/MW(th) | 900/2700 |
| No. of fuel assemblies (FA) | 151 |
| FA lattice arrangement | Hex |
| Fuel type/Enrichment | Enriched Uranium ~4.24% |
| Discharge burnup MWd/Te | 46000 |
| Average Linear Heat Generation Rate w/cm | 159.6 |
| Power density Mw/m$^3$ | 87.4 |
| Core periphery diameter mm | 3306 |
| Core baffle diameter mm | 3455 |
| Material of the core baffle | SS + water |
| Core barrel ID/OD mm | 3455/3600 |
| Material of the core barrel | SS |
| Thermal shield ID/OD mm | 3630/3780 |
| Reactor Pressure vessel ID/OD mm | 4170/4670 |
| System pressure MPa | 15.7 |
| Active core height mm | 3600 |
| Coolant inlet/Outlet temperature °C | 291/325 |
| Fuel management | Three batch fuelling |
| Reactivity control | Soluble boron ($H_3BO_3$ in water) |
| Shutdown and Control | Rod clusters in fuel assembly |
| Control rod material | $B_4C$ and $Dy_2TiO_3$ |

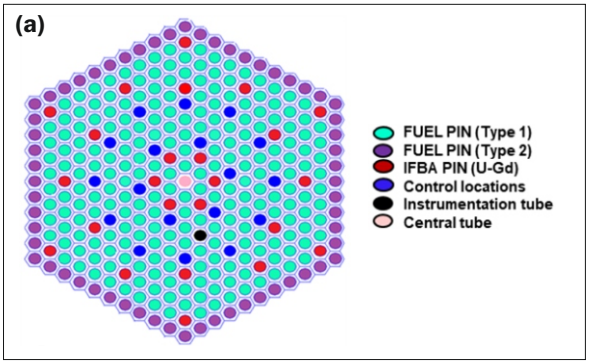


*Fig.8(a): Profiled fuel assembly of IPWR.*

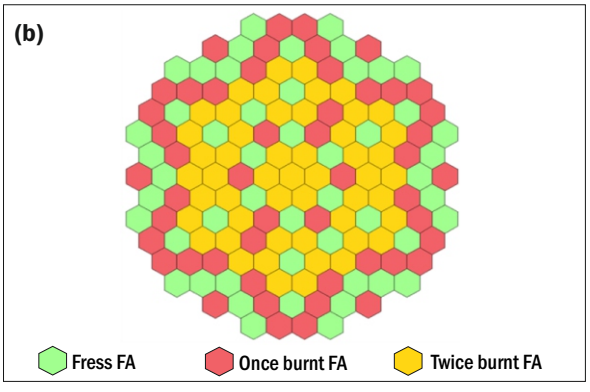


*Fig.8(b): Equilibrium core loading of 900 MWe of IPWR.*

### *Molten Salt Breeder Reactor (MSBR)*

In keeping with the mandate of designing an efficient thorium breeder system for the third stage of the Indian Nuclear Program, MSR is considered as a promising candidate. The fluid in an MSR is under circulation. By temporarily storing the irradiated thorium based molten salt in dedicated tanks, Pa-233 which has a 27-day decay half-life can be easily converted to fissile U-233 and pumped back into the reactor. By adjusting the feed and bleed of the molten salt, effective breeding can be achieved. The challenge is the physics simulation of liquid systems and managing the reactivity of the core. Studies of refueling rates and its effect on core reactivity have been done. Refueling study for a typical molten fluoride salt is shown in Fig.9a. The movement of liquid fuel results in a distributed delayed neutron source and hence the flow induced reactivity must be estimated more accurately (Fig.9b). Several core configurations have been designed with fluoride salts and fuel performance has been optimized. The current focus is on design of a thermal spectrum based 5 MWth demonstration reactor. Both Th-U233 and LEU based cores have been

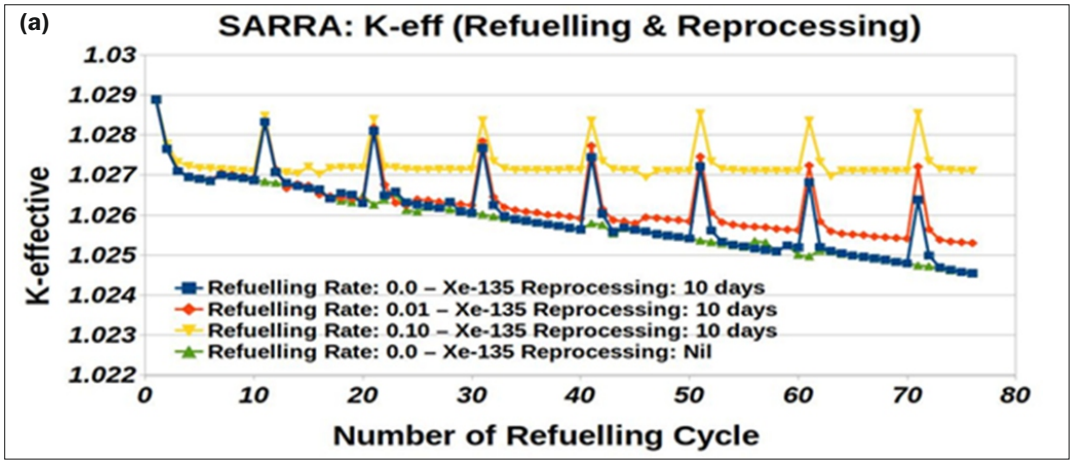


*Fig.9(a): Optimising of refueling cycle in MSR.*

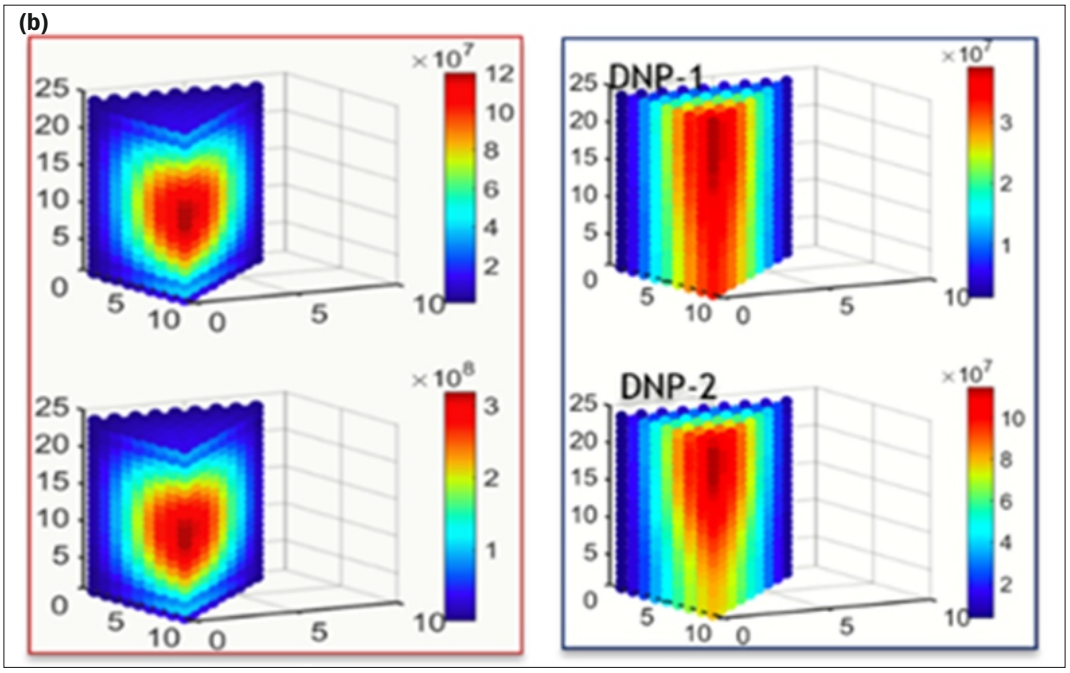


*Fig.9(b): Simulation for dynamics of molten salt - Movement of delayed neutron precursor.*

designed [18,19]. A typical core design of Th-U233 based 5 MWth MSR is shown in Table 8.

Neutronic tools have been developed for fuel management and treatment of dynamics of the molten salt [20,21]. The analysis studies include state-of-the-art studies on the advanced MSR fuel dynamics, benchmarking and validation, coupled neutronics-thermodynamics analysis; fission product, tritium transport; and effective thorium utilization and breeding. A molten salt fuel experiment is being designed and will be performed in critical facility to assess the integral parameters. The experimental results of the declassified MSRE experiments were analyzed with ARCH code and the results were found matching very well [22]. Other irradiation experiments for simulation of flow is being planned in research reactors.

### *Physics challenges of High Temperature Reactor (HTR)*

BARC is engaged in development of High-Temperature Reactors. The objective is to use the process heat for production of green hydrogen as an energy carrier of the future. A 100 kW Compact High Temperature Reactor (CHTR) was designed using the thorium. The physics design of CHTR has

*Table 8: Physics design features of 5MWth MSR of AHWR.*

| | |
|---|---|
| Power | 5 MWth |
| Fuel Salt inventory | 1.57 Tonne |
| U-235 inventory | 172 Kg |
| Graphite inventory (moderator) | ~6 Tonne |
| Number of Fuel Channels | 1176 |
| Fuel salt/Composition | LiF-CaF2-ThF4-UF4 : 70%-8%-0%-22% |
| Enrichment (U-235, Li-7) | 19.75 %, 99.9% |
| Control and Shutdown material | B4C |
| Fuel Temperature Coefficient (Doppler) | -4.0 pcm/°C |
| Loss of Delayed Neutron Precursor(DNP)due to salt flow | 272 pcm |

*Table 9: Physics design features of 5MWth MSR of AHWR.*

| | |
|---|---|
| Reactor Power | 100 kW (thermal) |
| Fuel | TRISO particles of ($^{233}$U-Th)$C_2$ or (Th,LEU)$C_2$ |
| Core fuel cycle | 15 effective FPYs |
| Coolant | Lead-Bismuth Eutectic |
| Core inlet/outlet | 900/1000$^0$C |
| Moderator/Reflector | BeO/BeO and Graphite |
| Height & diameter | 100 cm & 127 cm |

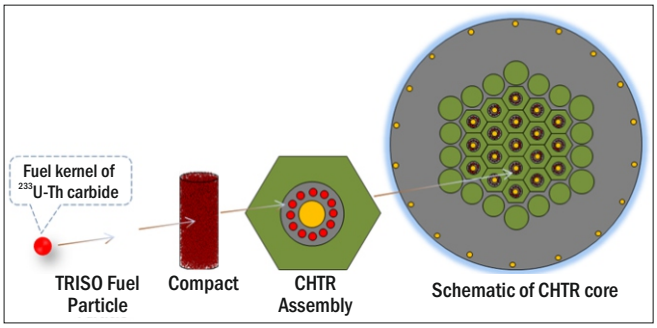


*Fig.10: Schematic of fuel particles and the CHTR core.*

advanced features like thorium-based TRISO coated fuel, long core life cycle, negative temperature reactivity coefficients, core heat removal by natural circulation, and decay heat transfer to the surroundings passively during severe accidents [23]. The physics challenge here is to design long life core spanning 10 to 15 years with sufficient burnable absorber to sustain reactivity throughout the core life. The compact nature poses issues of locating the reactivity mechanisms and optimizing the fuel performance. The optimized core characteristics of CHTR core is presented in Table 9. The simulation of heterogeneous CHTR core with graphite bores containing TRISO particles is illustrated in Fig.10.

The natural circulation cooled and TRISO particles fueled CHTR design necessitates multi-physics investigations of the high-temperature core under normal operations and anticipated transients. An indigenous capability, code ARCH-TH, for simulations of full core neutronics coupled with thermal-hydraulics has been developed and extensively validated for viability. Subsequently, the anticipated transients in CHTR were investigated in detail. The analyses of CHTR transients demonstrate the designed passive features of the core.

It is also worth mentioning that these types of core design can be successfully used for district heating or as power packs for remote areas. In another version of HTR, a pebble bed core was simulated which has potential for hydrogen generation [20]. In a pebble, several thousand of TRISO fuel particles are embedded in a graphite matrix. The core design envisaged movement of these pebbles from bottom to top, thereby facilitating online refueling. The physics challenge was the treatment of double heterogeneity. A code PebMC was developed to solve for the flux/power distribution in the core [24].

## New Energy Systems

In order to exploit the physics properties of different materials, many new concepts have been developed both in India and elsewhere in the world. For example, if super critical water is used, the moderating properties can be tuned to achieve breeding in thermal reactor systems. Use of lead and lead bismuth eutectic as coolants has been explored in order to go to high temperatures and improve the heat removal [25]. Inert matrix fuel has superior metallurgical properties and can be used to retain the fission gases inside the fuel matrix. Few systems that are being designed are briefly explained here.

### *Advanced LWRs*

In order to increase the fuel utilization, LWRs are being designed with longer cycle lengths. This would require higher fissile content or enrichment. Longer burnups are limited by degraded fuel behavior, fission product release and degradation of clad. Different reactors are being proposed with elegant solutions for each of these issues. Studies on the use of low neutron absorbing clads have been done to aid the use of higher enrichment in fuel. Plutonium recycle is another option to improve the burnup in thermal reactor systems. High burnup fuel would also require the use of neutron poison like Gadolinium or Erbium to be mixed with fuel. Several fuel cycle options in thermal reactor systems with thorium as a carrier either with weapons grade or reactor grade Plutonium have been extensively studied [6].

### *Small modular reactors (SMRs)*

It is seen from the operating experience of LWRs, that small reactors are easy to operate and have enhanced safety features. SMRs are smaller than traditional nuclear reactors, and can be used to provide a reliable source of energy in a variety of settings. They are designed to be factory-built and transported to the site for installation, allowing for faster and more efficient construction. The current designs envisage that all reactor components are placed inside the pressure boundary and can be treated as an integrated module. The power rating of these modules typically ranges from 20 to 200 MW(e). Such units can be combined in a reactor site to increase the power output. SMRs are ideal to replace the aging coal fired plants. However, the key to success of SMRs in this application will be to design systems with more passive safety features leading to a much lower risk of accidents or malfunctions.

Design of these compact integrated modules is challenging. The power density is designed to be higher and will require enriched fuel in a better matrix so that fission products and fission gasses can be contained. The reactor core being considered is a hexagonal core with enriched uranium fuel in a once through mode. The U-235 content is adjusted to achieve large cycle lengths.

### *HTRs - Gas cooled and Liquid Metal cooled*

Gas-cooled reactors (GCRs) have been used since the earliest days of nuclear power using graphite as moderator and helium or $CO_2$ as the coolant. In early history, GCRs used natural uranium as fuel in thermal spectrum and competed with LWRs without relying on the enriched uranium fuel. Both UK and France developed Magnox-type gas cooled reactors, with France building nine reactors and the UK building 24 reactors. This was followed by development of Advanced Gas Cooled Reactors (AGRs) which were built in UK and are classified as generation-II gas cooled reactors. Unlike the first-generation Magnox reactors, which were optimized for plutonium, AGRs were made to economically produce power similar to the coal fired plant and thus required higher operating temperatures. The AGR designs, therefore, are developed with stainless steel cladding and enriched uranium fuel leading to higher burn-ups of about 18GWD/T. The AGR's oxide fuel, with higher operating temperature compared to the metallic Magnox fuel, also resulted in improved power conversion efficiency of about 42%, compared to around 28% in a Magnox.

BARC is looking at the feasibility of developing gas cooled reactors for hydrogen generation. GCRs have several advantages over LWRs, such as use of natural uranium fuel and use of gas coolant but are bulky and have lower power densities. The High Temperature Reactors (HTRs) are also categorized as GCRs which are designed with specialized TRISO coated fuel and with inert helium gas coolant. A preliminary physics study has been recently initiated.

### *Accelerator driven sub-critical system (ADSS)*

In an ADSS, particles or ions are accelerated to high energies and made to bombard on heavy elements which then produce a large number of neutrons. High energy protons, on colliding with a target of high-density element (such as lead, tungsten, and uranium cause the detachment of a large number of neutrons from these nuclides in a process known as "spallation." The ADSS consist of three components namely, the accelerator, the target and the blanket in addition to heat removal and electrical generating equipment. The blanket can be fertile or fissile, or irradiated fuel having fission products. Copious number of neutrons could be produced if the energetic beams are incident on the high-Z target material.

Typically, an accelerator producing intense high energy proton beams of 1GeV energy and current of 10mA is used. These protons are made to be incident upon a heavy metal target such as Lead to produce neutrons by the spallation reaction. The number of neutrons per proton depends upon the target material, its size and the proton energy. For example, for when a 1GeV proton is incident on Pb target, about 20–30 neutrons may be produced. A typical schematic of ADSS is shown in Fig.11.

Energy amplification can be demonstrated from first principles in an ADSS. A 1 GeV proton beam mentioned above requires about 40 MeV to produce one neutron and the electrical energy required will be about 100 MeV. The subcritical multiplication resulting from this spallation can provide additional neutron population in the subcritical

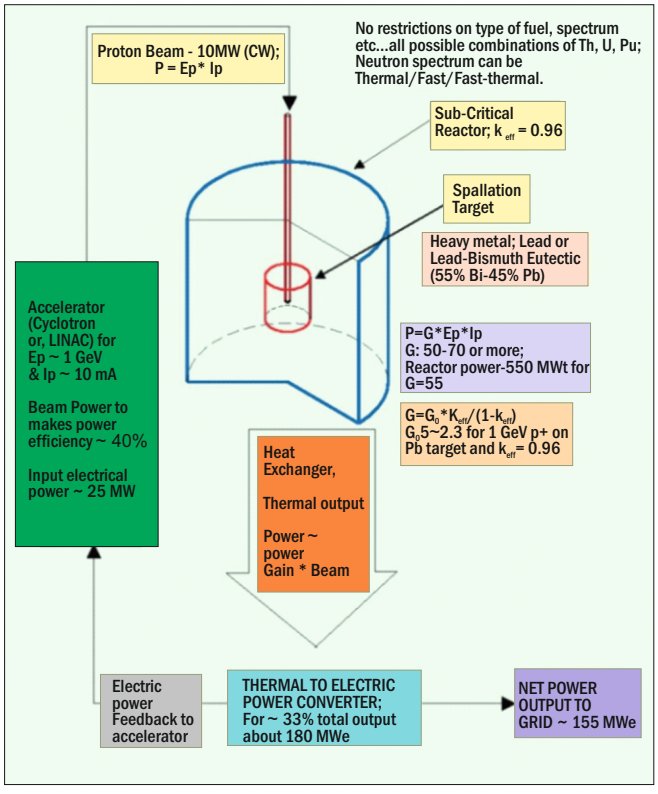


*Fig.11: Components of Accelerator Driven Sub-critical core (ADSS).*

blanket. Considering a multiplication factor of 0.98 the net fission neutrons generated by one spallation neutron will be about 20 and the fission energy converted to electrical energy released will be about 1.3 GeV [26]. Therefore, this system is also called an "energy amplifier."

### Hybrid Reactors

Fission-Fusion hybrid reactor systems have a good potential to breed fissile content. The inner fusion core is a good source of neutrons and if it is surrounded by a fertile or fissile blanket region, breeding or transmutation can be achieved. The fusion core is usually based on the efficient D-T reactions. The core design is governed by the balance between use of the neutrons from fusion core to breed fissile species and to breed tritium. The temperature in the inner fusion core will be about a few keV and the neutrons emitted usually have energies of 3-5MeV. These high energy neutrons can be made to cause either fissions or captures in the surrounding blanket. Transuranic elements have significant fission cross sections for high energy neutrons and if the blanket is fueled with these elements, they can be converted to other actinides and reduce the waste volume.

### Simulation Techniques and Methods

The fundamental quantity to be calculated are the neutron flux distribution and the effective multiplication factor. Advanced reactors have several design objectives to cater to and are phenomenologically more intensive to simulate. More heterogeneities are introduced for enhanced safety and to improve fuel utilization. Thus, these advanced energy systems are characterized by multi-physics phenomena and are required to be modeled exactly.

On the deterministic front, the discretization in space and energy are being taken to higher levels. The reactor core is being analyzed over larger number of both regular and irregular nodes or meshes and the flux can be determined more accurately using advanced numerical techniques. The parameters are required at pin section, pin level, fuel assembly level and global core level. The energy domain is being discretized to finer bins to span nine orders of neutron energies from MeV to meV range [27]. The time domain to be dealt with in reactor physics simulations must also cover a huge range. The reaction mechanisms are to be understood in the femtosecond scale. The reactivity feedbacks are modeled in micro second range. The transients are modeled in steps of milliseconds to estimate the power rise phenomenon over time intervals of a few seconds to minutes. Fuel management in reactors are performed over a few days or months. The isotopic concentrations of fuel out of the core are governed by natural decay and could vary from milliseconds to millions of years. Thus, it is obvious that a single code or single technique cannot cater to these varied simulations required and that too with good accuracy [27]. A brief on some codes and methods developed are detailed here.

ARCH is a diffusion theory-based 3D core analysis code using finite difference techniques developed for both square and hexagonal geometries [28]. New multi-physics modules ARCH-TH has been introduced in this code and it also has been coupled with thermal hydraulics in a code system PROMISIN.

ADWITA is a fuel cycle analysis code developed for spent fuel analysis which estimates actinide concentration, activity of actinides and fission products and radiotoxicities [29]. This has been validated with experimental results decay heat and PHWR discharged fuel of both uranium and thorium cycle. Codes based on probabilistic methods have also been developed. The general geometry continuous energy Monte

**ARCH:: Analysis of Reactor Transients in Cartesian and Hexagonal Geometries**

***Used for HTRs, AHWR, IPWR, VVER, IMSR :: Well validated***

* Rectangular & Hexagonal lattices, K-eff, External Source simulation
* Xenon spatial Oscillations & Transients : TH module included
* Fuel Burnup, Core Followup

**ADWITA: Activation, Decay, Waste Incineration and Transmutation Analysis**

*Use of multiple methods for (TTA)
*Inventory generation based on power history
*Decay Follow up of the generated inventory
*Mass, Activity, Decay heat rate during all time

**Reactor Physics Codes**

**OpenMC-McBurn Integrated code**

*Integrating McBURN code with OpenMC code for burnup simulation
*Heterogeneity modelling, continuous energy nuclear data
*Detailed spatial treatment
*Reaction rate transfer from McBURN
*Validation with PHWR and VVER fuel for benchmarking the coupling

**Other new generation codes**

M3C :: Monte Carlo Criticality code
TRANPIN ::2D whole core transport solver
CARS/CARS-ANN :: Auto fuel management
PATMOC :: Multi-group MC code
VISWAM :: Improved lattice simulation tool
HEXPIN :: Pin-by-pin analysis for hexagonal cores;
STEMR ::MOC based transport using ray tracing
DIAMOND :: MOC Code for square LWRs
KINFIN :: MC based transient analysis tool

**State-of-the-art reactor physics analysis tools developed for analysis and design of thermal reactors**

*Fig.12: Reactor Physics code basket developed by RPDD.*

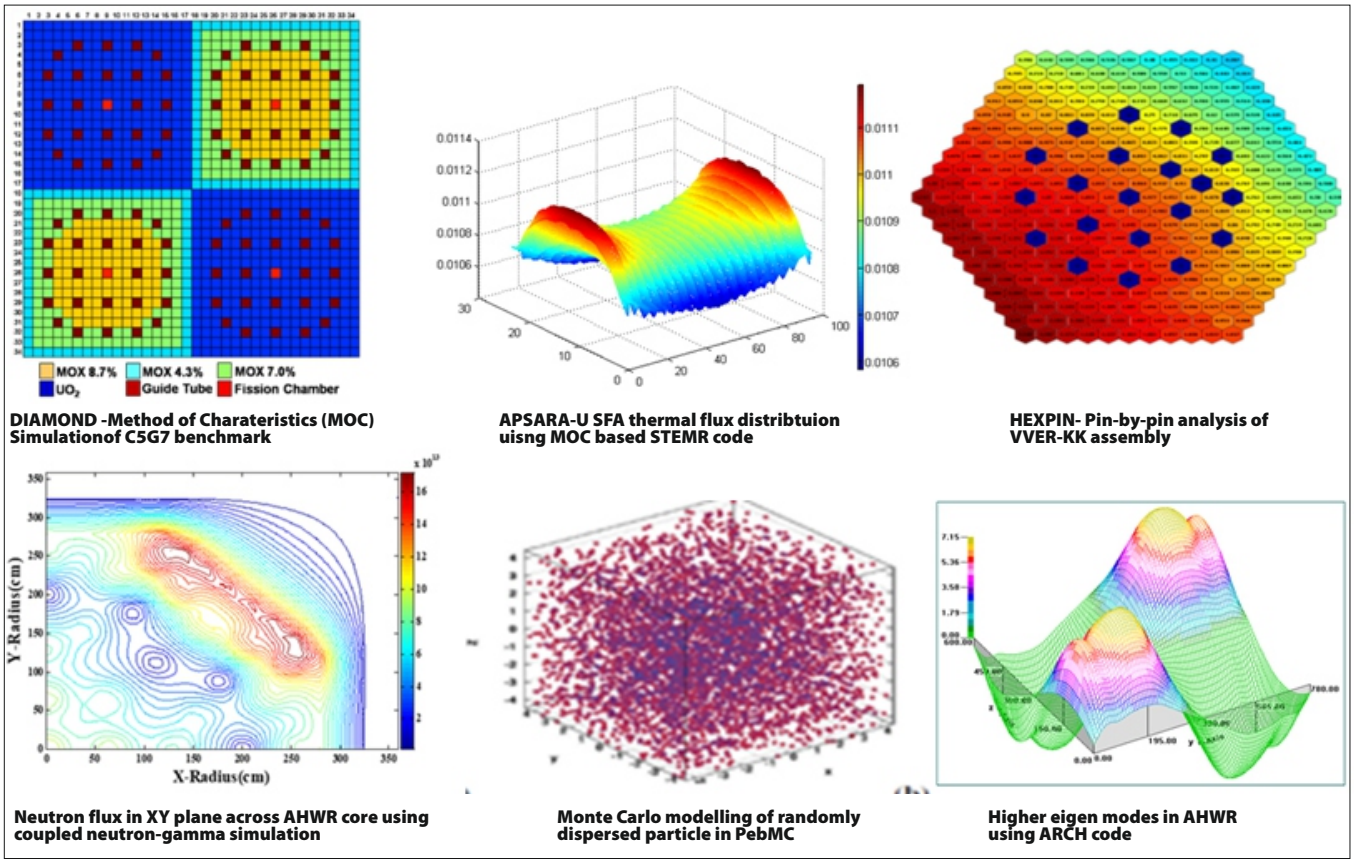


*Fig.13: A few simulation results from advanced neutronics codes.*

Carlo code M3C, multi-group Monte Carlo code PATMOC and time dependent Monte Carlo code KINMC have been developed and validated extensively and used for routine simulations [30,31,32]. McBURN - a Monte Carlo based burnup simulation tool has been integrated with the indigenous Monte Carlo codes and tested for burnup simulations of PHWRs and VVERs. An overview of the reactor physics codes developed recently is shown in Fig.12.

VISWAM, a versatile neutron transport code for lattice geometries has been developed with several options of solution methods. TRANPIN and HEXPIN, core simulation tools have been developed for triangular geometries for a detailed pin-by-pin analysis [33]. Transport theory codes are used for more exact simulation of highly heterogenous cores. 2D MOC codes for neutron transport DIAMOND and STEMR have also been developed. Some of the other codes that have been developed based on advanced methods and techniques are

in-core fuel management code CARS based on genetic algorithms and ANN [34], PebMC, a Monte Carlo method for treating fuel pebbles in high temperature reactors, SAARA, code for fuel management in MSRs, MSDyn, a circulating fuel salt analysis code and codes based on modal analysis. Multi-physics modeling in MSDyn and ARCH-TH have been verified with experiments and results have agreed very well [35,36]. Some of the selected results from the simulations using advanced codes and methods are presented in Fig.13. A varied set of codes cratering to several different applications have been developed and tested over the years.

## Summary

The physics challenges are manifold for future energy systems. Reactor physics design and the engineering development are complimentary and they influence each other. Multi-physics modelling is very important to determine the safety and estimate the feedbacks more accurately. Experimentation on fuel and processes will help in reducing margins and validate the neutronic tools. Post irradiation examination of irradiated fuel will throw light on the fuel behavior especially for high burnups. Material challenges are varied and new materials have to be developed and experimentally qualified for its high irradiation stability and durability. To quote a few specialized tasks, better neutron transport methods to estimate the tritium breeding in ITER blanket, use of more foil irradiation coupons to cover the entire energy range to estimate the fluence in reactor pressure vessel (RPV) in LWRs, and study of fuel thermo-mechanical behavior both with deterministic and AI techniques.

In order to estimate the neutron counts in highly sub-critical phases, better physics methods will be required and signature of the emerging particles should be captured more accurately and out-of-core detection systems also should be enhanced. Newer detectors for estimation of in-core fluxes are required for the different types of neutron spectra that will be encountered in future.

On the nuclear physical constants, for neutron and particle induced cross sections, more precise measurements are required with cutting edge technology. Elastic scattering cross section of new compound materials is the need of the day even for current generation reactors. High energy cross sections are difficult to measure and require more precise instrumentation. Neutron and gamma shielding will also play a major role in these new and hybrid energy systems and Monte Carlo based particle transport methods will be required and will be tested to their ultimate capabilities in order to develop cost effective shields. Irradiation behavior is not fully understood for new fuel types and will require long irradiation campaigns, detailed post irradiation examination and accelerated testing in accelerators.

New generation power reactors are being designed with diverse objectives and require newer materials and better simulation methods. On the research reactor front, the challenge will be to achieve high neutron fluxes for material characterization and design several features for extracting the neutron for basic research. This will also involve the development of many engineered systems such as neutron guides, detectors and spectrometers and high energy probes. These novel experimentation efforts will induce reactor technologists to take up more challenges. The excitement in reactor design is driven by deep understanding of the basic physics of nuclear interactions and its interplay with other processes.

## Acknowledgement

The author wishes to express her thanks to K. P. Singh, Anurag Gupta, Devesh Raj, Suhail Ahmad Khan, Amit Thakur, Rajeev Kumar, Kapil Deo, Arindam Chakraborty, Anindita Sarkar and all officers of RPDD.

Special thanks are due to T. Sakuntala for reading and suggesting improvement in the manuscript. Thanks are also due to AD, KMG for doing all the needful to publish this article.

## References

[1] https://www.world-nuclear.org

[2] Physics of nuclear reactors Mohanakrishnan P., Singh O. P., Umasankari Kannan (Eds). Physics of Nuclear Reactors. San Diego: Academic Press, 2021.

[3] Gen IV International Forum, https://www.gen-4.org/

[4] Umasankari Kannan and P. D. Krishnani, "Energy from Thorium - An Indian perspective", Sadhana Vol 38, Part 5, October 2013, 81–837.

[5] Umasankari Kannan and R. Srivenkatesan, "Fuel performance indices for Thorium-Uranium-Plutonium fuelled Advanced Heavy Water Reactor with closed fuel cycle", Paper presented at the International Conference on Nuclear Engineering ICONE-15, Nagoya, Japan during 22-26 April, 2007.

[6] "Extending the Global reach of nuclear energy through thorium", DAE, Govt. of India published at IAEA General Conference Side event (2008).

[7] Umasankari Kannan, "The story of fission reactors – From Chicago pile to advanced energy systems", Invited talk presented in NUCAR-2017, 6-8th Feb, Bhubhaneshwar.

[8] Umasankari Kannan, "Perspectives on nuclear data for advanced reactor design and analysis", Journal of Life Cycle Reliability and Safety Engineering, 9(2), 135-146 DOI 10.1007/s41872-020-001205

[9] Anil Kakodkar, "Advanced Heavy water Reactor", Proc. INS annual conference on Advanced Technologies related to nuclear power INSAC1994, Feb 28 to Mar 2, 1994, Mumbai.

[10] Anil Kakodkar, "Salient features of design of thorium fuelled Advanced Heavy Water Reactor", Indo-Russian seminar on thorium utilisation, 17-20 Nov 1998, Obninsk, Russia.

[11] Kamala Balakrishnan and Anil Kakodkar, "Preliminary physics design of Advanced Heavy Water Reactor (AHWR)", proceedings of the Technical Committee Meeting on the Technical aspects of high convertor reactors, Nuremberg, March 1990, IAEA-TECDOC-638.

[12] R. K. Sinha, and Anil Kakodkar, 2006. Nucl. Engg. and Design Vol 236, Issues 7-8, pp 683-700. Design and development of AHWR – The Indian Thorium fueled innovative reactor,

[13] Umasankari Kannan, Neelima Prasad Pushpam, Arvind Kumar, S. Ganesan, P. D. Krishnani, R. Srivenkatesan and R. K. Sinha, "Physics design aspects of Thorium Fueled Advanced Heavy Water Reactor (AHWR)", paper presented Advances in Nuclear Fuel Management IV (ANFM 2009) Hilton Head Island, South Carolina, USA, April 12-15, 2009, on CD-ROM, American Nuclear Society, LaGrange Park, IL (2009).

[14] R. Srivenkatesan, Arvind Kumar, Umasankari Kannan, V. K. Raina, M. K. Arora, S. Ganesan, and S. B. Degweker, "Physics considerations for utilisation of Thorium in power reactors and subcritical cores", Proc. of annual conference of Indian Nuclear Society, INSAC-2000 on "Power from Thorium – Status, Strategies and directions" June 1-2' 2000, Mumbai.

[15] Kapil Deo, Amod Kishore Mallick, Neelima Prasad, Rajeev Kumar, Sudipta Samanta, Deep Bhandari and Umasankari Kannan, Reactor Physics Experiments at AHWR-Critical Facility", BARC/2022/I/020, September, 2022.

[16] Amod Kishore Mallick, Rajeev Kumar, Sudipta Samanta Kapil Deo, Deep Bhandari Yogesh Upreti, Umasankari Kannan, V. Shivakumar, Sharad Kumar Verma, S.K. De, Avaneesh Sharma, "Experimental study of voiding effects with thorium based MOX fuel cluster in Critical Facility", Nuclear Engineering and Design 398 (2022) 111973.

[17] Devesh Raj, Anindita Sarkar, Gopal Mapdar and Umasankari Kannan, "Technical Design report of IPWR : Reactor Physics chapter", RPDD/IPWR/ 27/2015, 23rd Nov 2015.

[18] A. K. Srivastava, Anurag Gupta, Umasankari Kannan, "Studies of a thermal spectrum small experimental IMSR with different U-235 fuel salts to maximise fuel utilization". RPDD/MSR/31-A/FEB-2019

[19] A. K. Srivastava, Anurag Gupta, Umasankari Kannan, "Reactivity coefficients study in small power, experimental, thermal spectrum MSR", RPDD /MSR/43/ JUN-2020

[20] Indrajeet Singh, Anurag Gupta and Umasankari Kannan, "Design report of innovative pebble-bed high temperature reactor (IHTR20)- Current status", BARC/2023/I/009.

[21] Indrajeet Singh, Anurag Gupta, "A Dynamic Analysis of Circulating Fuel Reactors with Zero-Dimensional Modeling", SRESA's International Journal of Life Cycle Reliability and Safety Engineering Vol.4 (4), 54-59, 2015.

[22] T. Sai Chaitanya, Anurag Gupta and Umasankari Kannan, "Neutronic Analysis of MSRE and its study for validation of ARCH code", Nucl. Engg. and Design., 320, 1-8, 2017.

[23] Dulera, I. V. et al., High temperature reactor technology development in India, Progress in Nuclear Energy 101, 82-99, 2017.

[24] Indrajeet Singh, S. B Degweker, Amod Kishore Mallick and Anurag Gupta, "A New Approach to Monte Carlo in High Temperature Reactors", Nuclear Science and Engineering, Vol. 193:8,868-883(2019). https://doi.org/10.1080/00295639.2019.1576453

[25] D. K. Dwivedi, Anurag Gupta, Umasankari K., "Transient simulation of LBE cooled CHTR under natural circulation with 3D multi-physics code ARCH-TH", Proceedings of 'IUSSTF Symposium on Advanced Sensors and Modeling Techniques for Nuclear Reactor Safety', Dec 15-19, 2018, IIT-Bombay, Mumbai.

[26] S. B. Degweker, "Accelerator Driven Systems for thorium utilization in India", Thorium Energy Conference 2013 (ThEC13), CERN Globe of Science and Innovation Oct 27-31, 2013, CERN Zurich.

[27] Umasankari Kannan, "Physics of next generation reactors– Towards self-reliance in design, safety and operation", Proc. of Advances in Reactor Physics (ARP-2022), Mumbai, India, May 18-21, 2022.

[28] Anurag Gupta, ARCH: A 3D Space-Time Analysis Code in Cartesian and Hexagonal Geometries. 19th National Symposium on Radiation Physics (NSRP-19), Dec 12-14, 2012, Mamallapuram, TN, India.

[29] Devesh Raj and Umasankari Kannan, "Development of computer code ADWITA and data library for the solution of transmutation chain equations and application to the analysis of nuclear fuel cycles", Annals of Nuclear Energy,164, 108619, 2021.

[30] Anek Kumar, Umasankari Kannan and S. Ganesan, "Development of an Assembly-Level Monte Carlo Neutron Transport Code "M3C" for Reactor Physics Calculations", Nuclear Science and Engineering, July 2019, https://doi.org/10.1080/00295639.2019.1645502

[31] Amod Kishore Mallick and Umasankari Kannan, "PATMOC : A Multi-group Monte Carlo code for Neutron Transport Simulation", RPDD/EP/164 (2018).

[32] Argala Srivastava, K. P. Singh, Amod Kishore Mallick, Umasankari Kannan and S.B. Degweker, "A diffusion Monte Carlo based Algorithm for Estimation of Higher Eigen Values for Reactor Core", Nuclear Science and Engineering, Vol 193, 1044-1053, 2019.

[33] Suhail Ahmad Khan, Umasankari Kannan and V. Jagannathan, "Development of Whole Core Pin by Pin Transport Theory Model in Hexagonal Geometry", Annals of Nuclear Energy, 104, 214–228, 2017.

[34] Amit Thakur, Debasmit Sarkar, Vishal Bharti and Umasankari Kannan, "Development of in-core fuel management tool for AHWR using Artificial Neural Networks" Annals of Nuclear Energy, 150, 107869, 2021.

[35] Indrajeet Singh, Anurag Gupta and Umasankari Kannan, "Studies on Reactivity Coefficients of Thorium-Based Fuel (Th-233U)O2 with Molten Salt (Flibe) Cooled Pebble", Nuclear Science and Engineering, 191, 161–177, Aug 2018.

[36] D. K. Dwivedi, A. Gupta, P. D. Krishnani, "3D space time analysis of anticipated transient analyses in CHTR with Fuel Temperature feedback", In: Nayak A., Sehgal B. (eds) Thorium- Energy for the Future. Springer, Singapore, 2019, https://doi.org/10.1007/978-981-13-2658-5_31.

# Applications of Deep Learning

2

# Deep Learning based Technology for Fuel Bundle End Plate Weld Inspection

**Rahul Jain[1], Sanjeev Sharma*[1], G. Venugopal[2], S. Sairam[2] and K. Madhusoodanan[1]**

[1]*Division of Remote Handling & Robotics, Bhabha Atomic Research Centre, Mumbai – 400085, INDIA*
[2]*Nuclear Fuel Complex, Hyderabad – 501301, INDIA*

*Fuel elements welded with end plate*

ABSTRACT

Detecting defects at every stage of the fabrication of nuclear fuel bundles is essential for ensuring high-quality assurance standards. This paper presents the state-of-the-art deep learning method for detecting the quality of end plate welding with each fuel element. The system can identify good and potentially incorrect welds for active assistance to operators. The proposed method achieves mean precision of 0.9918 and a mean recall of 0.9916 with test images.

KEYWORDS: *Defect identification, Welding defect, Deep learning, Visual Inspection, Quality assurance*

## Introduction

The fuel bundle of Indian 540 MWe PHWR (Pressurised Heavy Water Reactor) consists of 37 cylindrical fuel elements arranged in a concentric ring of 1,6,12, and 18 configurations. A robotic system welds all the fuel elements with end plates with pre-defined welding parameters like current, time, and pressure. The robotic system then captures and displays the image of the welded assembly on a monitor (Fig.1). Visual inspection by an operator confirms the weld quality for all the pins. However, inspecting all the fuel pins requires a very high level of focus and can cause visual fatigue to operators, thus increasing the risk of the wrong inspection. Traditional machine vision methods based on feature extraction cannot meet the quality control requirements, mainly because of the variable illumination conditions and inconsistent shape and size of the defects. However, identifying surface defects from images using deep learning techniques is an active research topic [1,2,3]. One key challenge in using neural network methodology is collecting sufficient number of labeled defective samples. Further, when defective samples are insufficient, artificially generated images are needed to augment the dataset [4].

## Classification of Weld

Presently, the visual acceptance criterion followed for a pin is to verify the presence of two spot weld marks on either sides of the end plate (Fig.1). Electrodes leave these marks after welding. Three categories are defined based on weld marks (Table 1).

- Normal.
- Missing spot weld marks.
- More than two spot weld marks.

Our framework checks each pin for missing or additional spot weld marks. In case of discrepancies, the operator isolates the bundle and investigates further.

*Author for Correspondence: Sanjeev Sharma
E-mail: ssharma@barc.gov.in

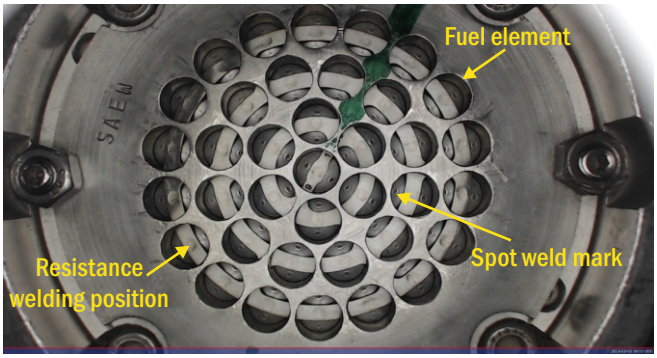


*Fig.1: Fuel elements welded with end plate.*

*Table 1: Classification of weld quality.*

| Class | Descripti on | Image | % of total images |
|---|---|---|---|
| Type - I | Normal |  | 99.09% |
| Type - II | Missing spot weld mark |  | 0.008 % |
| Type - III | More than two spot weld mark |  | 0.002% |

## Image Dataset for Supervised Learning

An automated system captures an image of 37 fuel pins welded with an end plate after the completion of welding. Though more than 3000 bundle images are available, very few cases have pins of Type-II and Type-III (Table 1). This anomaly results in a distribution where class labels are not equal for three categories. The skewed distribution makes neural network learning algorithms less effective, especially in predicting minority class examples. Therefore, we have developed methods for the artificial generation of Type-II and Type-III cases.

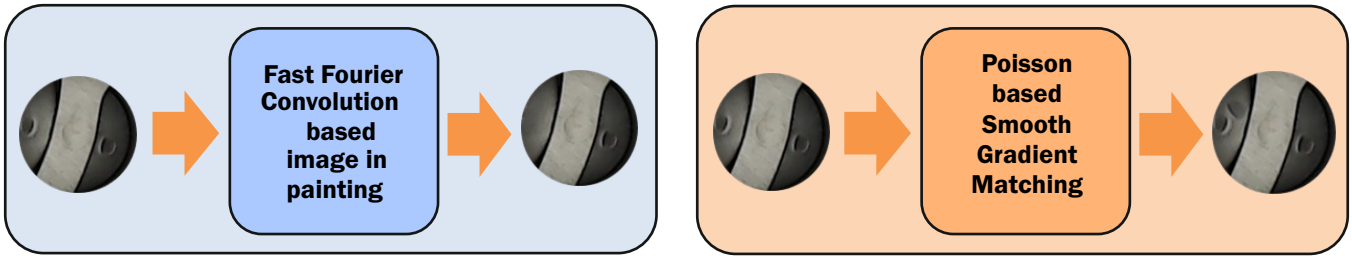


**(a) Artificial generation of Type II images** **(b) Artificial generation of Type III images**

*Fig.2: Augmentation of training dataset.*

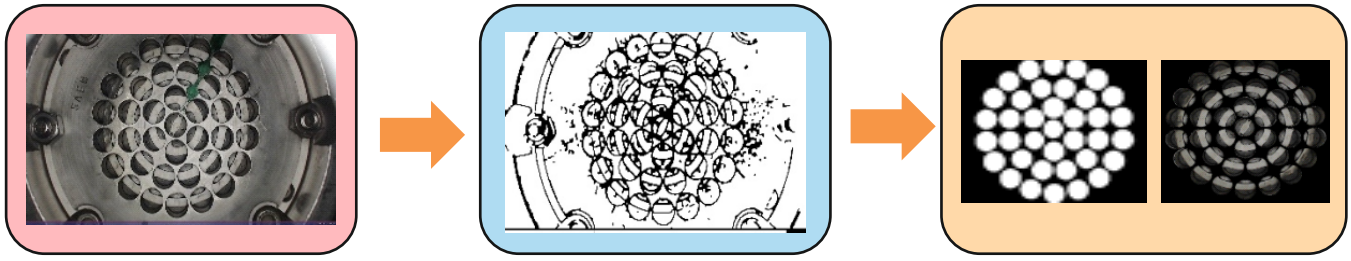

**Fuel bundle with end plate** **Pre-processed image after smoothening and edge detection** **Boundary masks and segmented pins of fuel bundle**

*Fig.3: Generation of boundary mask and segmentation of fuel pin elements.*

### Artificial Generation of Type-II images

We use a method based on Fast Fourier Convolutions (FFCs) [5] for generating the images with the missing weld impressions (Type-II). Our framework selects a mask for removing the weld mark and gives it as input to FFC for processing. It does the filling, keeping the content awareness of the regions, and therefore creates smooth boundaries as if the weld was missing at that spot (Fig.2a).

### Artificial Generation of Type-III images

The idea here is to crop spot weld marks from one image and clone them at suitable locations in the other Image. An important point here is to match the gradient of the spot weld mark image with the target image. A Poisson-based solution [6] for seamlessly merging the source image patch into the destination image has been used (Fig.2b).

### Image Preprocessing and Segmentation of Individual Pin

The fuel bundle image used for the final visual inspection has 37 fuel pins welded with end plates. Hence, it is required to segment individual fuel pins for supervised training and classification with a neural network model. Following image preprocessing and segmentation algorithms are applied to produce boundary masks and isolated pin images for further processing (Fig.3):

- Image smoothing using the Gaussian Filter to remove noise.
- Edge detection with Laplace of Gaussian with Zero Crossing.
- Image Thresholding to get a binary image.
- Hough transforms with the tuned parameters to produce the Image's desired pins boundaries (mask).

The software developed uses the mask generated above and applies it to the input image for segmenting individual fuel pins. Thus, each fuel bundle image generates 37 fuel pin images for the training and classification of deep neural networks.

### Deep Learning Architecture

Network-based on Inception and ResNet architecture (Fig.4) has achieved good performance for detecting spot weld marks as compared to typical deep learning architectures. The Inception ResNet block combines multiple filters of various sizes with residual connections. This feature not only helps in convergence but also reduces the training time of the network. This network has been pre-trained on a large dataset for object detection and segmentation. Our framework uses a transfer learning approach to classify three weld categories. Fig.5 shows isolated fuel pin images batch-processed by a deep learning network to produce superimposed classification results on fuel bundle images.

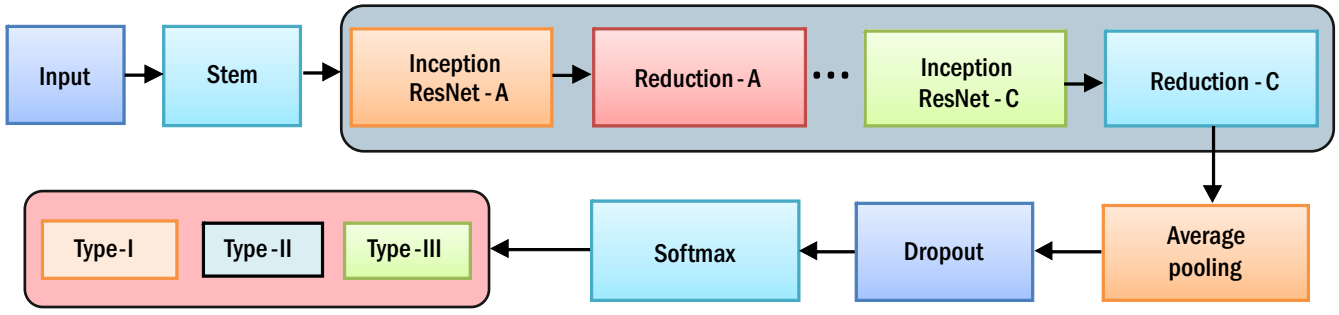


*Fig.4: Deep learning architecture based on Inception ResNet-V2.*

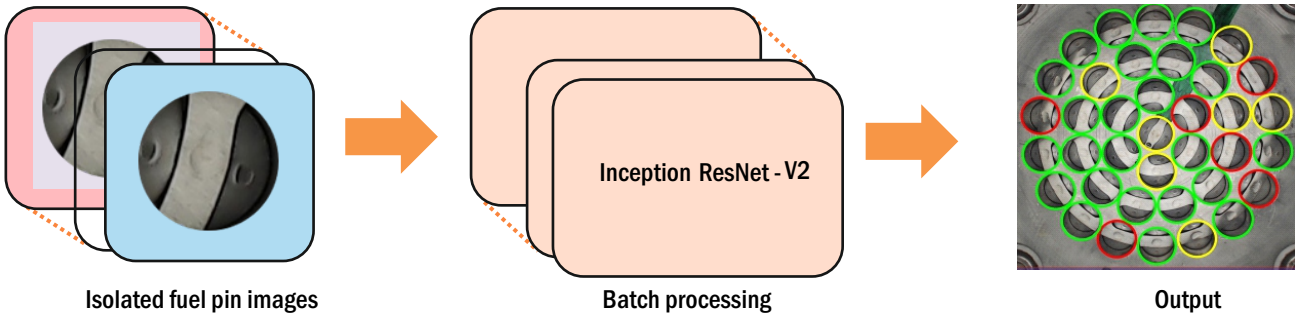


*Fig.5:Inspection system based on deep learning system. Following convention is used for depiction of weld quality, Green: Type-I, Red: Type-II, Yellow: Type III.*

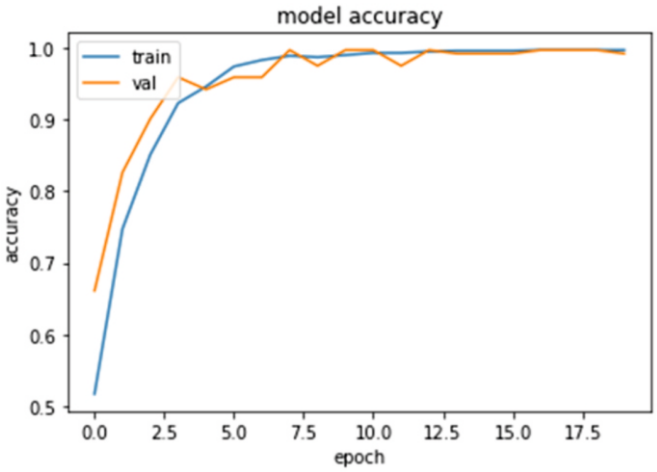


*Fig.6: Training and validation accuracy of deep learning model.*

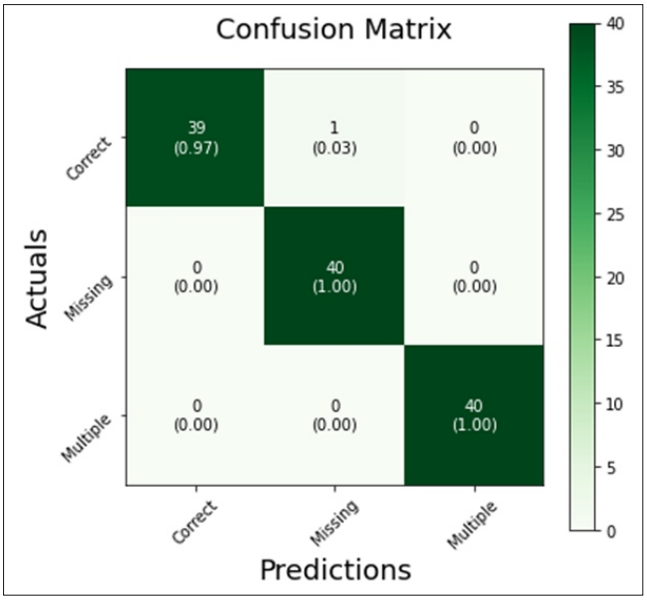


*Fig.7: Evaluation of deep learning model with test data.*

## Results

We performed model training for 20 epochs on a total of 1200 images. The dataset used for training has uniform distribution across Type-I, Type-II, and Type-III instances (400 each). We also validated the model with 120 images (40 for each class). Fig.6 shows that both the training and the validation accuracy increased with the number of epochs, and there is no over fitting or under-fitting.

The training accuracy is 0.9928, and the validation accuracy is 0.9918. Fig.7 shows values of the confusion matrix over the predictions on the test data. There is only one misclassification, where Type I (Normal) classifies as Type II (Missing spot weld mark). Detail investigation revealed that the weld mark was barely visible due to the camera position. The mean precision and recall computed from the confusion matrix are 0.9918 and 0.9916, respectively.

## Conclusions

We have developed a framework for automated inspection of end plate weld with nuclear fuel pins. The proposed method achieves mean precision of 0.9918 and a mean recall of 0.9916 with test images. Initial tests on the production floor show promising results. The system is undergoing rigorous performance testing by deliberately creating Type-II and Type-III spot welding marks.

## Acknowledgements

Authors thank Dr. Komal Kapoor, Chairman and Chief Executive, NFC (Nuclear Fuel Complex) for conceptualization, initiation, support and encouragement during the development of the project.

## References

[1] Bhatt, Prahar M., et al. “Image-based surface defect detection using deep learning: A review.” Journal of Computing and Information Science in Engineering 21.4 (2021).

[2] Das, Subrata, et al. “Deep learning convolutional neural network for defect identification and classification in woven fabric.” Indian Journal of Artificial Intelligence and Neural Networking (2021).

[3] Shinde, Prashant et al. "Wafer Defect Localization and Classification Using Deep Learning Techniques.” IEEE Access (2022).

[4] Jain, S., et al. Synthetic data augmentation for surface defect detection and classification using deep learning. J Intelligent Manufacturing Vol 33, 1007–1020 (2022).

[5] Roman Suvorov, et al. “Resolution-robust Large Mask Inpainting with Fourier Convolutions.” Winter Conference on Applications of Computer Vision (WACV 2022).

[6] Patrick Perez, et al. “Poisson image editing”. ACM Transactions on Graphics (2003).

# Design and Development

3

# A Passive Bi-directional Safety Relief Valve for Nuclear Applications

**Nagaraj Alangi*, Mukesh Kumar Verma, Dev Ranjan Das, Soumitra Kundu and Sanjay Sethi**

*Advanced Tunable Laser Applications Division, Beam Technology Development Group, Bhabha Atomic Research Centre, Trombay – 400085, INDIA*

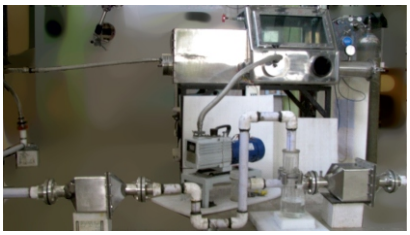

*SRV proof of concept setup*

ABSTRACT

Inert atmosphere glove boxes with attached glove ports typically of 200 mm and 160 mm diameter are extensively used for handling toxic and radioactive materials. Pressure regulating valves are conventionally used and beyond its specified limits regulation of the glove box pressure may be compromised. In this work, we report design, development and testing of a passive, compact, prototype safety relief valve (SRV) with silicone oil as bubbler fluid to mange the glove box pressure, both in dynamic as well as in the isolated condition. The onset of the relief and the transient glove box pressure were measured as a function of flow in the range of 0-60 lpm and always found to be at 12.5 mm ±1 mm water column (WC). The glove box when evacuated using rotary pump with nominal pumping speed of 16 $m^3$/h reached a maximum negative pressure of 177 mm of WC, which was within the desired safety limit. During its extensive testing, the SRV functioned at the set boundaries with the desired sensitivity and proves its application in the safe glove box operations.

KEYWORDS: *Prototype safety relief valve, Engineered safety feature, Glove box safety*

## Introduction

Bhabha Atomic Research Centre (BARC) utilizes a number of inert atmosphere glove boxes with attached glove ports typically of 200 mm and 160 mm diameter, and which house toxic and radioactive materials [1-6]. Several operations are undertaken in the equipment housed in the glove boxes such as vacuum treatment, annealing, sintering, attrition, melting etc. Generally, the ventilation system in the glove boxes is once through type in which an inert gas is flowed in the glove box through the gas inlet line and discharged into the exhaust line which drives to the stack after passing through various stages of HEPA filters. In practice, the radioactive material is handled in the glove box at -25 mm water column (WC) ±12.5 mm WC pressure (negative guage pressure) and the dynamic negative pressure is maintained in the glove box using a pressure regulating valve (PRV) installed on the exhaust side of the glove box. The pre installation setting of the PRV is done for a specified pressure and flow of the exhaust system to maintain -25 mm WC and regulate the glove box pressure within ±2.5 mm WC accuracy. Beyond the specified limits of exhaust line pressure and gas flow, regulation of the glove box pressure may be compromised. Similarly, when the glove box is isolated by closing the inlet and outlet valves as is the normal practice, PRV cannot regulate the pressure in the glove box.

There are a number of scenarios in which the glove box is either over pressurised or under pressurised from the nominal operation conditions. An isolated glove box can be over pressurized due to increase in the glove box temperature, inadvertent leak of any pneumatic line inside the glove box, heat/gas released due to chemical reaction and malfunction of the inlet gas cut-off valve. Under-pressurization of an isolated glove box can be due to a leak in any of the vacuum boundaries of the equipment housed in the glove box. Similarly, under-pressurisation of the glove box can also be witnessed in a ventilated glove box when the flow due to leak in the vacuum boundary is more than the inlet gas flow. An extreme condition of glove box can result when the vacuum pump is directly evacuating glove box due to a catastrophic failure of a component.

In the glove box, the gloves denote a hazard, in that they could get detached if the glove box were accidentally over pressurised or under pressurised thereby releasing radiotoxic material to the laboratory environment. Beyond the pressure gradient design limits of the glove box panel, the panel may crack, break or develop leak, thereby release the radiotoxic material to the laboratory environment. In some laboratories, as a precautionary measure the glove boxes are fitted with active pressure relief devices which will vent into a dedicated exhaust system and not into the laboratory [7]. The pressure relief setting is generally set to limit the difference between the glove box pressure and barometric pressure in the laboratory, since it is this pressure difference which causes the gloves to detachment. Dedicated passive over pressure relief devices for glove box are reported by several groups based on bubbler devices using suitable liquid [8,9,10].

Active pressure relief devices are available for the wide range of the requirements, but they stop functioning in the event of a station blackout condition, which is undesirable. Spring loaded relief valves are available for the wide ranges of pressure, which are extensively used for high pressure applications, however at near atmospheric ranges these spring-loaded valves are not thoroughly reliable. Mercury bubblers are widely used in different laboratories to relieve the over pressure of glove box by bubbling through mercury and the set-point set by the hydrostatic head. Several designs of check valves are reported for mercury bubblers to isolate the glove box [9]. Rupture disk type of safety relief valves are not an option for laboratories handling toxic and radioactive

*Author for Correspondence: Nagaraj Alangi
E-mail: nagaraj@barc.gov.in

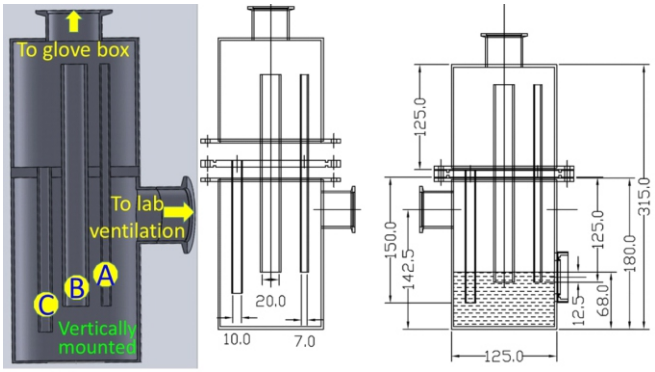


*Fig.1: Engineering drawing of bi-directional safety relief valve.*

materials. There is no reported literature available on the safety relief valve which is functional both during over pressure and under pressure.

Engineered safety features for glove box are designed to protect the worker from hazards. Eliminating the hazards is the preferred control; however, a hierarchy of controls are being used to implement feasible and effective controls. Protection of the worker is dependent on active and passive controls, good work practices, training, ergonomic consideration, and housekeeping. Hence to mitigate the hazard of glove detachment, the need is for a device which functions as a passive pressure relief device and is sensitive to room barometric pressure, but not the downstream pressure in the exhaust line. The same device shall also function as a passive check valve to limit glove box pressure within the specified range. This forms the motivation for this developmental work.

In this work, we report the design, development and testing of a passive, compact, prototype safety relief valve (SRV) with silicone oil as bubbler fluid to limit the glove box pressure, specifically when the glove box is in an isolated condition. This SRV proposed is a passive device with no mechanical components and the device can function at both positive and negative set pressure boundaries.

## Design Considerations and Functionality

### *Description and functionality*

The bidirectional safety relief valve essentially contains two cylindrical compartments one above other, connected with three tubes of different sizes (tube A, B and C), each tube serves a different functional requirement. Fig.1 shows the drawing of the SRV. The top cylindrical compartment is connected to the glove box and the bottom compartment is connected to piping exposed to the laboratory exhaust. The connections of both the cylindrical compartments to respective piping's are O-ring based quick connect fittings for ease of maintenance. A viewing window in the SRV serves to monitor the fluid level. Tubes A and B are immersed in the silicone oil contained in the bottom cylindrical chamber. In the normal conditions, the immersion of these tubes in silicone oil isolates the glove box from the ambient atmosphere. The schematic of the layout of the SRV for implementation in the actual application is as show in Fig.2. The HEPA filters prevent the release of toxic particulates from glove box to the ambient atmosphere. The U bend in the pipe line serves as an accumulator for any oil droplets carried away by the air ingress to the glove box under extreme under pressurisation.

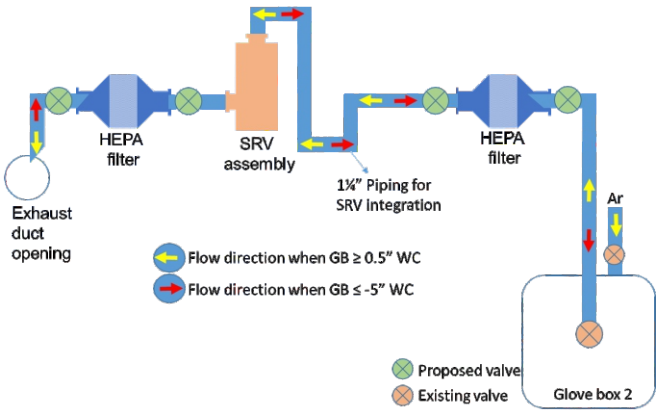


*Fig.2: Schematic of the layout of the SRV for implementation.*

The over-pressure relief of glove box is obtained by the submerged vent line (tube A) in a silicone oil reservoir, the relief pressure being a function of the submerged depth and is maintained at 12.5 mm. The choice of the bubble fluid is detailed in the selection of materials section. The gas released is filtered through HEPA filters, one placed before the SRV and another after the SRV in the piping layout. The type of gas (Ar, $N_2$, He or air) was not having strong influence on the release pressure [9]. Initially when the over pressurization is relatively less, bubbling happens through the tube A, which is favourable for bubble formation owing to its smaller size. However, if the flow of gas causing over pressurization is more, both tubes A and B will participate in the venting.

In the event of under-pressurisation of the glove box, all the three tubes commence sucking of oil into the tube. Eventually, there comes a point at which the oil level has reached below level of tubes A and B, there by exposing the cross-sectional area of both the tubes A and B. At this point, the fall of oil plug in the tube due to gravity is balanced by the opposing force of vacuum in the glove box. When the glove box is further under-pressurized, the oil plug moves up and enters in to the top cylindrical chamber. At this point, the tubes are clear of oil and allow air into the glove box. The oil from the top cylindrical chamber is returned to the bottom cylindrical chamber through tube C. At a given flow of air, which is a function of the under pressurization, there is a dynamic balance between the suction of the oil through the tube A and B and return of oil via tube C. The maximum negative pressure perceived by the glove box in the event of under pressurization is a strong function of the air flow into glove box. At a given sizing of pipe and route, the pressure drop across all the elements decide the maximum flow achieved.

Hence, the peak negative pressure perceived by glove box is directly related to the extent of under pressurization and air flow rate achievable. The onset of the under-pressure relief of glove box is a function of the total volume of the fluid sucked through all the vent tubes, which clears the vent lines A and B for air inrush.

### ***Design and sizing considerations***

- It should be compact and light weight and sufficiently protected for avoiding any damage due to mild external impact.
- The piping size shall be chosen to achieve the desired flow of air/gas with acceptable pressure drop across all the components.
- The fluid used in the SRV should not result in more than 1 ppm concentration of its vapour in the glove box during normal operation of glove box.

- A provision shall be available to measure/monitor the fluid level in the SRV, there by quantity of the fluid.
- The SRV module should have replaceable HEPA filters at both the ends to be connected to glove box and the vent line respectively.
- Mist eliminator should be provided between the HEPA filter and fluid line/container of the SRV to avoid its blocking of HEPA filters.
- Provision shall be available to monitor health of SRV system by periodic testing of its performance for onset of release of excess positive & negative pressure, rate of release of pressure.
- All the connections and joints shall be 'O' ring based with quick connect fittings for ease of handling and convenience in achieving suitable leak tightness.

### *Limits of operation*

The SRV is to be meant for relief of excess positive or excess negative pressure in the glove box directly to the exhaust duct of room ventilation. The onset of release of excess positive pressure of glove box only shall be at +12 mm WC ±2 mm WC and release of excess negative pressure of glove box shall occur at –125 mm WC ±5 mm WC. The SRV shall maintain a seal to prevent exit/entry of air in between +12.5 mm WC and –125 mm WC of glove box pressure. The rate of release of excess positive pressure in the glove box should be ≥60 lpm with glove box at 25 mm ±2 mm WC. This scenario is envisaged under the conditions of failure of regulation by PRV and inert gas flow solenoid valve is malfunctioning. Similarly, the rate of release of excess negative pressure in the glove box should be more than 200 lpm with glove box maintained at -180 mm ±5 mm WC. This extreme flow is observed when there is a breach of vacuum seal or catastrophic failure of glass window attached to vacuum chamber either in the dynamic pumping or isolated condition.

### *Selection of materials for SRV*

The fluid used in the SRV plays a major role in the performance of the SRV to have no contamination to the associated glove box. Ideally, the SRV fluid should be radiation resistant, oxidation resistant, explosion resistant, chemically inert, minimum combustion hazard, have low vapour pressure, recyclable, extended life without degradation of properties, less viscous and non-wetting. Water is generally used in many bubblers; however, it has the disadvantage of high vapour pressure thereby increasing the moisture concentration in the inert glove box. Mercury is also used in SRV for glove box, however not considered in the current study as it may not provide greater resolution and also lead to severe health hazards. Hydrocarbon oils are not considered due to their flammability and high vapour pressure. Hence the obvious choice is the silicone-based fluids; specifically, the phenyl methyl-siloxane (DC 702), tetramethyl tetraphenyl trisiloxane (DC 704) and pentaphenyl trimethyl trisiloxane (DC 705) fluids which have very low vapour pressure at room temperature and are stable over longer duration of time. Out of the listed silicone-based fluids, DC 704 was chosen keeping in view of its vapour pressure, availability, stability, cost and vast experience in handling the fluid in the vacuum generation systems. Some indication of the holdup of oil in the steel components was derived from the experience of diffusion pump before finalizing the fluid for SRV. Table 1 shows properties of silicone based fluids.

*Table 1: Physical properties of silicone based fluids.*

| S.No | Specifications | DC 702 | DC 704 | DC 705 |
|---|---|---|---|---|
| 1 | Vapor Pressure at 25°C (torr) | $1x10^{-6}$ | $1x10^{-7}$ | $1x10^{-9}$ |
| 2 | Boiling Point at .5 torr (°C) | 180 | 215 | 245 |
| 3 | Viscosity at 25°C (cSt) | 45 | 39 | 175 |
| 4 | Flash Point (°C) | 193 | 221 | 243 |
| 5 | Density at 25°C (g /ml) | 1.07 | 1.07 | 1.09 |

The materials used for fabrication of the SRV have several considerations such as transparency, fabrication ease, surface condition, radiation resistance, amenable to coating, compatibility with both SRV fluid and the ambient air and SRV fluid hold up. One of the important considerations is the SRV fluid holdup which decides on the extent of the fluid participating in the SRV functionality. If the holdup of oil is more on the internal walls of the SRV, the onset of relief in both over pressurisation and under pressurisation occurs earlier than the designed value. Hence, careful selection of materials is necessary to have reliable functionality of the SRV. Transparent materials such as quartz, glass and Perspex were not considered for the construction of SRV as they are likely to be damaged due to mild impact; however, quartz window with suitable protection is used as a fluid level indicator (level sensor was not chosen considering passive design). In this study, SS304 has been chosen as the material of construction of the SRV due to ease in fabrication and availability. Based on the separate study of the contact angle of silicone fluids with different materials, a suitable coating of Teflon is proposed on all the internal surfaces of SRV for minimal holdup of SRV fluid.

### *Instrumentation requirements*

The SRV shall be supported by reliable instrumentation for different aspects. Instruments are required for measuring and transmitting the glove box pressure and temperature, detect the onset of the SRV and generate an alarm, measure and transmit the pressure drop across the HEPA filter during flow conditions and flow measurement during testing conditions. The Magnehelic gauge being the industry standard to measure pressure drop across HEPA filters are used to determine choking of HEPA filter. Pressure transmitters for both under and over pressurisation are connected to glove box to measure and transmit the real time data. RTD based temperature transmitter is used to measure the temperature of the glove box. A high-speed data logger records all the data transmitted by the instruments for the presentation of historical trends and observation of transients during testing.

### *Periodic testing method*

A dedicated arrangement for period testing of SRV is necessary to test the reliability and efficacy of the SRV. The schematic of the layout for periodic testing is as shown in Fig.3. A dedicated testing line branching from the SRV line is connected to the glove box exhaust through a HEPA Filter for testing the SRV for relief from under pressurization. For testing the SRV in over pressurization, a gas line is connected to pipe after the first HEPA filter as shown in the layout. Any makeup of the SRV fluid can be done by opening the 6.4 mm compression fitting in the lower cylindrical compartment.

### *Experimental testing and validation*

The SRV was tested extensively in multiple stages of development. Initially the proof of concept was demonstrated using an SRV fabricated out of Perspex to witness the

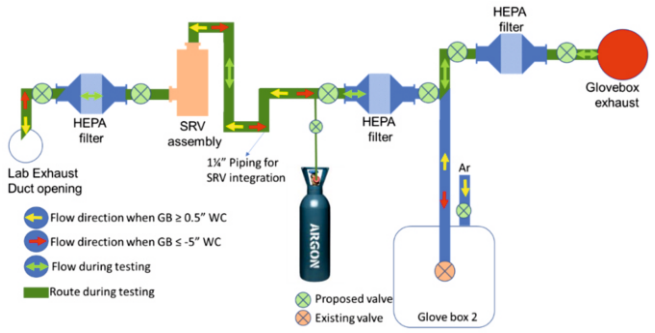


*Fig.3: Schematic of the layout for periodic testing of the SRV.*

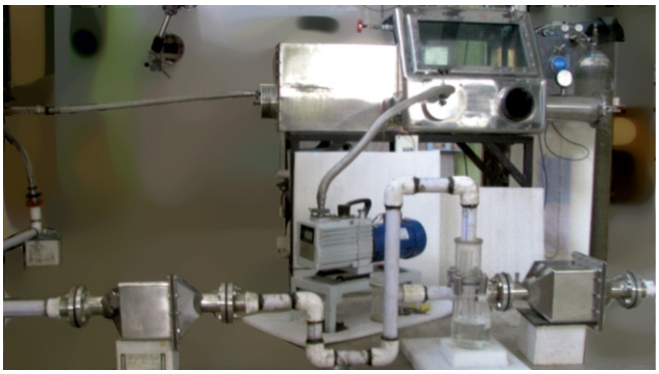

*Fig.4: Photograph of the SRV proof of concept setup.*

activation of SRV at both the set pressure boundaries and water was used as the SRV fluid. The proof-of-concept set-up of the SRV is shown in Fig.4 in which the top cylindrical portion of SRV was connected with an inactive test glove box using 1¼" PVC piping along with the HEPA filters and bottom cylindrical portion of the SRV was kept open to atmosphere via HEPA. Argon gas was used to create positive pressure in the glove box and 8 $m^3$/h rotary pump with a control valve was used to generate negative pressure in the glove box. A photohelic gauge (0-4" WC) was used to precisely measure and control the positive pressure of the glove box and a water manometer with ±1.0 mm WC accuracy was used for measurement of absolute pressure in the glove box.

Subsequent to the demonstration of the proof of concept, a SRV made of SS304 was fabricated with the design dimensions and the piping with HEPA filters was retained for testing. The schematic of the layout for testing is as shown in Fig.5. A rotary pump of 16 $m^3$/h was used to evacuate the glove box of 1 $m^3$ volume and argon gas was used to pressurise the glove box. The glove box had all the necessary pressure transmitters connected to a data logger for recording of the glove box pressure during the entire period of testing.

The pipeline length, elbows, HEPA filters were chosen based on the envisaged site layout requirement and PVC pipes of same dimensions were used for testing. Flow of over pressurization gas was measured using a rotameter and flow during under pressurisation was measured at the exhaust of the rotary pump using an anemometer. The value of flow calculated for each reading was an average of at least 5 readings recorded during the testing. A water manometer with ±1.0 mm WC accuracy was used for measurement of guage pressure in the glove box supplemented by the Magnehelic guage mounted on the glove box.

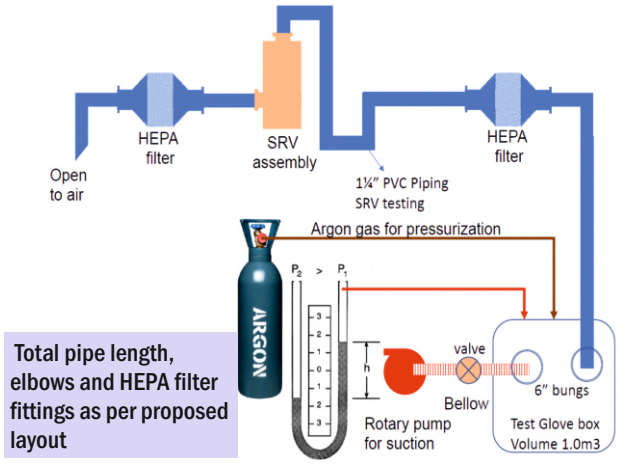


*Fig.5: Schematic of the layout for testing of SRV.*

## Results and Discussions

The bidirectional passive SRV uses the barometric pressure in the laboratory as a reference for the relief pressure and remains unaffected by the pressure fluctuations of the glove box exhaust system. The SRV was tested by connecting to a test glove box which was having a leak tightness of 0.05 volume %/h and volume of 1000 L. Four gauntlets were also used on the glove ports to check for any glove detachment during extreme pressure conditions within the testing limit. The developed SRV assembly must function during the three following different states of the glove box conditions.

### *The Glove box at nominal operating pressure*

Glove boxes are generally evacuated as normal procedure when establishing an inert atmosphere inside and maintained at a pressure slightly below the barometric pressure in the laboratory. The SRV assembly must therefore act as an isolation valve, and not allow flow into the glove box under this circumstance. This functionality is accomplished by the tubes immersed in the silicone oil. When the glove box is slightly (-1" WC) below the barometric pressure in the laboratory, the silicone oil rises up the tubes until the balance of suction and gravity is established without any further rise of oil up the column. Small oscillations occurring due to the operations in the glove box are accommodated by the slight oscillations of oil level of oil in the tubes of SRV and isolation is always maintained.

### *Glove box venting under over pressurisation*

Should the pressure rise in the glove box, the silicone oil in the tubes of SRV is displaced into the cylindrical reservoir until the pressure is not sufficient to generate a bubble. When the over pressurisation continues in the glove box and the flow is low, all the oil in the tubes is displaced until it reaches the bottom of the tube. At this condition, any further flow leads to escape of the gas from the glove box and will rise up through the oil leading to the laboratory exhaust system. This bubble formation happens preferably at tube A as it has the most favourable tube diameter for bubble formation. The setting of the relief pressure is determined by the depth of tube immersed below the level of the silicone oil, in this case 12.5 mm. The onset of the relief and the transient glove box pressure was measured as a function of flow in the range of 0-60 lpm. In the range of the study with DC704 as bubbler fluid, the onset of relief was always found to be at 12.5 mm ±1 mm WC. The glove box pressure monotonously increased with increase in the over pressurisation flow and reached a maximum of 24 mm WC at 60 lpm and continued to maintain at that flow as shown in Fig.6.

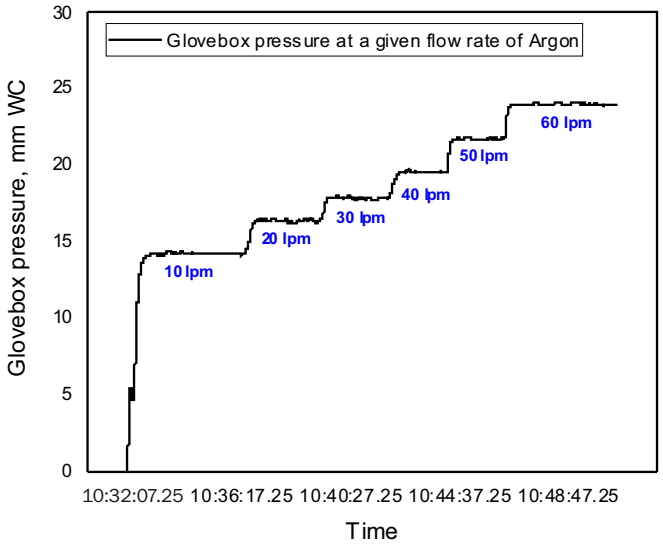


*Fig.6: Glove-box pressure at different flow rates under over-pressurization condition.*

Argon, helium and nitrogen were used to pressurize the glove box to study the effect of gas. No significant difference was observed either on the onset of relief or the peak positive pressure as anticipated. It should be noted that all the tests were done by pressurization of an isolated glove box, and in a ventilated glove box the pressure is regulated by the PRV and it may never be over pressurised.

### *Glove box under vacuum*

Glove boxes are evacuated as normal procedure when establishing an inert atmosphere inside and the suction is regulated by the PRV. When a glove box envelops a vacuum chamber, which is under dynamic vacuum, the leak or failure will lead to evacuation of glove box limited by the capacity of the rotary pumping system. As the evacuation of the glove box by the rotary pump can lead to more under pressurisation than leak in an isolated chamber, this scenario was chosen for testing of SRV. Table 2 shows the results from the testing of the SRV in which the onset of the relief and the maximum pressure during under-pressurization are tabulated with respect to flow obtained with the different sized fittings used to connect the rotary pump and a glovebox of 600 L.

As can be seen from the Table 2, when a glovebox is evacuated by rotary pump of 16 $m^3$/h through a 3/8" valve, the flow was relatively less due to the pressure drop across the valve. When the valve was replaced with a quick fitting opening with 22 mm diameter clear opening, the flow increased. When both the connections to glovebox (SRV and rotary pump) were replaced with quick fitting opening with 22 mm diameter, maximum flow of 13.3$m^3$/h was achieved with a nominal rotary pump speed of 16 $m^3$/h. It can be observed that the onset of relief during under pressurization was similar in all the tests.

*Table 2: Glovebox pressure maintained during the testing of SRV.*

| Measured velocity, m/s | Calculated flow, $m^3$/h | Onset of flow, mm | Glove box pressure, mm of $H_2O$ (600L volume) | End connections of piping |
|---|---|---|---|---|
| 3.9 | 6.9 | -125 mm±5mm | 130 mm±2mm | 3/8" valve |
| 6.3 | 11.1 | -125 mm±5mm | 130 mm±2mm | One 22 mm Diameter pipe |
| 7.5 | 13.3 | -125 mm±5mm | 185 mm±2mm | Two 22 mm Diameter pipe |

However, the glovebox pressure was more negative when the flow was higher for obvious reasons. The major pressure drop occurs at the HEPA filters and the SRV assembly, contribution to the pressure drop from other segments of pipe is negligible.

The test was repeated with a 1000 litre glove box with a data logger to collect 8 data points per second. The variation of the glove box pressure with time when evacuated using rotary pump with nominal pumping speed of 16$m^3$/h is as shown in Fig.7. The maximum negative pressure of glove box was 177mm of WC. When the test was repeated after duration of ~600 sec, the maximum negative pressure of glove box was 197mm of WC with the same rotary pump. The reason for this behaviour is attributed to the time required for the oil to totally drain back to the reservoir, whose level regulates the dynamic sealing during the air inrush. The test when repeated after a period of 24h again for few minute resulted in a maximum negative pressure of glove box was 177 mm of WC as shown in Fig.8 which confirms the hypothesis. Although the testing at different times, the glove box pressure never reduced below 180 mm WC except when repeated immediately.

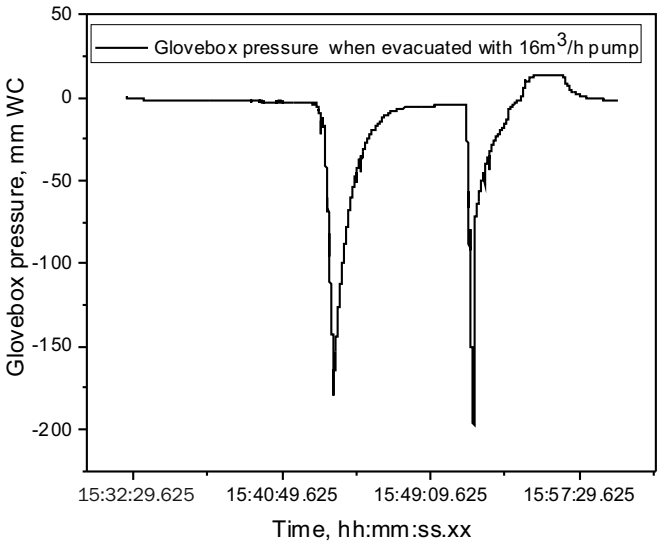


*Fig.7: Glove box pressure during under-pressurization by rotary pump evacuation.*

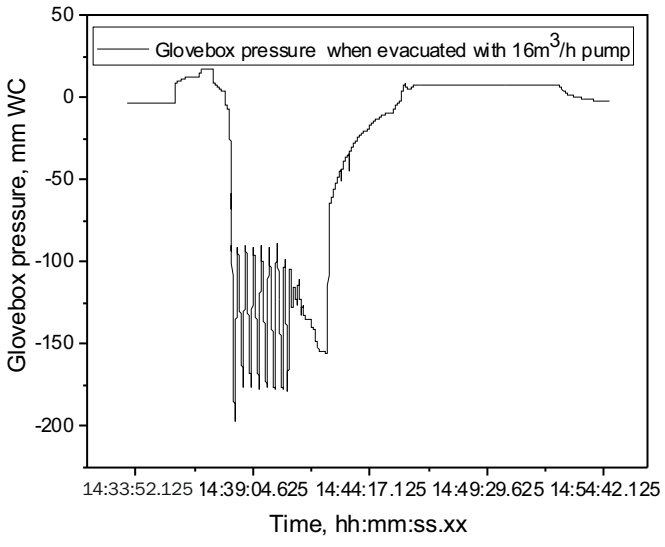


*Fig.8: Glove box pressure during under-pressurization by rotary pump evacuation after 24h of previous test.*

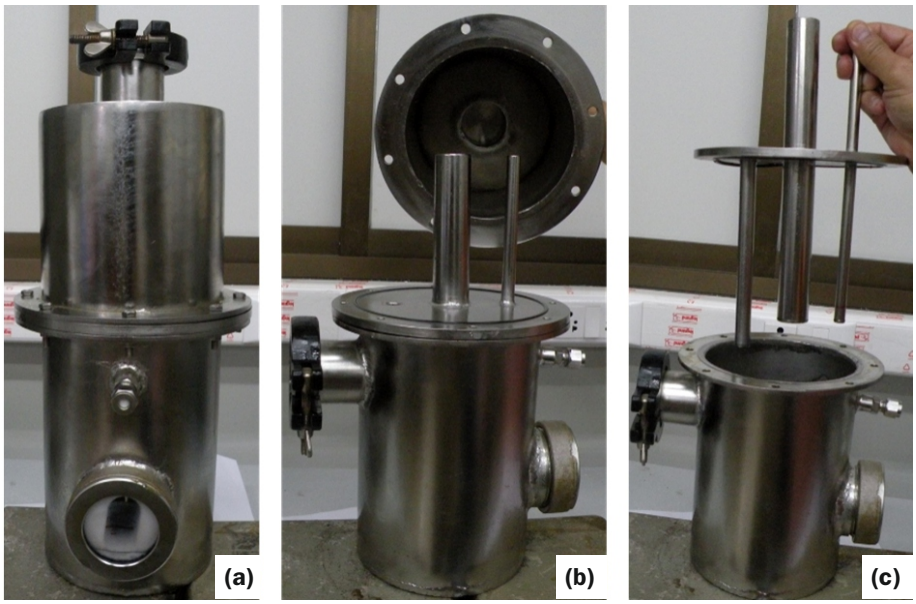


*Fig.9: (a) SRV in assembled condition (b) SRV with top cylindrical section open (c) SRV with bottom cylindrical section and the plate with tubes.*

Consecutive activation of SRV is not envisaged in actual scenarios as an alarm is generated for human intervention. When the rotary pump was turned off, the glove box pressure reached around 125 mm which is the onset limit. The test was repeated several times to check the reliability and functional limits, and the onset and the maximum negative pressure was within the limits observed. The photographs of the prototype SRV are as shown in Fig.9.

## Conclusions

A passive bidirectional SRV has been designed, fabricated and tested for its functionality and found to function suitably for both over pressurisation and under pressurisation of the glove box. During its extensive testing, the SRV functioned at the set boundaries with the desired sensitivity. Its compact design and passive nature have proven its expediency in the safe glove box operations. This SRV also demonstrates the capability of having the glove box, if required without human presence over an extended duration of time. This SRV designed finds application in all glove boxes with nominal operating pressure above or below the atmospheric pressure, and tailoring of oil level is necessary to set the activation limits.

## Acknowledgements

Authors acknowledge with thanks, support and guidance from Dr. Archana Sharma, Director, Beam Technology Development Group, BARC. The authors gratefully acknowledge Jaya Mukherjee and Anupama P. for their valuable suggestions and discussions. The authors thank S. P. Dey for offering insightful feedback, which helped consolidate the ideas. The assistance of K. Karmakar and S. B. Gaikwad in carrying out the experiments is also appreciated.

## References

[1] P. R. Roy and C. Ganguly, "Plutonium metallurgy in India" Bull. Mater. Sci., Vol.6, No.5, September 1984, pp. 923-958.

[2] Kamath, H. S., Majumdar, S., & Purusthotham, D. S. C. (1998). Developments in MOX fuel pellet fabrication technology: Indian experience (IAEA-TECDOC-1036). International Atomic Energy Agency (IAEA).

[3] J. P. Panakkal, Non-destructive characterization of plutonium bearing nuclear fuels for fast and thermal reactors, Proceedings of the National Seminar & Exhibition on Non-Destructive Evaluation, NDE 2011, December 8-10, 2011.

[4] A. K. Mishra, B. K. Shelke, M. K. Yadav, Mohd. Afzal, Arun Kumar, G. J. Prasad, Developments in fabrication of annular MOX fuel pellet for Indian fast reactor, International Conference on Fast Reactors and Related Fuel Cycles: Safe Technologies and Sustainable Scenarios (FR13), 4–7 March 2013, Paris, France.

[5] R. B. Bhatt. G. Ravi Kumar (Eds.). (2018). Experience and Developments in Fabrication of MOX Fuel at Advanced Fuel Fabrication Facility, BARC Newsletter Founder's Day Special Issue, 2018.

[6] Aneesh, T., Usha, S., Chandran, Neeraja, Devi, S. Sagunthala, Kumar, D. Shravan, Mahildoss, D. Jebaraj, & Ananthasivan, K. Pujari, P. K., & Pai, R. V. (Eds.). (2021). Integrity testing and qualification of glove boxes by pressure decay method. 15th Biennial DAE BRNS Symposium Nuclear and Radiochemistry (NUCAR2021), Feb 22-26, 2022, BARC, Mumbai.

[7] Hu, Ming-Sen. The Design and Development of Control System for High Vacuum Deoxygenated and Water-Removal Glove Box with Cycling Cleaning and Regeneration. 10.5772/intechopen.80423. (2018).

[8] Blaedel, K. L. Glovebox pressure relief and check valve (UCID–20695). United States. (Mar 1986).

[9] Clayton G. Turner, Aaron L. Balsmeier, and Ryan J. Shawler, Bubbler Flow Testing, Enclosure, Summer, 2019.

[10] ISO 10648-1:1997, Containment enclosures — Part 1: Design principles.

# Applications of Artificial Intelligence

4

# Predicting Properties of Glasses using Machine Learning Algorithms

**Pooja Sahu, Vishwas Tiwari and Sk. Musharaf Ali***

*Chemical Engineering Division, Bhabha Atomic Research Centre, Trombay – 400085, INDIA*

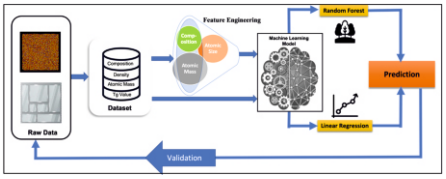


*Typical application of machine learning*

ABSTRACT

Prediction of suitable glass composition is very important and also challenging. The glass can have the possibility of having large number of probable combination of compositions, which makes it quite challenging to apply the experimental method of trial and error. The computational tools like Ab initio and Classical Molecular Dynamics simulations have very high computational cost. Machine learning (ML) is a very promising tool for predicting the properties of glass with sufficient efficiency and at a low computational cost. The ML models were built by applying feature engineering and varying the descriptors for higher accuracy. The two main ML models implemented for investigation are Linear Regression and Random Forest. We investigated two types of glasses: Sodium Borosilicate glass and Radiation shielding window (RSW) glass. The different models were built for different properties ($T_g$ value, density, and Young's modulus) and then optimized for higher accuracy.

KEYWORDS: *Classical Molecular Dynamics, Machine learning, Radiation shielding window, Young's modulus*

## Introduction

Apart from many other important uses, glasses are used for immobilization of radioactive waste and radiation shielding. In that context, tailor made glass is necessary. Glasses are known as supercooled liquid which are non-equilibrium, non-crystalline material that spontaneously relax at room temperature [1] . The glass does not require to satisfy any rigid stoichiometric rules. Glasses can be made of any element present in the periodic table if quenched fast enough from the melt state to solid state. Zanotto et al. [2] showed that there is a possibility of forming $10^{52}$ different glass compositions with 80 most useful chemical elements of the periodic table when combining them in 1.0 mol %. The experimental method of trial and error to make the glass with desired properties is expensive as well as time consuming. Computational tools like ab initio and classical molecular dynamics simulations can be used as an alternative to reduce the experimental expenses, but these computational tools have certain limitations like this can be precisely applied only for simple glass compositions containing maximum 5-6 elements. At least one simulation is required for each composition of the glass which increases the computational cost because there are a large number of compositions available.

The Machine Learning (ML) model can be used to address the complex problem in the material science by using the existing information about the glasses [3]. The ML models are built on the concept of learning from the available database. In order to use the ML algorithms to predict the properties of the new glasses, it is essential that the developed model should have high predicting accuracy. The model accuracy mostly relies on the existence of the useful data which are accurate, consistent and complete. There are many ML algorithm which can be utilized to build the model. Previous study by Cassar et al. [4] reported a successful application of a Multilayer Perceptron (MLP) artificial neural network (ANN) to predict the glass transition temperature ($T_g$) of multicomponent oxide glasses containing over 46 chemical elements. Further, Alcobaca et al. [5] showed application of different ML models to predict the $T_g$ of glasses containing over 65 chemical elements, where the random forest (RF) and k-nearest neighbors algorithm (K-NN) model had the highest accuracy as compared to other models. In these studies, the relative deviation (RD) at extreme $T_g$ (450K<; 1150K >) was shown to be higher as compared to the intermediate $T_g$ (459K<= $T_g$>= 1150K) range. The prediction of Young's modulus values was done by Yang et al. [6] using high-throughput molecular dynamics simulations and ML models to infer the relationship between glass composition and Young's modulus.

This letter reports the different ML models to predict the $T_g$ value, Young's modulus and density of the glasses, with the help of different features (% of compositions, atomic mass, atomic size and density) as input. Among the used ML models i.e. linear Regression [7] (LR) and random forest (RF) [8] , the RF model was found to have better accuracy.

## Computational Methodology

A schematic for ML application for predicting the glass properties is shown in Scheme 1.

### Dataset

For both the sodium borosilicate and radiation shielding window (RSW) glasses, the dataset used was collected from the SciGlass database, which contains 4,20,000 glasses and 2,68,000 oxide glasses. We limited our dataset to different compositions of $SiO_2$, $K_2O$, $Na_2O$, PbO, LiO, BaO and $As_2O_3$. We excluded all the compositions containing any other chemical element. In the selected dataset, the range of $T_g$ was varied from 673K-1173K, the density was ranged from 1.8 g /$cm^3$ - 9g/$cm^3$ and Young's modulus was ranged from 40GPa to

*Author for Correspondence: Dr. Sk. Musharaf Ali
E-mail: musharaf@barc.gov.in

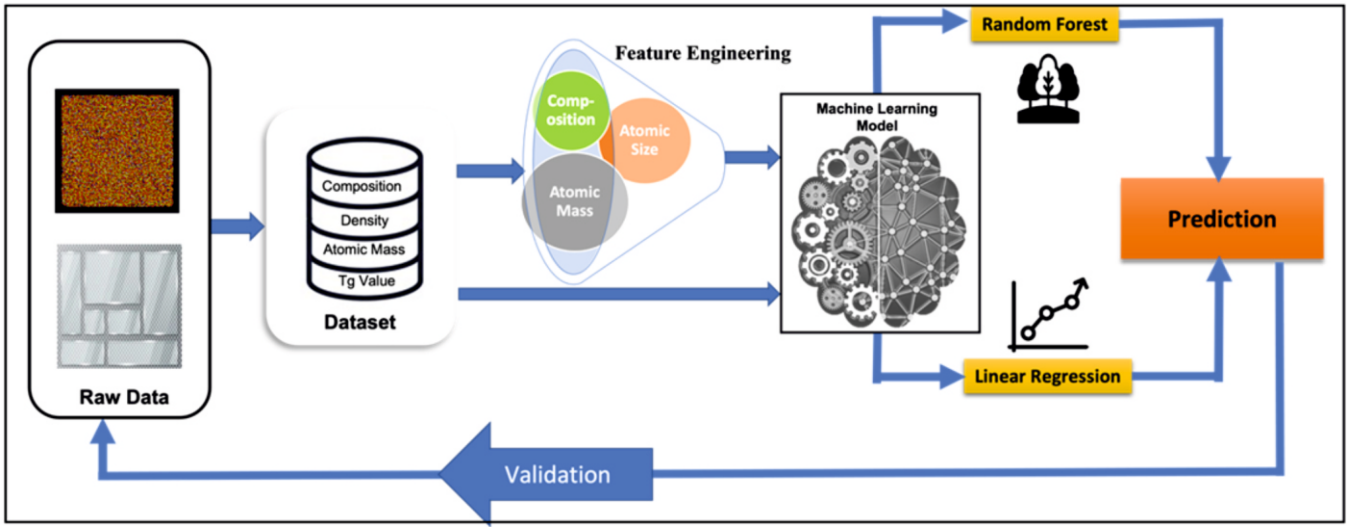


*Scheme 1. Illustration of typical application of machine learning.*

90GPa. The dataset after cleaning was reduced to greater extent $T_g$ – 1349, Young's Modulus – 659, Density – 1445. The duplicate data was removed, and the median was selected for the clean dataset. The elemental compositions are presented in Fig. 1.

### Machine Learning Algorithms and Evaluation

The ML algorithms used in present studies are linear regression and random forest. In most of the studies, the RF model has been used because it gives good predication that can be understood easily, and it is one of the few models which can perform both regression and classification tasks. The performance of the used ML models was checked by evaluating the coefficient $R^2$.

### Training and Evaluation Setup

The Feature Engineering [9] is an essential phase of developing machine learning models and is performed on the dataset as per the requirement. A feature is defined as a unique attribute or variable in a dataset. Feature engineering helps to improve the performance of machine learning model by selecting the right features for the model and preparing the features in a way that is suitable for the machine learning model. The step used in feature engineering were data cleansing, data transformation, feature extraction, feature selection.

The dataset was randomly divided into 80:20 ratio. The 80% of data was taken for the training the models and the 20 % for the testing the models. Then the models were built by using default Machine Learning Algorithms and then were modified to improve the accuracy of the models. The modification were made by changing the number of descriptors [10] as input data and adjusting the number of decision tree [11] in the models. Then the model was saved and used to predict the unknown data to check the accuracy of the model for unknown

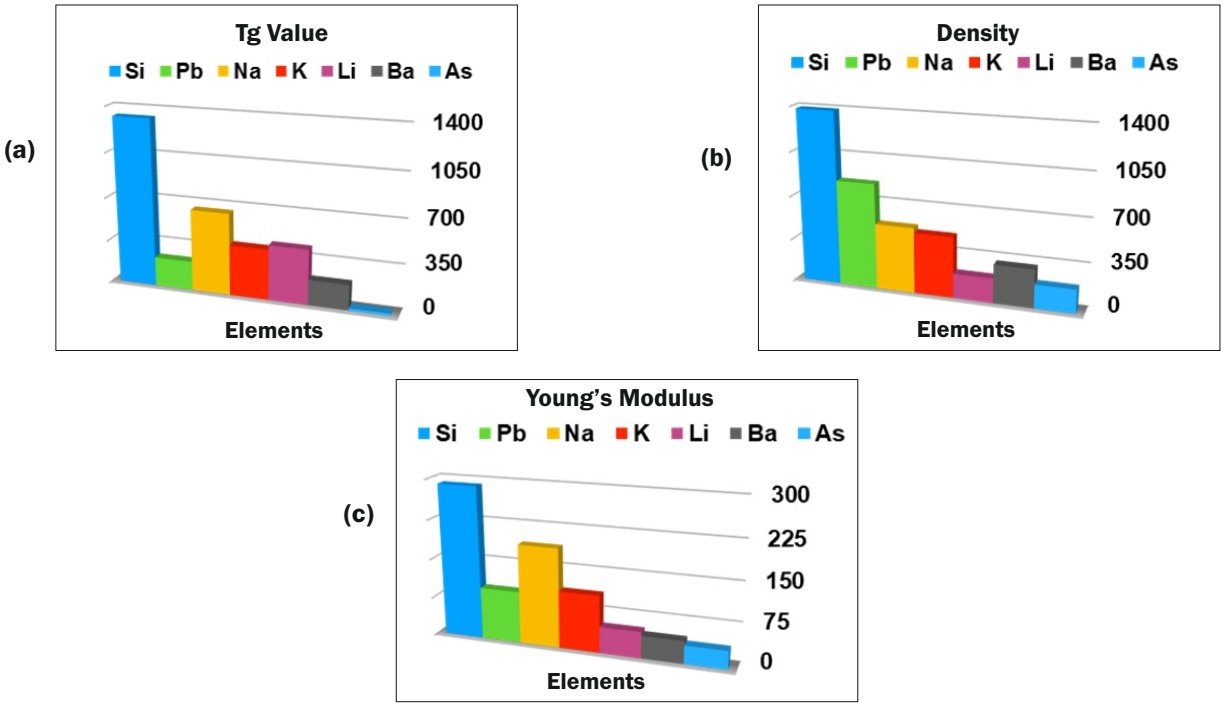


*Fig.1: Number of compositions containing each elements in the clean dataset (a) Density, (b) $T_g$ and (c) Young's Modulus. (Note: Oxygen is present in all glasses of this dataset).*

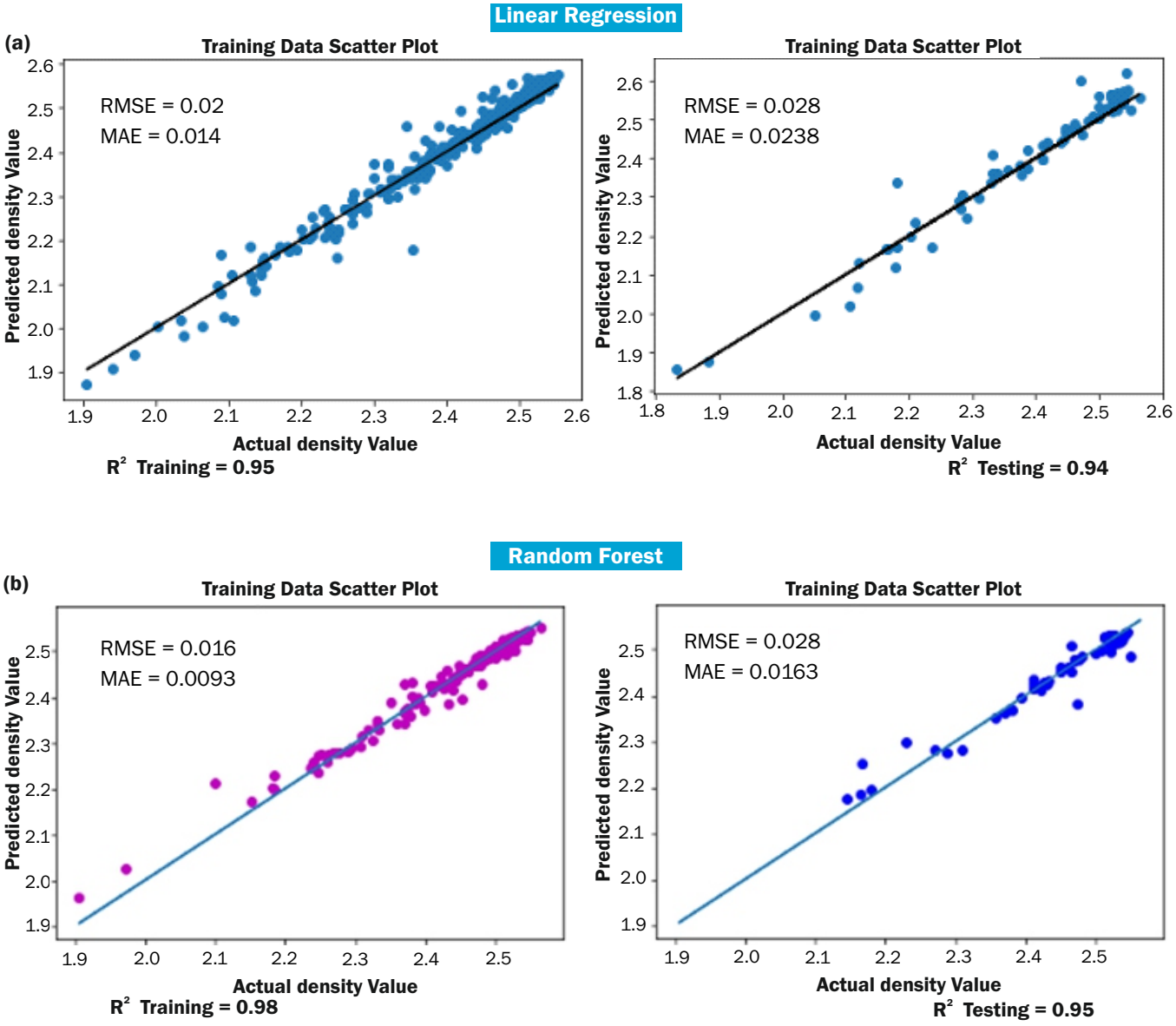


*Fig.2: Scattering plot of actual Density vs. predicted density of training and the testing data. (a) Linear Regression algorithm. (b) Random Forest Algorithm.*

composition. Then we selected the best ML model for each properties that were calculated. All the studies were performed using the Python programming language with the sklearn, numb, pandas, matplot, and pickle libraries available in Anaconda-3.0.

## Results & Discussion

### Sodium Borosilicate Glasses

#### *Density*

The density prediction was done using glass composition as input feature and no additional descriptors were considered. Both Linear regression and the Random Forest model had given accurate results with $R^2$ Training and $R^2$ Testing of 0.95 and 0.94 values for linear Regression and 0.98 and 0.95 for Random Forest model (see Fig.2). The Random Forest method gives better $R^2$ as compared to Linear Regression Model with percentage error of 0.7. Very close values of glass densities from MD simulation and from ML model in Table 1 for unseen glass compositions by ML model (either for training or testing), show the accuracy of RF model for prediction of glass density of sodium borosilicate glasses.

*Table 1: Comparison of density from MD simulation and ML model for sodium borosilicate glasses.*

| Sr. No. | Glass composition | | | MD estimated density (g/cm³) | ML predicted density (g/cm³) |
|---|---|---|---|---|---|
| | $B_2O_3$ | $Na_2O$ | $SiO_2$ | | |
| 1 | 10 | 10 | 80 | 2.39 | 2.39 |
| 2 | 12.5 | 12.5 | 75 | 2.44 | 2.43 |
| 3 | 15 | 15 | 70 | 2.48 | 2.48 |
| 4 | 50 | 10 | 40 | 2.17 | 2.20 |

#### *Glass transition temperature ($T_g$)*

The linear regression model was not suitable for $T_g$ as $R^2$ value was less than 0.8. Therefore, Random Forest model was used for the prediction of the $T_g$ value. The RF model was first tested with single input descriptor i.e. composition and then by using two descriptors - composition and density. The RF model with single descriptor has $R^2$ training and testing equal to 0.98 and 0.96 respectively as displayed in Fig.3. This model was

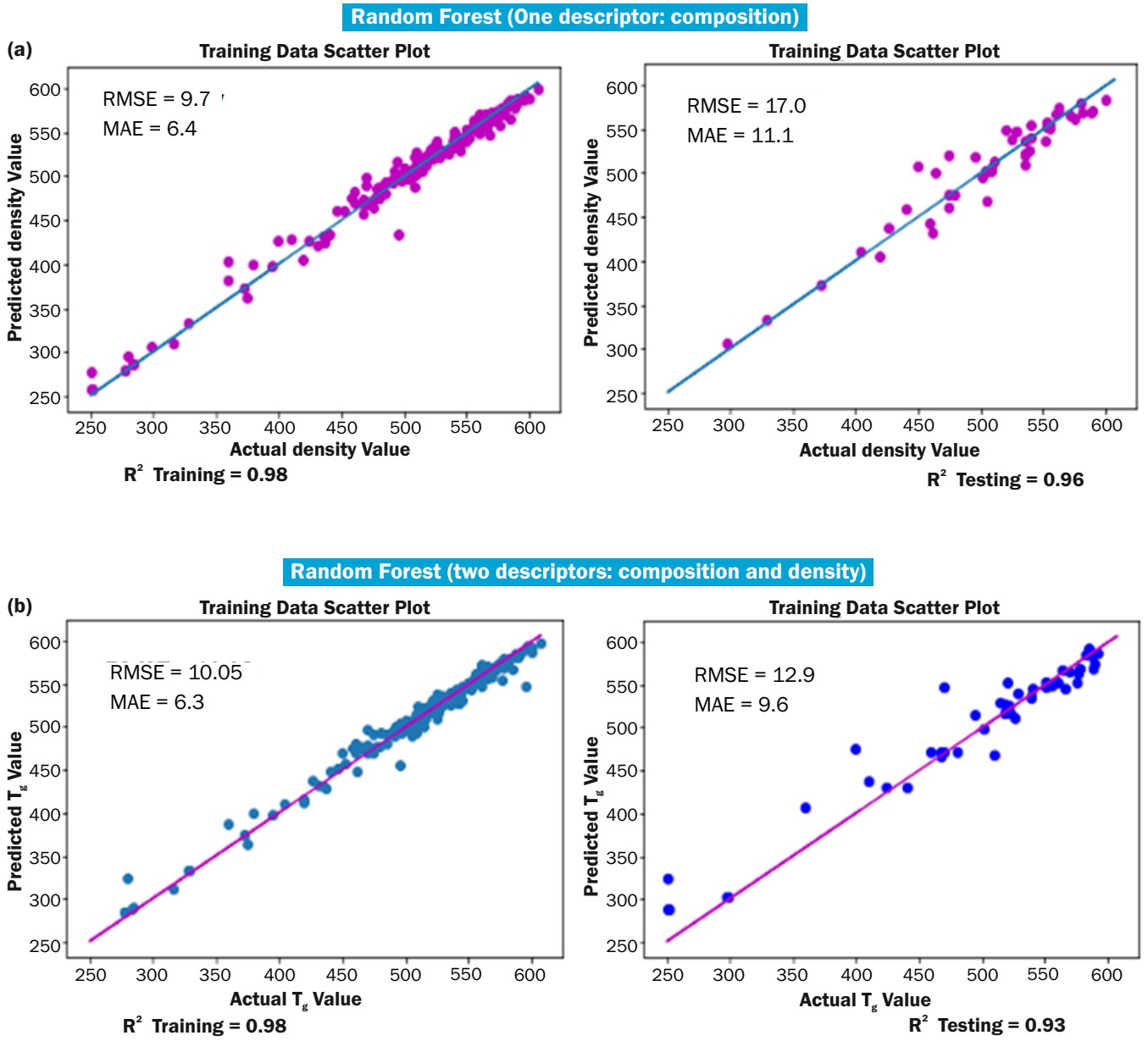


*Fig.3: Plot of actual vs predicted $T_g$ of training and testing using Random Forest Model. (a) Model with only one descriptor (composition), (b) Model with two descriptors (composition and density).*

able to predict the $T_g$ of unknown compositions with error of 20 ± 0.01 K. The second model, with two descriptors has $R^2$ training and testing equal to 0.98 and 0.93 respectively. In spite of lower testing $R^2$, the second model was able to predict the unknown data with lesser error of 15.8 ± 0.01K (data shown in Table 2). Hereby, it can be remarked that the accuracy of model would increase significantly with the addition of the density descriptor as input feature.

### Radiation Shielding Window (RSW) Glass

#### *Density*

The density model for radiation shielding window (RSW) glass build with one descriptor i.e. composition, which gave $R^2$ training and testing of 0.99 and 0.93 respectively as shown in Fig.4. The predicted accuracy was 96% for unknown glass compositions, data reported in Table 3. The RF was seen to optimize at 50 trees as shown in Fig.5. The estimated RMSE and MAE are within acceptable range for density.

*Table 2: Comparison of $T_g$ from MD simulation and ML model for sodium borosilicate glass.*

| Sr. No. | Glass composition | | | MD estimated $T_g$ (°C) | ML predicted $T_g$ (°C) |
|---|---|---|---|---|---|
| | $B_2O_3$ | $Na_2O$ | $SiO_2$ | | |
| 1 | 30 | 14 | 56 | 530 | 541 |
| 2 | 25 | 10 | 65 | 511 | 506 |
| 3 | 20 | 12 | 68 | 570 | 567 |
| 4 | 15 | 15 | 70 | 590 | 586 |

#### Glass transition temperature ($T_g$)

To predict $T_g$, RF model was used with three different number of descriptors. The first one with single descriptor of composition, showed $R^2$ training and testing equal to 0.89 and 0.64 respectively as shown in the Fig.6(a). Further, we added

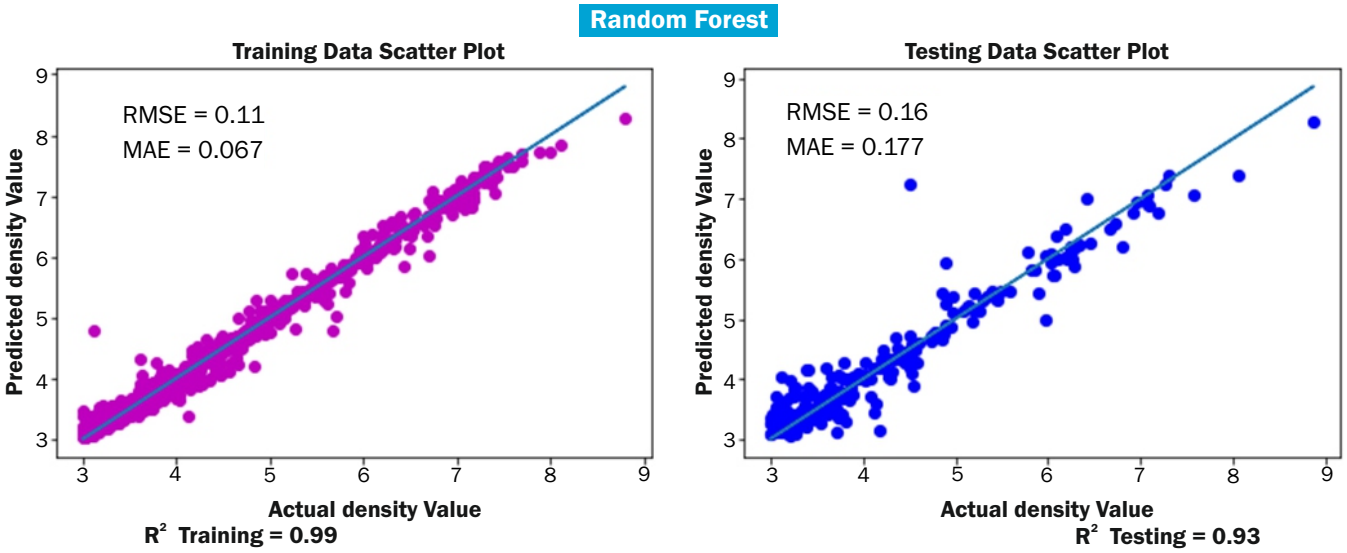


*Fig.4: Scattering plot of actual density value vs predicted density value of training and the testing using Random Forest Model. Note – RMSE (Root Mean Square Error) and MAE (Mean Absolute Error).*

*Table 3: Comparison of density from MD simulation and ML model for RSW glass.*

| Sr. No. | Glass composition | | | | MD estimated density (g/cm³) | ML predicted density (g/cm³) |
|---|---|---|---|---|---|---|
| | $SiO_2$ | $K_2O$ | $Na_2O$ | PbO | | |
| 1 | 84 | 16 | 0 | 0 | 3.32 | 3.32 |
| 2 | 67 | 0 | 33 | 0 | 3.07 | 3.10 |
| 3 | 51 | 0 | 0 | 49 | 5.91 | 5.88 |
| 4 | 64.8 | 1.8 | 0 | 33.4 | 4.60 | 4.50 |

*Comparison of density from MD simulation and ML model [using RF method with composition as descriptor] for RSW glass.*

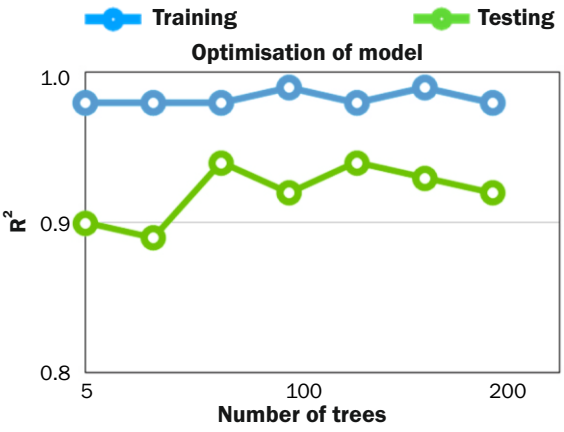


*Fig.5: The accuracy (as captured by the $R^2$ value) of the Random Forest model as a function of number of trees considered in each model as obtained for the training and testing set respectively.*

atomic mass descriptor to composition and found that the $R^2$ training and testing was decreased to 0.88 and 0.61 respectively (see Fig.6(b)). $R^2$ testing was furthermore reduced to 0.42 (with $R^2$ training as 0.92), while including 3rd descriptor of atomic size as shown in the Fig.6(c). Nevertheless, the prediction of $T_g$ for unknown dataset made using RF model with three descriptors showed sufficient close to the MD estimated $T_g$. (see Table 4). Notably, the estimated RMSE and MAE values are higher in case of RSW glass compared to NBS-Glass due to higher data range [5]. It might be noteworthy to mention that the sole-observation of the mean error values (RMSE, MAE) and $R^2$ values can't give enough evidence for the statistical accuracy of model for prediction than its competitors with higher values of mean error bar and $R^2$. Similar to studies of Alobaca et al. [5], we found that in spite of higher mean error and low $R^2$ testing, our model predicts good match of $T_g$ with MD estimated data as shown in Table 4. The $R^2$ training and testing as a function of number of trees (for 3rd model) is shown in Fig.7, where model seem to be optimized with 5 trees for training and 150 trees for testing.

### *Young's Modulus*

Similar to previous case of $T_g$, three RF models with different descriptors; (i) composition, (ii) composition and atomic mass, and (iii) composition, atomic mass and atomic size; were used for prediction of Young's modulus. The overlapping of predicted data with actual data and the $R^2$ training and testing for last two models (with two and three descriptors) is shown in Fig.8. The RF Model with three descriptors was found to have highest accuracy with $R^2$ training and testing equal to 0.88 and 0.89 respectively. This model was optimized with 150 number of RF tress (data shown in Fig.9. The accuracy of 3rd model can be noted from nearly similar values of ML predicted and MD estimated Young's modulus values in Table 5 for unknown data which was not used either for training or testing.

## Conclusion

In this work, we carried out large number of experiments evaluating two popular ML algorithms: Linear Regression and Random Forest to analyze data sets of sodium borosilicate glasses and window shielding glasses and their respective density, glass transition temperature $T_g$ and Young's Modulus. We investigated the performance of these algorithm when used for the prediction with default and featured engineered models. We also investigated the effect of descriptors on the different property prediction and the $R^2$ value of the models. The impact of descriptor on the different properties of glass was noted to be different. The density had direct relation with composition and addition of any other descriptor doesn't have

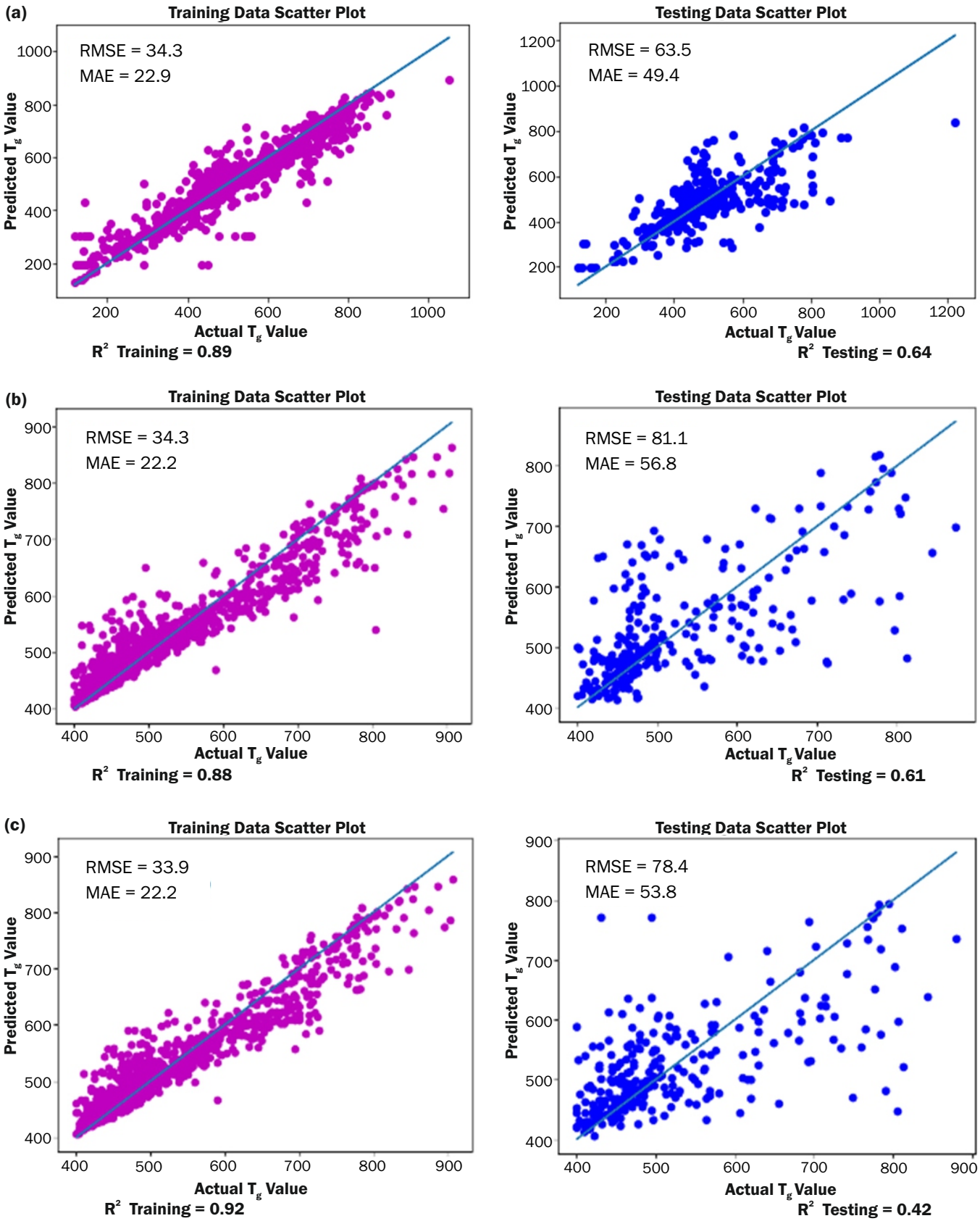


*Fig.6: Scattering plot of actual $T_g$ value vs predicted $T_g$ value of training and the testing using Random Forest Model. (a) Model with one descriptor (composition), (b) Model with two descriptors (composition and Atomic Mass), (c) Model with three descriptors (composition, Atomic Mass and Atomic size).*

any significant effect on the model accuracy. On the other hand, Young's modulus not only depends on the composition but also greatly depends on other descriptors like atomic mass and atomic size. While $T_g$ mostly depends on the compositions and density. Importantly, with the prediction accuracy of these models for unknown data, it was shown that the sole-observation of the mean error values (RMSE, MAE) and $R^2$ values can't give enough evidence for the statistical accuracy of model than its competitors with higher values of mean error bar and $R^2$.

*Table 4: Comparison of $T_g$ from MD simulation and ML model for RSW glass.*

| Sr. No. | Glass composition | | | | | | $T_g$ (°C) [MD] | $T_g$ (°C) [ML] |
|---|---|---|---|---|---|---|---|---|
| | $SiO_2$ | $K_2O$ | $Na_2O$ | PbO | $Li_2O$ | $As_2O_3$ | | |
| 1 | 66.7 | 16.6 | 16.7 | 0 | 0 | 0 | 431.2 | 420 |
| 2 | 75.8 | 6.8 | 7.6 | 9.8 | 0 | 0 | 422.4 | 413 |
| 3 | 90 | 0 | 5 | 0 | 5 | 0 | 452.0 | 467 |
| 4 | 77.3 | 2.8 | 4 | 14.4 | 1.4 | 0.04 | 444.4 | 445 |

*Comparison of Tg from MD simulation and ML model[using RF method with three descriptors: composition, atomic mass and atomic size] for RSW glass.*

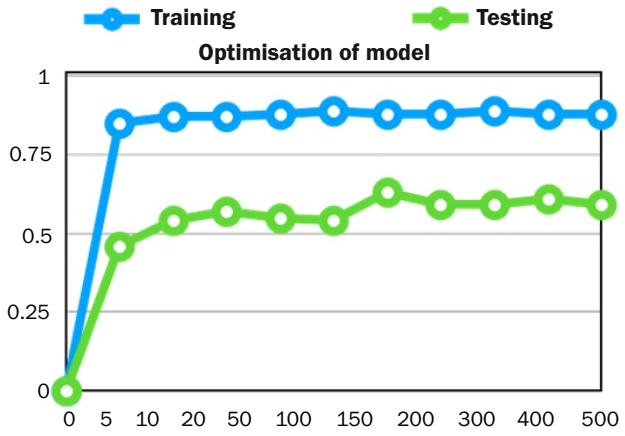


*Fig.7: The accuracy (as captured by the $R^2$ value) of the Random Forest model as a function of number of trees considered in each model as obtained for the training and testing set respectively.*

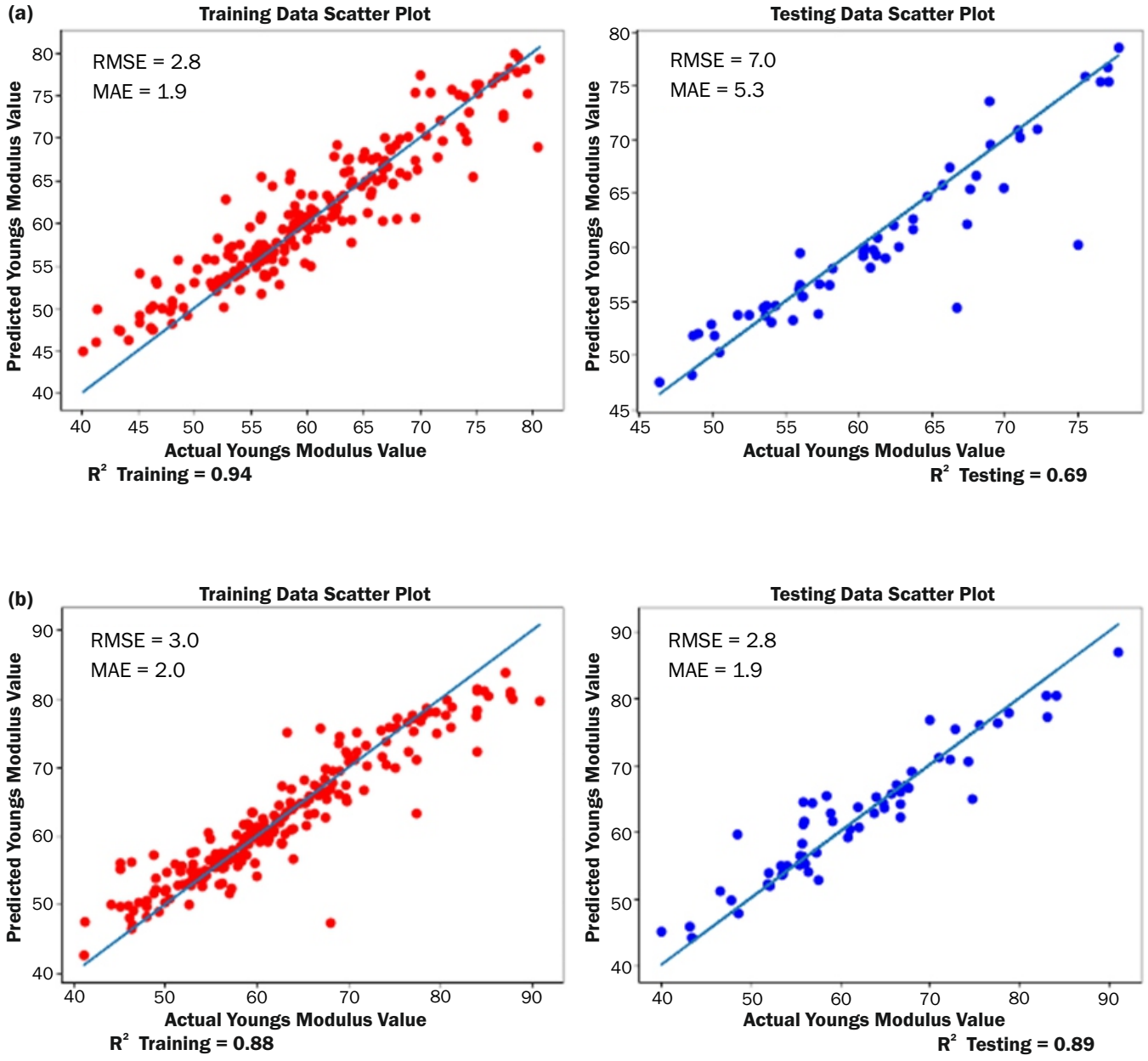


*Fig.8: Scattering of actual Young's Modulus vs predicted Young's Modulus of training and the testing using Random Forest Model. (a) Model with two descriptors (composition and atomic mass), (b) Model with three descriptors (composition, atomic mass and atomic size).*

*Table 5: Predicted Young's modulus and actual Young's modulus from 3rd RF model.*

| Sr. No. | Glass composition | | | | | | | Y [GPa] [MD] | Y [GPa] [ML] |
|---|---|---|---|---|---|---|---|---|---|
| | $SiO_2$ | $K_2O$ | $Na_2O$ | PbO | $Li_2O$ | BaO | $As_2O_3$ | | |
| 1 | 66.7 | 14.5 | 0 | 19 | 0 | 0 | 0.24 | 50.50 | 50.28 |
| 2 | 77.3 | 7.6 | 5.8 | 0 | 0 | 9.3 | 0 | 71.00 | 71.15 |
| 3 | 75 | 5 | 10 | 0 | 0 | 10 | 0 | 64.92 | 64.36 |
| 4 | 52 | 8 | 20 | 0 | 20 | 0 | 0 | 55.90 | 55.99 |

The presented study can be easily expanded to predict other properties such as thermal expansion coefficient, elastic modulus, and hardness to successfully replace empirical approves for developing novel glasses with useful properties and applications. The Machine Learning can also be used to construct an algorithm which would be able to predict more than one property at once.


## Acknowledgement

Authors sincerely acknowledge Director, Chemical Engineering Group, BARC and Head, Chemical Engineering Division, BARC for their and support and encouragement.


## References


[1] Zanotto, E. D.; Mauro, J. C. The Glassy State of Matter: Its Definition and Ultimate Fate. Journal of Non-Crystalline Solids2017, 471, 490–495. https://doi.org/10.1016/j.jnoncrysol.2017.05.019.

[2] Zanotto, E. D.; Coutinho, F. A. B. How Many Non-Crystalline Solids Can Be Made from All the Elements of the Periodic Table? Journal of Non-Crystalline Solids2004, 347 (1), 285–288. https://doi.org/10.1016/j.jnoncrysol.2004.07.081.

[3] Liu, H.; Fu, Z.; Yang, K.; Xu, X.; Bauchy, M. Machine Learning for Glass Science and Engineering: A Review. Journal of Non-Crystalline Solids: X2019, 4, 100036. https://doi.org/10.1016/j.nocx.2019.100036.

[4] Cassar, D. R.; de Carvalho, A. C. P. L. F.; Zanotto, E. D. Predicting Glass Transition Temperatures Using Neural Networks. Acta Materialia2018, 159, 249–256. https://doi.org/10.1016/j.actamat.2018.08.022.

[5] Alcobaça, E.; Mastelini, S. M.; Botari, T.; Pimentel, B. A.; Cassar, D. R.; de Carvalho, A. C. P. de L. F.; Zanotto, E. D. Explainable Machine Learning Algorithms For Predicting Glass Transition Temperatures. Acta Materialia2020, 188, 92–100. https://doi.org/10.1016/j.actamat.2020.01.047.


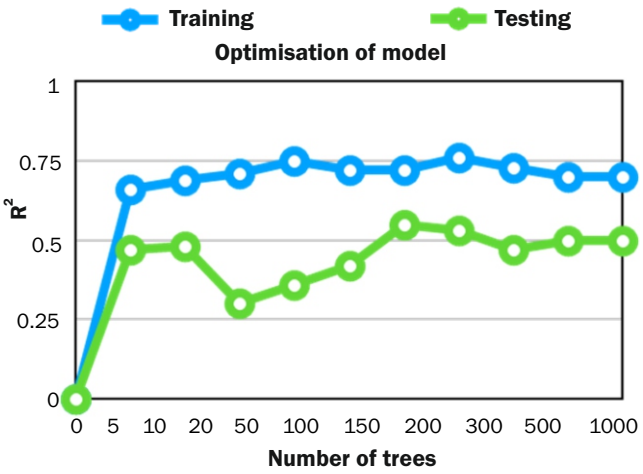


*Fig.9: The accuracy (as captured by the $R^2$ value) of the Random Forest model as a function of number of trees considered in each model as obtained for the training and testing set respectively.*


[6] Yang, K.; Xu, X.; Yang, B.; Cook, B.; Ramos, H.; Krishnan, N. M. A.; Smedskjaer, M. M.; Hoover, C.; Bauchy, M. Predicting the Young's Modulus of Silicate Glasses Using High-Throughput Molecular Dynamics Simulations and Machine Learning. Sci Rep 2019, 9 (1), 8739. https://doi.org/10.1038/s41598-019-45344-3.

[7] Breiman, L.; Friedman, J. H. Predicting Multivariate Responses in Multiple Linear Regression. Journal of the Royal Statistical Society: Series B (Methodological)1997, 59 (1), 3–54. https://doi.org/10.1111/1467-9868.00054.

[8] Breiman, L. Random Forests. Machine Learning2001, 45 (1), 5–32. https://doi.org/10.1023/A:1010933404324.

[9] Feature Engineering for Machine Learning [Book]. https://www.oreilly.com/library/view/feature-engineering-for/9781491953235/ (accessed 2023-06-07).

[10] Jain, A.; Bligaard, T. Atomic-Position Independent Descriptor for Machine Learning of Material Properties. Phys. Rev. B2018, 98 (21), 214112. https://doi.org/10.1103/PhysRevB.98.214112.

[11] Liu, H.; Zhang, T.; Anoop Krishnan, N. M.; Smedskjaer, M. M.; Ryan, J. V.; Gin, S.; Bauchy, M. Predicting the Dissolution Kinetics of Silicate Glasses by Topology-Informed Machine Learning. npj Mater Degrad2019, 3 (1), 1–12. https://doi.org/10.1038/s41529-019-0094-1.

# Optical Processing

5

# Micro-lens Array Assisted Nano-Patterning on Stainless Steel using Picosecond Laser

**Sunita Kedia*[1,4], Pratiksha Pawar[2], Kiran Yadav[2], A. K. Sahu[3] and J. Padma Nilaya[1,4]**

[1]*Laser & Plasma Technology Division, Bhabha Atomic Research Centre, Trombay – 400085, INDIA*
[2]*Department of Physics, K. J. Somaiya, Vidyavihar, Mumbai – 400077, INDIA*
[3]*Glass & Advanced Material Division, Bhabha Atomic Research Centre, Trombay – 400085, INDIA*
[4]*Homi Bhabha National Institute, Training School Complex, Anushaktinagar, Mumbai – 400094, INDIA*

*Various patterns generated on SS sample*

ABSTRACT

Optical near-field processing by employing contact particle lens array leading to effective nano-patterning on metal surface using a picosecond pulsed laser has been demonstrated. The technique utilizes self-assembled monolayer of polystyrene colloidal microspheres as near-field optical confinement structure on 316L stainless steel (SS). Each microsphere, acting as a micro-lens, focuses the incident laser beam leading to material ablation and pit formation underneath. The characteristics of pitting depend sensitively on the laser parameters, particle and substrate material properties. These nano features may have diverse applications including inscribing security features.

KEYWORDS: *Micro-lens, Nano-patterning, Picosecond laser, Monolayer, Colloidal particles*

## Introduction

Nano-patterning on surfaces have wide ranging applications in diverse areas, e.g., biosensors, display, data storage, solar cells, security etc. [1-5]. Designing unique nanoscale patterns on metal surfaces with limits on its replication can provide a high level of security against fraudulent activities [6]. Generation of nano-patterns on metals and semiconductors usually employ costly, multi-step and time-consuming lithography processes which limit production throughputs [7,8]. In last decade or so, particle lens array has evolved as one of the near field techniques for laser-based surface nano-patterning on substrates [8] and has gained popularity as a contactless process with ability to generate surface features smaller than the diffraction limit. In this process, a hexagonally close packed monolayer of spherical colloidal particles is deposited on a smooth surface by self-assembly method. When exposed to a laser pulse of appropriate fluence, each particle acts as a micro-lens and focuses the incident laser beam at particle-substrate contact point where the beam intensity enhances to a level as to cause ablation of substrate material resulting in the formation of nano-pits [9,10]. Depending upon the laser spot size, wavelength, intensity and the substrate and particulate materials, nano-patterns can be generated on polymer surfaces [11], hydrophobic surface [8], semiconductor substrates [12] etc. In the absence of any particulate absorption, it is understandable that higher is the laser intensity, larger would be pit dimensions. Needless to say, the substrate properties, e.g, its absorption at the incident wavelength, melting point etc. also play an important role in this process.

We present here, our experimental results of nano-patterning on 316L stainless steel alloy (SS) surface by means of polystyrene (PS) colloidal particle (dia ~2.3 μm) monolayer irradiated by a single pulse from a picosecond laser operating at 532nm. A focused laser beam with a sub-mm spot size was allowed to shine upon the mono layer of particles. Coupled with computer controlled linear translation stage, patterns well discernable by eye were generated on the substrate surface with each point in the pattern holding a sub-pattern of nano-pits. The size, depth, and density of the nano-pits could be sensitively regulated by controlling the laser power, laser wavelength and diameter of colloidal particles respectively. If characterized thoroughly, this technique can be gainfully employed as a security feature that can be inscribed on any surface which may be a part of an important instrument that requires protection from replication. Apart from standardizing methods to generate monolayer of particles on substrates over large areas, nano-pits of diameter ranging from ~0.5 μm to 1.5 μm on SS substrates by varying laser energy from 0.3 mJ to 2.5 mJ respectively, have been generated as sub-structures of main patterns on SS substrate. The pattern 'BARC' on SS sample with and without monolayer was compared where the single direct laser pulse irradiation yields a single spot of size ~100 μm whereas, monolayer assisted irradiation leads to the creation of ~ 2000 nano-pits within the same area.

## Materials and Methods

A novel method for the generation of monolayer on SS substrate was conceived and Fig.1(a) shows the sequence of steps followed. Commercially procured aqueous colloidal solution of monodispersed PS microsphere (M/s. Spherotech Inc.) of diameter ~2.3 μm and 5% w/v concentration was appropriately diluted in ethanol and subsequently ultrasonicated for 20 min. The colloidal mixture was drop-cast on water surface in a Petridish where the PS particles floated on the surface of the liquid (density of PS (0.0005 g /cm$^3$) was less than methanol (0.79 g /cm$^3$) and water (1 g /cm$^3$)). The dilution was optimized such that the particles formed monolayer on water surface. Mirror polished SS substrates (diameter: 2 cm) with average roughness of ~1.5 nm were cleaned with methanol. Monolayer of PS settled on water

*Author for Correspondence: Sunita Kedia
E-mail: skedia@barc.gov.in

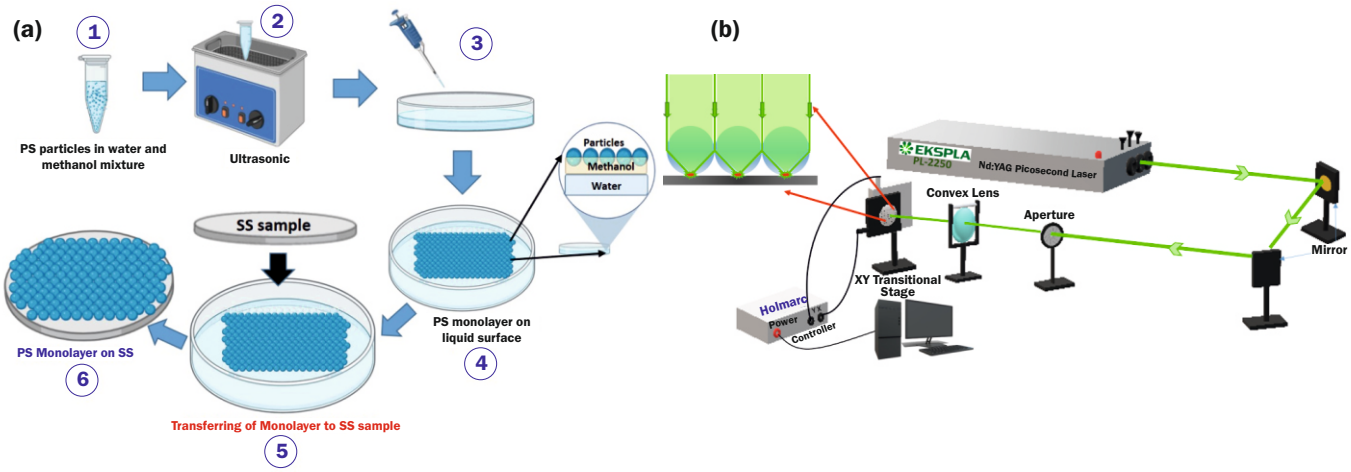


*Fig.1: (a) Pictorial depiction of PS monolayer preparation on SS substrate (b) Experimental set up for laser assisted pitting, inset: simple rendition of focusing of the incident laser beam through micro particles.*

surface was carefully transferred to the SS and was allowed to dry in ambient with adequate protection from dust. Deposition of PS monolayer was confirmed using scanning electron microscope (SEM) images. An Nd:YAG picosecond pulsed laser (M/s. Ekspla; PL2250) with pulse duration ~30 ps emitting at 532 nm was used to irradiate the PS monolayer. The substrate surface was exposed to a single laser pulse that was steered and focused (10 cm focal length lens) on to the sample. The laser beam affected spot diameter was ~100 µm and contained ~2000 microparticles. Under ideal conditions of irradiation, each PS particle can give rise to a pit (inset of Fig.2(b)) and therefore, a sub-pattern of ~2000 nano-pits can be generated in one laser spot.

The analytic expression for microsphere induced pitting for sphere radius r >> λ is given by N. Arnold as follows [13].

$$w = r\sqrt{\frac{(4-n^2)^3}{27n^4}} \qquad (1)$$

where *n* is the refractive index of the sphere and λ is wavelength of incident light. As per equation-1, the laser spot size on the substrate will increase with particle size.

To be noted that, depending upon the spatial variation of laser intensity as a result of focusing, characteristics of pits generated under one laser shot may not be identical. However, this can be avoided by managing uniform intensity of the incident beam. Distance between two laser shots was maintained as 350 µm and various patterns were generated on the sample using computer controlled X-Y stage. The residues of the PS particles were removed post laser irradiation by immersing the sample in toluene for ~5 min. For sake of comparison, pattern of 'BARC' was generated on SS sample with and without monolayer, keeping all other parameters constant and the difference between then in the micro-nano scale is evaluated.

## Results and Discussion

Fig. 2(a) shows the SEM images of PS monolayer on SS sample where hexagonally closed packed monolayer of PS particles can be seen in the inset of the figure. Fig.2(b) is a photograph of the sample where monolayer covering large surface area (~3 $cm^2$) of SS can be seen, the variation in surface color is an artifact due to reflection off the PS particulates. Fig.2(c) and its inset are the SEM image of the sample surface irradiated by single laser pulse (30ps, 1mJ) and subsequently cleaned in toluene showing nano-pits in closed packed arrangement on the substrate surface. Fig.2(d)

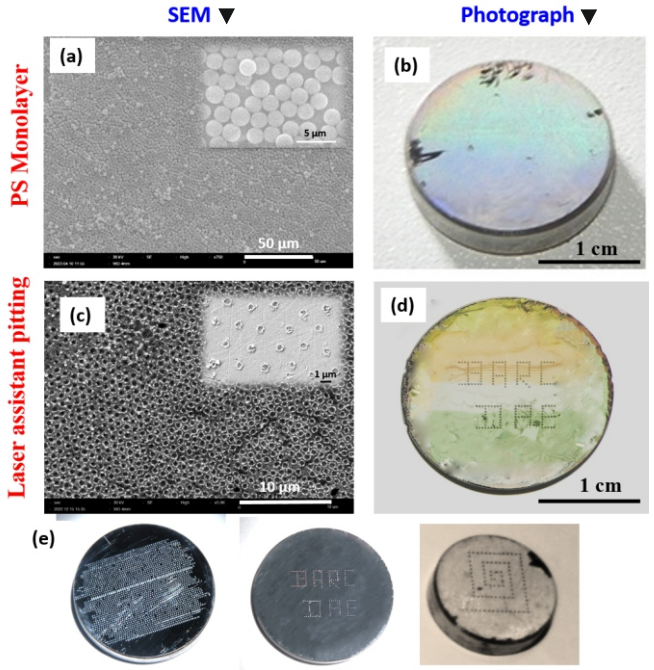


*Fig.2: (a) SEM image and (b) photograph, of PS monolayer on SS sample. (c) SEM image and (d) photograph, of laser assisted pitting on SS sample and (e) various pattern generated on SS sample.*

shows the photograph of a sample, with residual particulates post irradiation, on which 'BARC-DAE' has been inscribed. Some other patterns were tried with the same experimental set-up, photographs of which after removing the monolayer in toluene are shown in Fig.2(e).

Fig.3(a) and 3(b) are photograph of SS samples on which 'BARC' pattern has been created without and with PS monolayer, respectively. While both images appear similar to the eye, they are significantly different in micro-nano scale. A single beam of focused laser pulse on a substrate surface devoid of particulates results in a laser affected region (extending over ~100 µm) comprising of melted and resolidified portion at the centre surrounded by heat affected zone that depends on the spatial profile of the focused laser beam. Further magnification of this region shows undulations of the surface, a signature of the process mentioned above. The dark spots visible on the surface of sample (marked with arrows) are inherent defects on SS. However, in case of particle deposited surface, the focusing effect causes ablation and

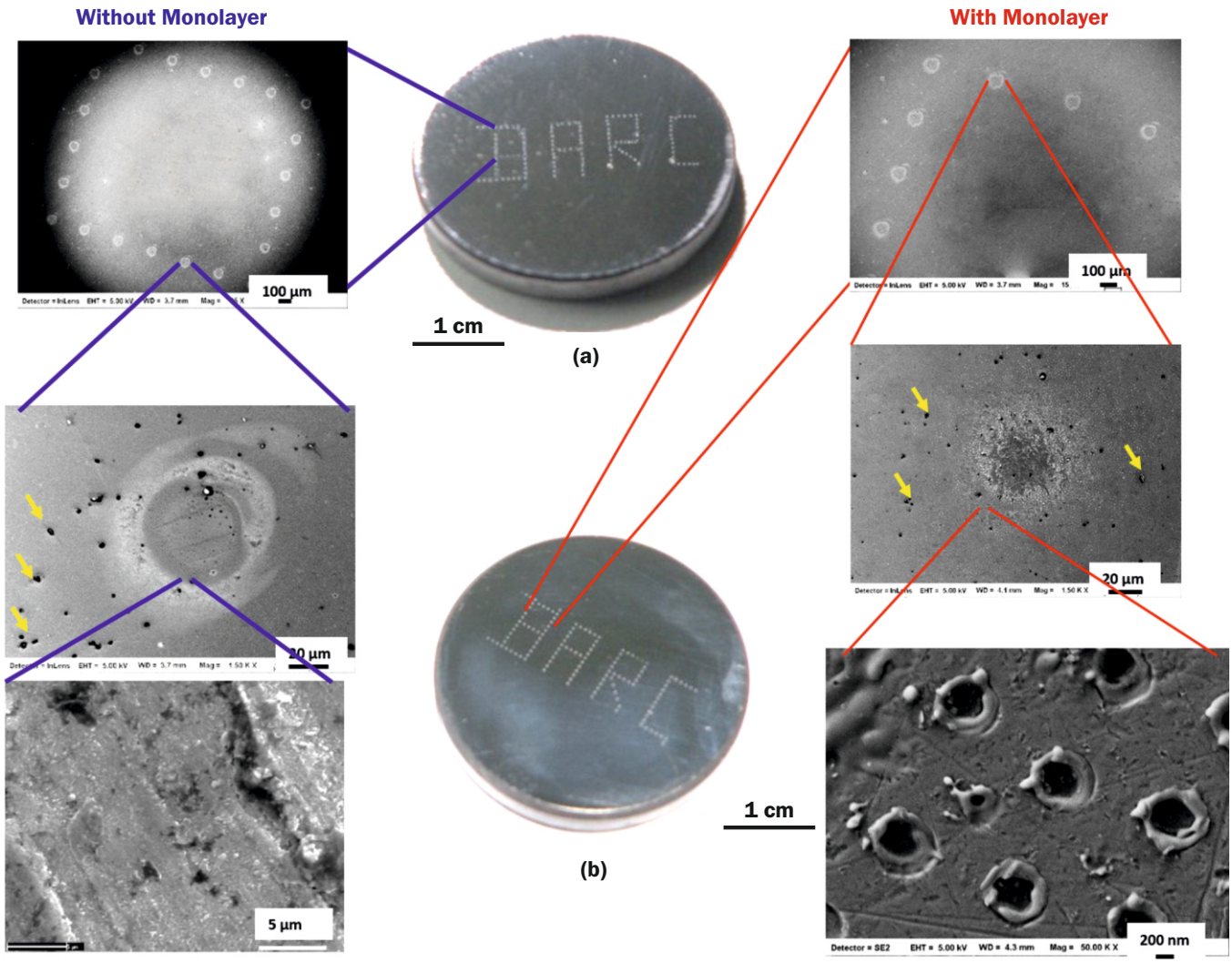


*Fig.3: Photograph, SEM image at different magnification of pattern generated on SS sample (a) without PS monolayer and (b) with PS monolayer.*

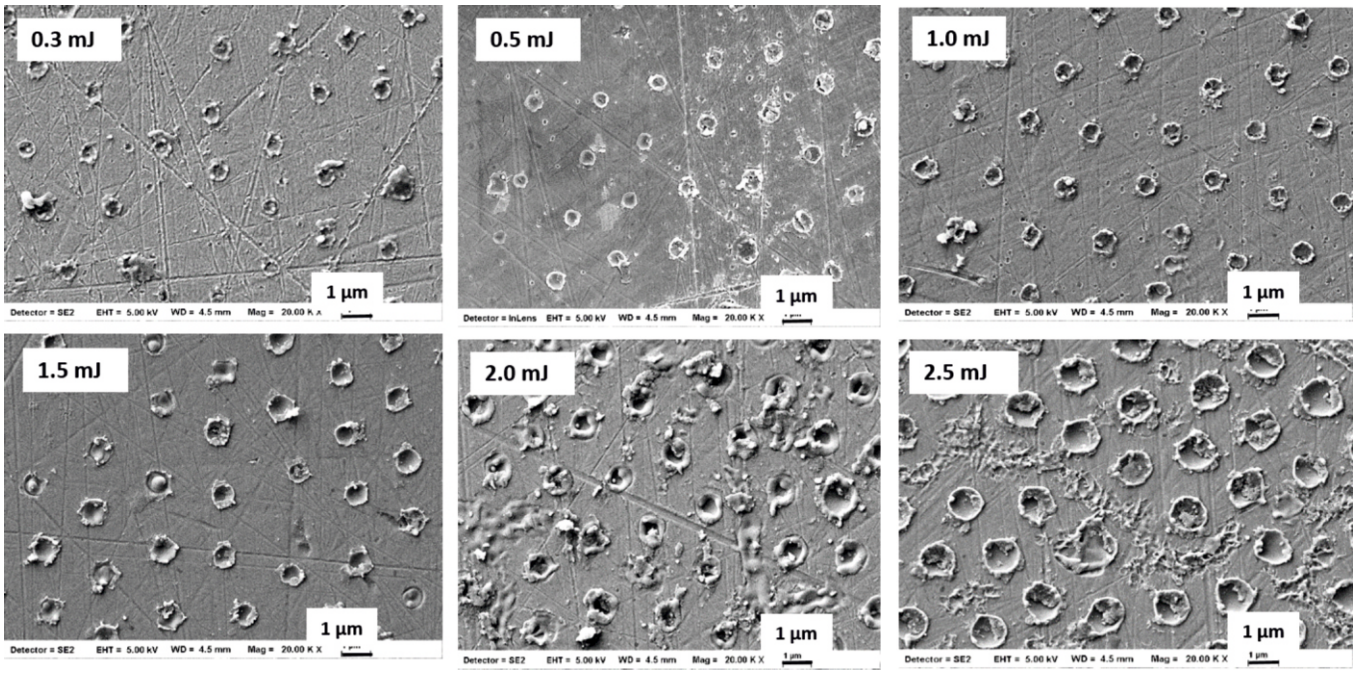


*Fig.4: FE-SEM images of the pits generated on SS sample at different incident laser energy.*

formation of pits and the same laser affected region has ~2000 nano-pits of diameter ~500 nm in it, as can be seen in the magnified (50 KX, scale bar- 200 nm) SEM image of Fig.3(b). Dimension, depth and separation between these nano-pits can be controlled and manipulated by varying laser power, pulse duration, wavelength, and diameter of micro-particles. As an example, Fig.4 shows the change in pit dimension with variation in laser energy.

The SEM images of pits generated at various laser energy per pulse on SS surface using PS monolayer of particle size ~2.3 µm. An increase in pit diameter from 0.5 µm (at 0.3 mJ) to 1.5 µm (at 2.5 mJ) is clearly visible in the images. This is due to an increase in the laser intensity at the contact point of particle and surface with increased laser power that in turn increases the area where ablation occurs.

Further investigations for a thorough parametric characterisation of this technique such as, depth profile vis-à-vis laser parameters, effect of microsphere diameter, surface oxidation, effect on mechanical properties of the surface, reproducibility, use of different materials such as polymers, and scaling-up are being planned.

## Conclusions

In conclusion, we have demonstrated a simple method of surface nano-patterning by particle assisted pulsed laser irradiation that can be scaled up easily. The characteristics of the nano-pits can be altered in a controllable manner by changing the laser parameters and the dimension of the particles. The technique of contact particle lens array assisted surface patterning appears promising, apart from other applications, in inscribing nano-security features on surfaces.

## Acknowledgements

The authors gratefully acknowledge constant support and guidance of Head, Laser & Plasma Technology Division and of Group Director, Beam Technology Development Group. They also acknowledge Nayna Jadhav, IRLS, BARC for technical help.

## References

[1] V. Naresh and N. Lee, A review on biosensor and recent development of nanostructured materials enabled biosensors, Sensor 21 (2021) 1190.

[2] Z. Chai, A. Childress and A. A. Busnaina, Direct assembly of nanomaterials for making nanoscale devices and structure: Mechanisms and applications, ACS Nano 16 (2022) 17641.

[3] J. Yu, M. Luo, Z. Lv. S. Huang, H. H. Hsu, C. C. Kuo, S. T. Han and Y. Zhou, Recent advantages in optics and optoelectronic data storage based on luminescent nanomaterials, Nanoscale 12 (2020) 23391.

[4] S. M. Lee, R. Biswas, W. Li, D. Kang, L. Chan, and J. Yoon, Printable nanostructured silicon solar cells for high-performance, large-area flexible photovoltaics, ACS Nano 8 (2014) 10507.

[5] J. Rajendran, R. Karri, J. B. Wendt, M. Potkonjak, N. McDonald, G. S. Rose, and B. Wysocki, Nano meets security: exploring nanoelectronics devices for security applications, Proceedings of the IEEE, 103 (2015) 829.

[6] J. Kim, J. M. Yun, J. Jung, H. Song, J. B. Kim and H. Lhee, Anti-counterfeit nanoscale fingerprints based on randomly distributed nanowires, Nanotechnology 25 (2014) 155303.

[7] Y. Xia and G. M. Whitesides, Soft Lithography, 28 (1998) 153

[8] A. Khan, Z. Wang, M. A. Sheikh, D. J. Whitehead and L. Li, Laser micro/nano patterning of hydrophobic surface by contact particle lens array, Applied Surface Science 258 (2011) 774.

[9] B. Sugathan, J. P. Nilaya, V. P. M. Pillai, and D. J. Biswas, Particle assisted structuring on metallic substrate: Anomaly when particle size exceeds irradiation wavelength, AIP Advanced 10 (2020) 035222.

[10] X. Sedao, T. Jy. Derrien, G. W. Romer and B. Pathiraj, Laser surface micro-/nano-structuring by a simple transportable micro-sphere lens array, Journal of Applied Physics 112 (2012) 103111.

[11] C. Farcau and S. Astilean, Simple colloidal lithography approach to generate inexpensive stamps for polymer nano-patterning, Materials Letters 65 (2011) 2190.

[12] B. Sugathan, J. P. Nilaya, V. P. M. Pillai and D. J. Biswas, Observation of particle assisted nano-ring, bump, pit structures on semiconductor substrate by dry laser exposure, AIP Advanced, 8 (2018) 115110.

[13] N. Arnold, Theoretical description of dry laser cleaning, Appl. Surf. Sci. 208 (2003) 15.

# Nuclear Medicine in Healthcare

6

# Clinical PET/CT, Nuclear Cardiology and Radionuclide Therapy: Current Status & New Developments

**Priyanka Verma[1,2], Ramesh Asopa[1,2] and Sandip Basu*[1,2]**

[1]*Radiation Medicine Centre, Bhabha Atomic Research Centre, Tata Memorial Centre Annexe, Parel, Mumbai – 400012, INDIA*
[2]*Homi Bhabha National Institute, Anushaktinagar, Mumbai – 400094, INDIA*

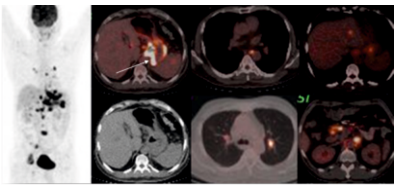

*PET-CT MIP and fused axial images*

ABSTRACT

This review discusses the current practices and newer developments in 3 important domains of Nuclear Medicine: (a) Clinical PET/CT, (b) Nuclear Cardiology & (c) Radionuclide Therapy. Their applications in cancer and non-oncological diseases through each of these modalities have been enumerated and discussed, citing specific clinical illustrations in each given scenario, with enlistment of various radiotracers and their specific uses.

KEYWORDS: *Nuclear medicine, PET/CT, Radionuclide Therapy, Oncology, Cardiology, Radiopharmaceuticals*

## Introduction

Molecular imaging involves in vivo characterization of biologic processes and their measurement at the cellular and molecular level. This enables early discovery of changes in tissues since functional alteration in tissues often precedes changes in anatomy. In Nuclear Medicine, radiolabelled molecules called radiopharmaceuticals are used for diagnosis and treatment of disease. Rapid developments in diagnostic methods and analysis have led to a paradigm change in disease management, with the process of diagnosis and treatment shifting from standard to personalized treatment[1].

## Developments

One major development in the molecular imaging is the Positron Emission Tomography/Computed Tomography (PET/CT). Positron emission tomography (PET) is increasingly being used for the diagnosis, staging, restaging and follow-up of various cancers and also for various benign applications. It has an important role in the evaluation of various tumors including solitary pulmonary nodules, non–small cell lung carcinoma, lymphoma, melanoma, breast cancer, and colorectal cancer [2]. PET is based on the detection of annihilation photons (γ) released when positron emitting radionuclides, such as F-18, Ga-68, C-11, and O-15, emit positrons ($\beta^+$) that undergo annihilation with electrons. The photons thus released have energies of 511 keV (0.511 MeV) and are detected by the detector in the PET scanner. FDG is currently the most widely used PET radiopharmaceutical in clinical oncology in addition to its clinical applications in cardiology and neurology [3].

PET with FDG allows direct evaluation of the cellular glucose metabolism. Glucose has been shown to be a major source of energy for the cancer cells. Tumor cells are usually fast growing in comparison to normal cells, and thus require additional energy to sustain their rapid growth rate. Whole-body FDG-PET/CT imaging is used to detect the spread of disease before they are noted by other imaging modalities, thus, improving staging and patient treatment, monitoring drug therapy and differentiating between active tumor and necrotic scar tissue which may be indistinguishable by other imaging modalities. When treating patients with chemotherapeutic agents or radiation therapy, standard anatomic imaging using CT or MR imaging may not be able to show the efficacy of therapy through structural changes early in the course. By using $^{18}$F-FDG-PET to monitor the bio-chemical changes in the tumor site, the effectiveness of therapy can be determined early [4].

Various PET radiotracers have been used clinically, and can be classified based on their mechanism of localization:

### *Metabolism*

- Glucose metabolism: $^{18}$F-fluorodeoxyglucose (FDG), cyclotron produced, half-life 110 minutes (most commonly used)
- Bone metabolism: $^{18}$F-fluoride
- Membrane lipid synthesis: $^{11}$C-acetate, $^{18}$F-choline.
- Amino acid transport & metabolism: $^{11}$C-methionine, $^{18}$F-tyrosine.

### *Perfusion*

- $^{15}$O-water (cyclotron produced, $T_{1/2}$ = 2 min)
- $^{13}$N-ammonia (cyclotron produced, $T_{1/2}$ = 10 min)
- $^{82}$Rubidium chloride (generator produced, $T_{1/2}$ = 78 sec)

### *DNA Synthesis*

- $^{18}$F-fluorothymidine (FLT), $^{11}$C-Thymidine

### *Receptor Expression*

- Somatostatin receptors: $^{68}$Ga-DOTA-TATE/TOC/NOC (Neuroendocrine tumors)

**Author for Correspondence: Sandip Basu*
*E-mail: drsandipb@gmail.com*

- Estrogen receptors: $^{18}$F-fluoroestradiol(Breast cancer)
- Dopamine receptors: $^{18}$F-fluoroDOPA (Neuroendocrine tumors)
- Benzodiazepine receptors: $^{18}$F-flumazenil (Epilepsy)

***Hypoxia***

- $^{18}$F-MISO, $^{64}$Cu-ATSM

***Angiogenesis***

- $^{68}$Ga-RGD (arginine-glycine-aspartic acid)

## Applications

### *Neurology*

PET is extensively used in neurology. In patients with different subtypes of dementia, FDG-PET shows distinct spatial patterns of metabolism in the brain and can help clinicians to make a reasonably accurate early diagnosis, for appropriate management or prognosis. Specific patterns help differentiate Alzheimer's dementia, frontotemporal dementia, dementia in patients with mild cognitive impairment and HIV-dementia complex [5]. PET has an important role in initial staging and restaging of brain tumors. In gliomas, PET is done for the assessment of response to a certain anticancer therapy including its (predictive) effect on the patients' outcome and the differentiation of treatment-related changes (eg, pseudo-progression and radiation necrosis) from tumor progression at follow-up [6]. PET helps to identify the focus of seizures in drug refractory epilepsy thus guiding the surgical management. The utility of PET in different neuropsychiatric disorders is also being actively explored.

### *Nuclear Cardiology: SPECT and PET*

RMC has been carrying out radionuclide myocardial perfusion scintigraphy studies since more than three decades and over the years the technique itself has evolved, making it more reliable and robust, with additional ventricular functional

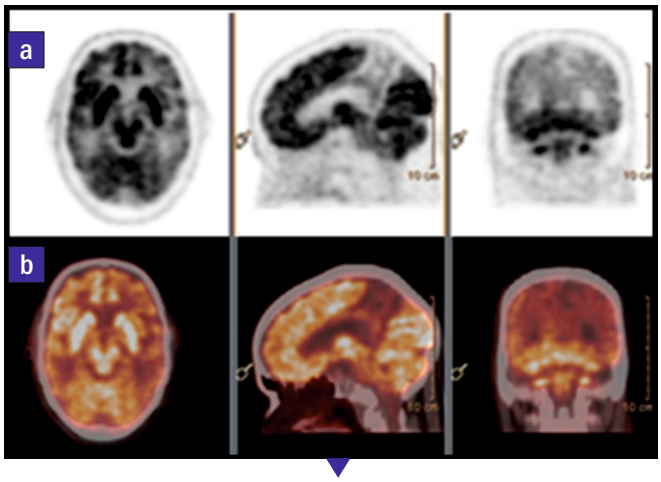


*Images of a 62 years old male with memory loss. FDG-PET (a) and PET/CT fused (b) axial, sagittal and coronal images show left posterior parietotemporal hypometabolism suggestive of early Alzhiemer's disease.*

*Non-FDG PET Radiotracers used at the Radiation Medicine Centre for patients*

| PET Radiotracers | Biochemical Process | Mechanism of Uptake or Localization | Clinical Indications |
|---|---|---|---|
| [18F] Fluoride | Bone metabolism | Incorporation in the hydroxyapatite crystals in bone | Evaluation of bone metastases/ benign bone lesions. |
| [18F] Fluorothymidine (FLT) | DNA synthesis | Substrates for thymidine kinase (TK-1) for DNA synthesis and reflects tumor cell proliferation rate | Disease Proliferation: carcinoma of brain, breast, lung, cervix, marrow disorders |
| [$^{18}$F]FMISO | Hypoxia | Intracellular reduction and binding | Brain tumors, breast carcinoma, myocardial ischemia |
| [18F] Fluoro-ethyl-tyrosine (FET) | Amino Acid | Amino acid metabolism & reflects tumor cell proliferation rate | Differential Diagnosis and grading of Brain tumors, Treatment response |
| $^{68}$Ga-DOTATATE | Receptor Binding | Specific binding to somatostatin receptor (SSTR-II, III, V) | Neuroendocrine tumors |
| $^{68}$Ga-PSMA-11 | Receptor Binding | Binding to Prostate-specific membrane antigen (PSMA), cell surface protein expressed abundantly in prostate carcinoma. | Castrate resistant prostate cancer |
| $^{68}$Ga- RGD (arginine-glycine-aspartic acid) | Angiogenesis | High affinity towards the integrin αvβ3 over-expressed on the tumor vasculature. | Carcinoma of thyroid, breast, lung, glioma, ischemic heart disease. |

information that further defines the prognosis in these patients. Thallium-201 chloride was used clinically for imaging myocardial perfusion scintigraphy studies at RMC before two decades. Because of its relatively long half-life and low-energy X-ray emission, it is not the ideal agent for imaging, giving a relatively large radiation dose with lower image quality than technetium agents. Since early part of the 2000s, 99mTc-MIBI radionuclide myocardial perfusion scintigraphy (MPS) has been established using as the main functional cardiac imaging technique at RMC for the assessment of ischaemic heart disease (IHD). Despite a growing number of alternative functional imaging techniques, MPS still remains the most widely used technique in assessing IHD and predicting prognosis.

Myocardial perfusion scintigraphy (MPS) using single photon emission computed tomography (SPECT) or positron emission tomography (PET) is a well-established mode of investigation in the diagnosis of acute-onset chest pain as well as evaluation of patients with known coronary artery disease. MPS is used to look at the changes in blood flow with stress. Traditionally, we use treadmill for physical stressing to increase oxygen demand in healthy arteries, leading to coronary vasodilatation and increased blood flow. In stenosed arteries, there is no increased flow despite the increased demand for oxygen. This results in ischaemia with associated symptoms (pain). In Fig.1 both normal and reversible perfusion defects have been shown.

In patients who are unable to do physical exercise, dobutamine can be used to the same effect. Direct infusion of adenosine for coronary vasodilatation was soon introduced at RMC since early 2000. This has a short half-life of about 10 s, with the effects being reversible within minutes of stopping the infusion. This made adenosine a fast, safe and reliable drug to use for assessing the myocardial perfusion reserve in normal coronary arteries and the loss of perfusion reserve in significantly stenosed coronary arteries (commonly termed "ischaemia"). These pharmacological agents are now widely used in RMC to assess myocardial perfusion with no loss of diagnostic accuracy for identifying significant stenosis. Other than referrals from major hospitals of Mumbai, we get more than 300 referrals for MIBI MPS studies from BARC hospital mainly for diagnosis of ischemic heart disease and also to look for significance of borderline coronary artery disease.

PET exhibits unparalleled advantages regarding the absolute quantitation of myocardial blood flow and myocardial flow reserve. Typical perfusion agents used in PET include O-15 $H_2O$, N-13 $NH_3$, and Rb-82, which have defined first-pass extraction fractions. Another promising agent for myocardial perfusion PET is F-18 flurpiridaz.

$^{18}$F-FDG PET cardiac imaging has a high sensitivity in detecting viable myocardium. FDG uptake is considered as the biomarker of viable myocardium and a perfusion/metabolism mismatch (i.e., impaired perfusion with increased/preserved metabolism) is characteristic of ischemic viable myocardium that should be rescued through a revascularization procedure. For the detection of viable myocardium, glucose loading with/without intravenous insulin injection is required to enhance F-18 FDG uptake in the normal and the ischemic viable myocardium. (7) We have used $^{18}$F-FDG PET scan to assess myocardial viability since the year 2002. This has a role in clinical practice in influencing patient management and improving clinical outcome. Unnecessary cardiac intervention thus can be avoided if FDG-PET study indicates no significant viable myocardium. In the next figure extensive viable myocardium is seen which after revascularization can improve left ventricular ejection fraction.

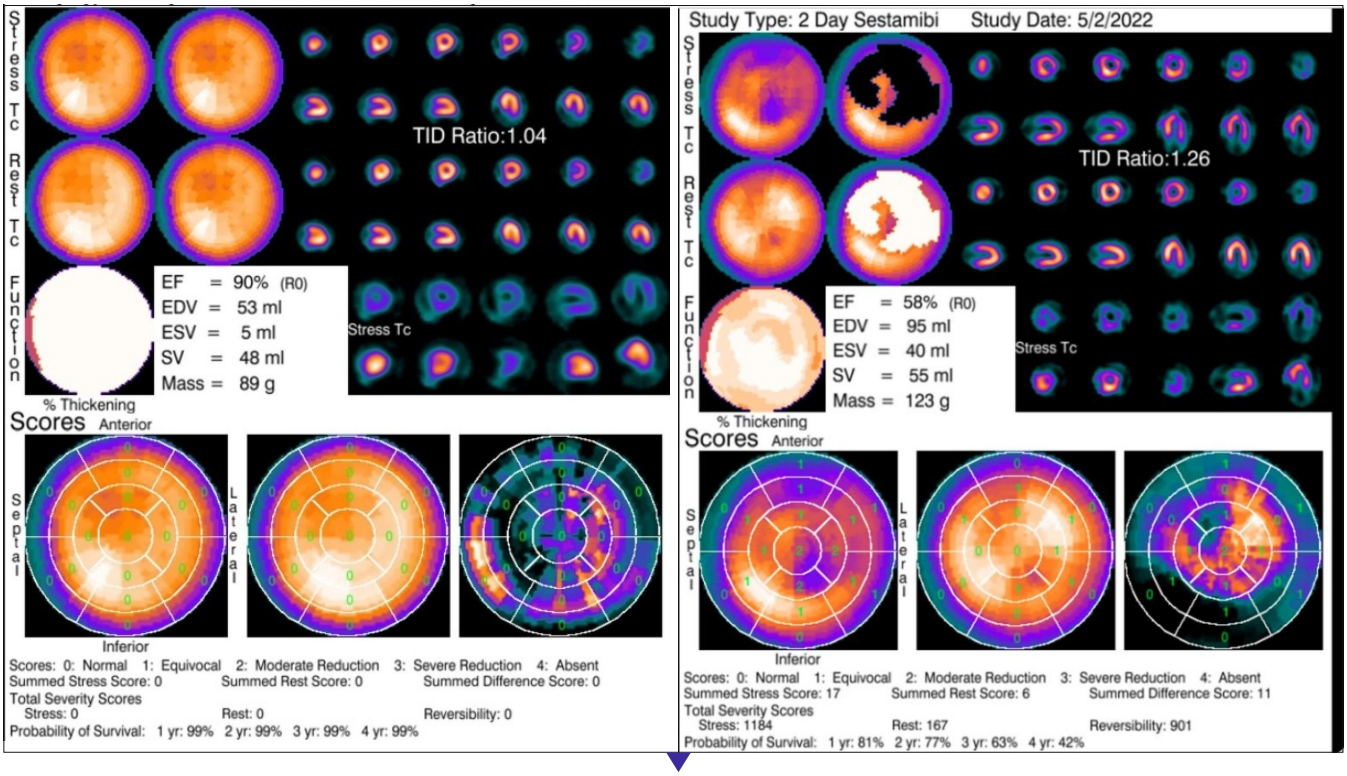


*Images on the left-hand side show normal myocardial perfusion and right sided images show reversible myocardial perfusion defects in antero-septal and antero-lateral segments.*

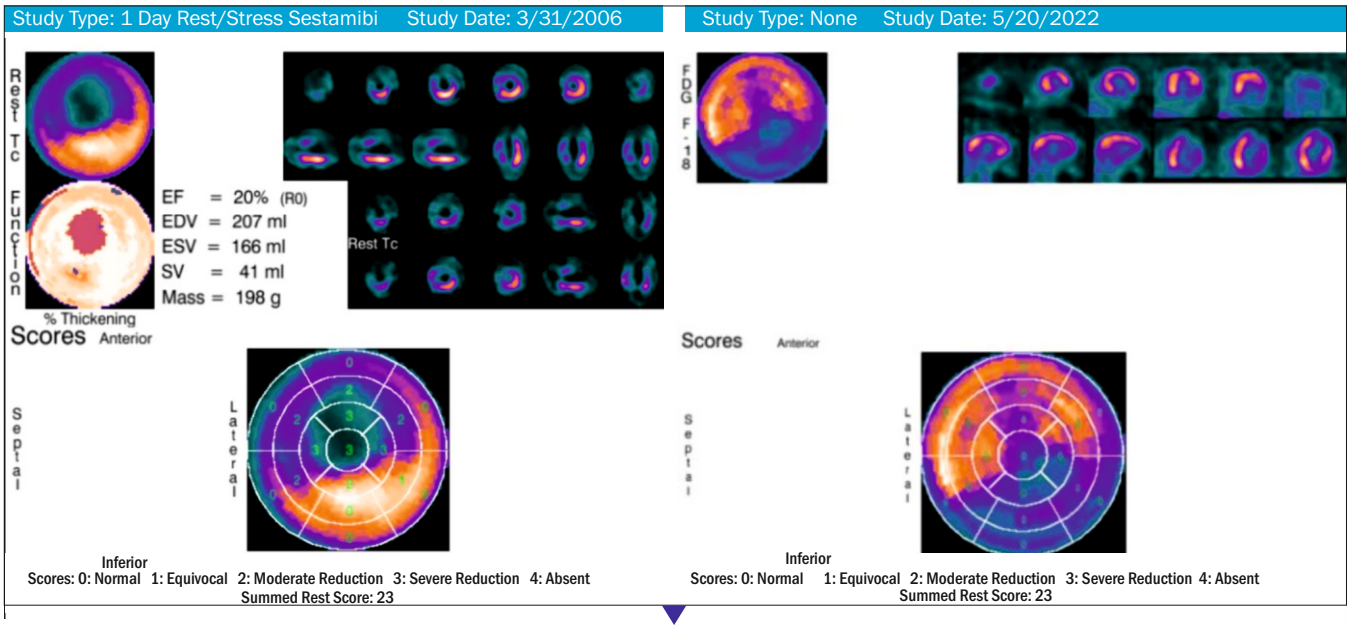


*The left sided images show large myocardial perfusion defects in antero-septal and antero-lateral segments and the right sided images show significant FDG uptake in corresponding antero-septal and antero-lateral segments, suggesting as viable myocardium.*

### *Oncology*

PET is extensively used in the management of various malignancies like lymphomas, lung cancer, head and neck cancers, breast carcinoma, gastro-intestinal malignancies (esophageal, gastric, GIST, colorectal and anal malignancies), genitourinary malignancies (bladder, penile, cervix, endometrial), melanoma, mesothelioma, multiple myeloma, neuroblastoma, paraneoplastic syndromes, sarcomas, thymic carcinoma and carcinoma of unknown primary [8].

### *Detection and Initial Staging of Tumor*

FDG-PET/CT has a vital role in the detection and staging of various malignancies, including lung carcinoma, breast carcinoma, lymphoma, carcinoma cervix and so on. It has been used in initial staging of patients with locally advanced or metastatic breast cancer or when conventional staging studies (e.g., CT or bone scan) are equivocal or suspicious and initial staging in patients with non-small cell lung cancer and selected patients with small cell lung cancer. PET helps in characterization of an indeterminate pulmonary nodule which is around 8-10 mm in diameter. In esophageal cancer, it helps in guiding the initial staging, primarily to assess resectability. In melanoma, PET helps in detection and localization of potential extranodal metastatic disease. PET forms a part of standard protocol in routine pre-treatment staging of patients with Hodgkin's lymphoma and different Non-Hodgkin Lymphoma subtypes. In colorectal cancer, it helps in pre-operative evaluation of patients with potentially resectable metastatic disease [2, 8, 9].

### *Monitoring Response to Treatment in Cancer*

PET/CT is often done as a baseline imaging prior to treatment and then during or post-treatment for early response assessment. It is performed in esophageal cancer following definitive chemoradiation and in lymphoma after chemotherapy and/or radiation therapy. Interim PET or early treatment response after two cycles of chemotherapy helps in prognostication and may modify treatment in lymphomas, if there is no response or there is progression of the disease seen on PET/CT [9]. In gastrointestinal stromal tumors (GIST), FDG-PET/CT has a definite role in staging and evaluation of the response to imatinib mesylate [9].

### *Restaging of Cancer and Follow-up Evaluation for Recurrence*

Early detection of recurrence is clinically important and can improve the prognosis and survival of patients with cancer. CT may underestimate the actual tumor burden by overlooking small tumor clusters in areas of distorted anatomy after treatment. FDG-PET is an effective whole-body imaging

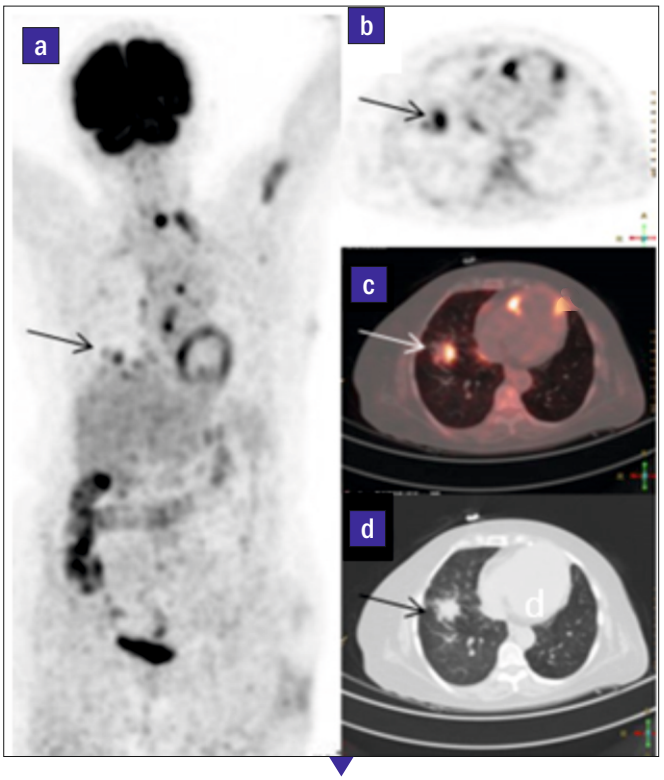


*The maximum intensity projection (MIP) (a) and axial PET (b), fused (c) and CT (d) images of a patient with carcinoma right lung show FDG avid 2 cm sized soft tissue mass involving the lower lobe of right lung, SUV max 4.62. The biopsy revealed adenocarcinoma. There was no evidence of metastatic disease and the tumor was deemed surgically resectable.*

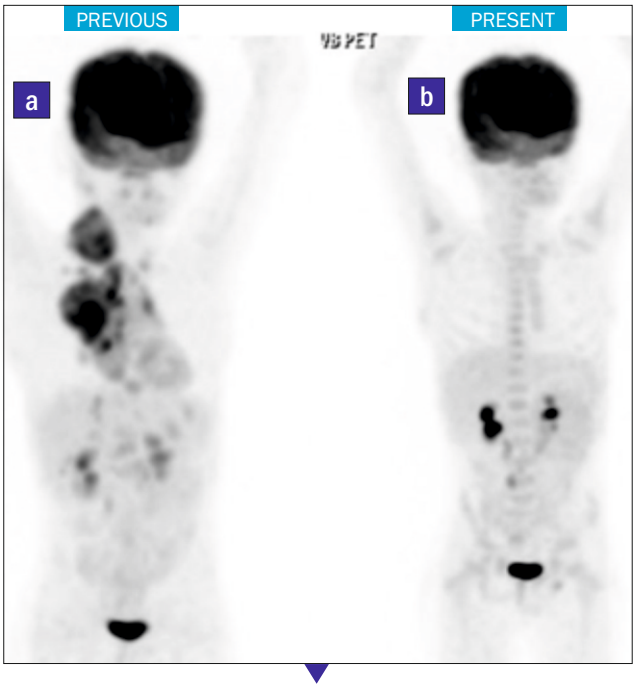


*FDG-PET MIP images (a) of a 27 years old male with diffuse large B cell lymphoma at initial staging (left image) PET/CT shows right cervical and mediastinal lymph nodal involvement. MIP (b) of the same patient after six cycles of chemotherapy showing no abnormal FDG uptake anywhere in the body suggesting complete metabolic response.*

technique that detects metabolic changes preceding structural findings [10]. PET/CT plays an important role in the evaluation of recurrent colorectal cancer with elevated CEA level (carcinoembryonic antigen). The recent studies show a very large role of FDG-PET/CT for detection of recurrence [8, 9, 10, 11, 12]. Many of these patients go on to receive treatment with curative intent, thus indicating the importance of early detection of recurrent disease [10, 11, 12] PET–CT is also a very helpful modality in the assessment of ovarian cancer recurrence; it can detect and localize the recurrence with high accuracy in this situation, thus can influence and modify the treatment plan, and reduces the need for second look surgery. A recent study showed the accuracy, sensitivity, specificity, of PET/CT scan were 95.77%, 85.7%, 97.89% respectively [13].

PET is also helpful in the follow-up or surveillance of various carcinomas like breast cancer (8). PET/CT has a high sensitivity in the early detection of relapse or second primary cancer in patients with head and neck squamous cell carcinomas, with significant management implications [13].

### *PET/ CT based Radiotherapy Planning*

PET/CT has been used in the radiotherapy (RT) planning of cervical cancer, lung cancer, head and neck cancers, brain tumors and more. It correctly delineates the diseased area so that the radiation can be targeted to the tumor cells and spare the normal cells. This improves the efficacy of the treatment and reduces toxicity to normal tissues [14].

FDG-PET/CT imaging has been used for contouring the target for RT, and has been shown to change the irradiated volume significantly compared with CT imaging alone. Modern advanced imaging techniques with image fusion and motion management in combination with current generation highly conformal RT techniques have increased the precision of RT, and have made it possible to reduce dramatically the risks of long-term side effects of treatment while maintaining the high cure rates for these diseases [15].

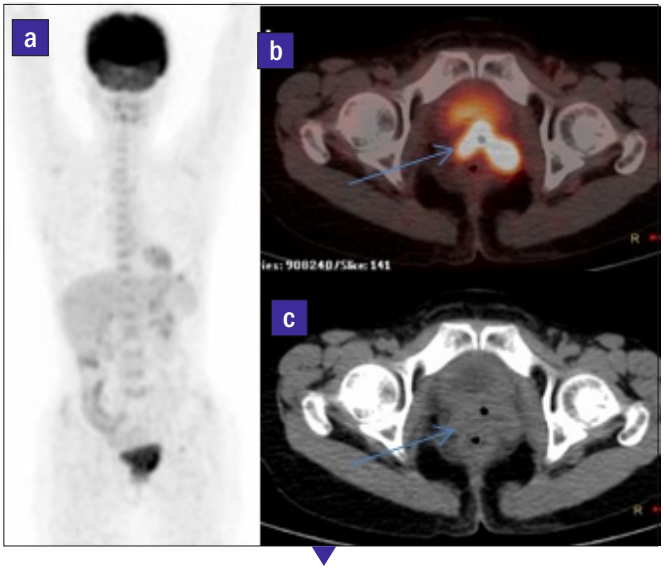


*Images of 42 years old female with carcinoma cervix, post-radiation therapy. $^{18}$F-FDG PET/CT (MIP, fused axial and CT) images reveal FDG avid soft tissue thickening in the cervix suggestive of residual active disease.*

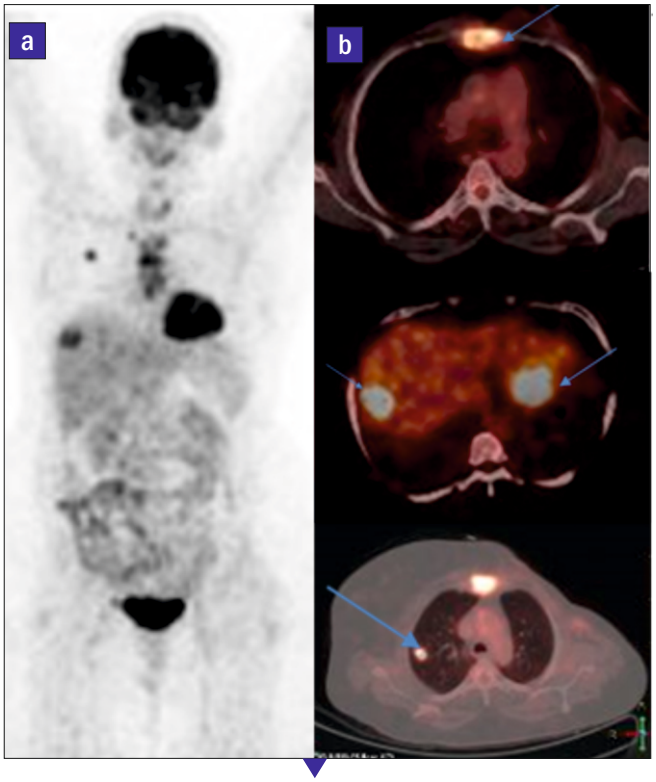


*Images of 48 years old female with carcinoma left breast, post-surgery, chemotherapy and radiation therapy 2 years previously, now presented with backache. FDG-PET/CT MIP (a) and fused axial (b) images showed recurrent metastatic disease in sternum (SUVmax 7.90), liver (SUVmax 7.97) and right lung (SUVmax 8.69).*

### *PET-CT guided Biopsy*

PET-directed biopsy has an increasing role in the diagnosis and staging of various diseases. Molecular image–guided biopsy approaches have great potential to increase the detection rate and improve diagnostic accuracy and therefore can have an impact on treatment decisions and patient care. If the biopsy is directed from the hypermetabolic area shown on the PET images, it is likely to result is revealing viable tumor cells and thus, give more definitive results. PET-CT guided biopsy are done for a variety of tumors including lung, breast, prostate and head and neck tumors [16].

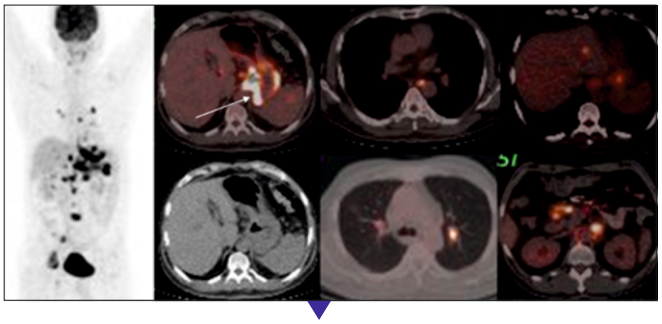

*50 years old male presented with unexplained weight loss. $^{18}$F-FDG PET/CT (MIP and fused axial images) done to look for unknown primary tumor, showed FDG avid wall thickening involving the proximal stomach, predominantly gastroesophageal junction (likely primary tumor), SUVmax 25.84, FDG avid paraesopaheal, gastrohepatic, perigastric, peripancreatic and retroperitoneal nodes. FDG avid hypodense liver lesion, multiple skeletal lesions, FDG avid nodule in upper lobe of left lung, 6mm, SUV max 12.29 (likely metastatic lesions). Gastroesophageal growth biopsy was reported as adenocarcinoma, poorly diferentiated.*

### *Unknown primary tumor in patients presenting with metastases*

Many times, patient presents with a swelling in the neck due to lymph node metastases or back pain due to bone metastases, or some other symptom due to metastatic disease. However, the primary remains unknown. Whole body $^{18}$F-FDG PET/CT is an effective method for detecting the primary tumors in patients with carcinoma of unknown primary. Additionally, it can also determine disease extent and contribute significantly to clinical patient management. The primary can be found in as either head and neck tumor or lung or breast tumor or other organs based upon the site of metastasis [17].

### Other Non-oncological Indications for PET-CT

Whole body FDG-PET/CT is a sensitive diagnostic technique for the evaluation of fever of unknown origin (FUO) by facilitating anatomical localization of focally increased FDG uptake, thereby guiding further diagnostic tests to achieve a final diagnosis. FDG-PET/CT has become a common procedure in the workup of FUO when other diagnostic clues are absent [18].

$^{18}$F-FDG-PET/CT has also been used in baseline evaluation and treatment response assessment in infectious diseases like tuberculosis (TB). It is particularly useful in detecting the disease in previously unknown sites, and allows the most appropriate site of biopsy to be selected. $^{18}$F-FDG-PET/CT is also very valuable in assessing early disease response to therapy, and plays an important role in cases where conventional microbiological methods are unavailable and for monitoring response to therapy in cases of multidrug-resistant TB or extrapulmonary TB [19].

However, there are few limitations of PET scan like limited resolution, physiological variations of FDG distribution, inability to detect mucinous tumors and radiation to the patient (about 6-10 mSv). Hence, judicious medical justification has to be made with every PET/CT referral.

### *Non-FDG Radiopharmaceuticals used for PET/CT Imaging*

*F-18 Sodium Fluoride (NaF) PET/CT:* It is used for imaging skeletal system evaluation, in oncology as whole body bone scan for evaluation of skeletal metastases, primary bone tumors and various benign skeletal conditions like

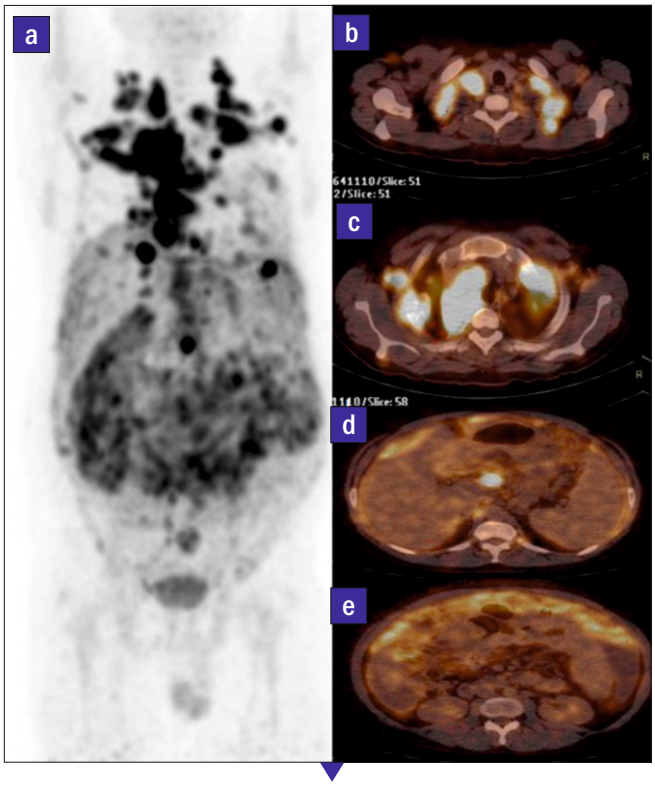


*FDG-PET/CT images of a 31 years old male with fever of unknown origin MIP (a) and axial fused images (b, c, d, e) showed FDG avid bilateral cervical, axillary, mediastinal and abdominal lymph nodes and omental deposits. Biopsy from the left cervical lymph node showed caseating granulomatous lymphadenitis and patient was diagnosed to have tuberculosis.*

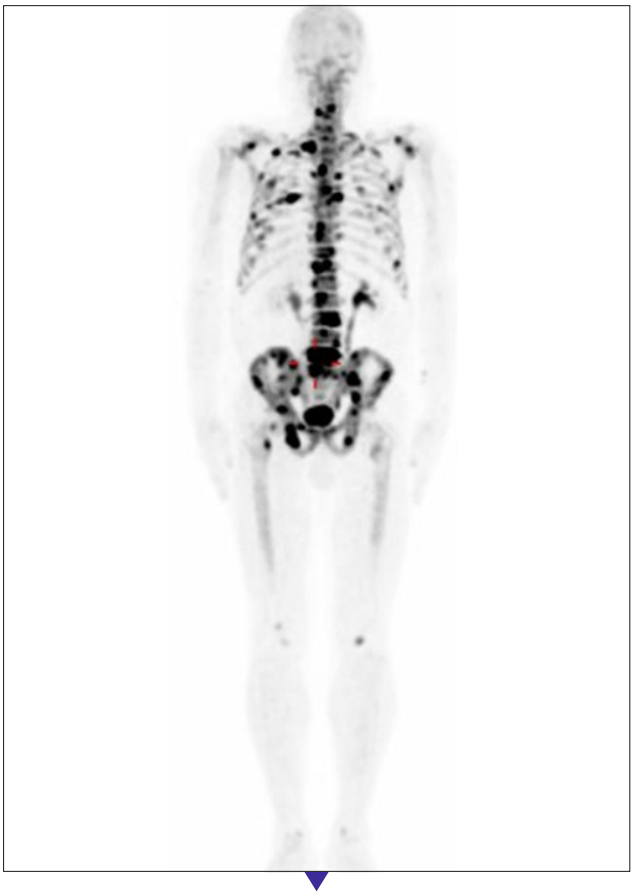

*$^{18}$F-fluoride PET/CT image (MIP) of 57 yrs old male with carcinoma prostate, serum PSA=335 ng/ml showing multiple foci of increased tracer uptake in the bones suggestive of extensive skeletal metastases.*

osteomyelitis, for bone graft viability and metabolic bone disease.

### $^{68}$Ga-PSMA-11 PET/CT

Prostate-specific membrane antigen (PSMA) is a type II transmembrane glycoprotein that is overexpressed in prostate carcinomas. PSMA expression is considered, at present, one of the most successful targets for therapy in nuclear medicine. It is used as an effective diagnostic and prognostic biomarker of prostate cancer. PSMA-based PET/CT imaging evolved as the procedure of choice in case of biochemical recurrence even with lower serum PSA levels, namely when PSMA-PET/CT scanning allows the optimization of the treatment strategy. 68Ga-PSMA-PET/CT was associated with sensitivity and specificity values of 33-93%, and >99% respectively in detecting recurrent disease [20]. To reduce the incidence of residual disease after surgery, PSMA-PET/CT should be considered also in patients with intermediate- and high-risk prostate carcinoma prior to radical prostatectomy. PSMA-PET is effective for imaging disease in the prostate, lymph nodes, soft tissue, and bone in a "one-stop–shop" examination. Finally, PSMA is an excellent theragnostic agent offering the possibility to highlight lesions by PET/CT imaging, and subsequently to irradiate metastatic sites with beta ($^{177}$Lu-PSMA-617) or alpha particle emitters ($^{225}$Ac-PSMA-617) [21].

### $^{68}$Ga-DOTATATE PET/CT

SSTR-based $^{68}$Ga-tetraazacyclododecanetetraacetic acid (DOTA)–peptide PET/CT is an exciting imaging modality that has shown significant advantages over conventional imaging in diagnosis and management of neuroendocrine tumors (NETs). It studies the somatostatin receptor (sstr) expression. In the recently updated National Comprehensive Cancer Network (NCCN) guidelines, $^{68}$Ga-DOTATATE PET/CT has been added as an appropriate evaluation tool along with site-specific anatomical imaging using multi-phase CT, multiphase MRI, or endoscopic ultrasound [22]. According to the SNMMI appropriate use criteria guidelines, SSTR based PET should be the preferred imaging modality for initial diagnosis, selection of patients for peptide receptor radionuclide therapy (PRRT), and localization of unknown primaries [22].

### PET/MRI

PET/MRI is the most recent development in the field of hybrid imaging. It may enable the potent for 'one stop shop' combination of anatomical, metabolic and molecular imaging. The PET/MR has applications in the field of neuroscience, oncology, musculoskeletal disease, etc., thus, turning out to be a frontier in the era of complementary hybrid imaging. Yet, it also requires further investigations on the various other applications of PET/MRI for pre-clinical and clinical trials [23].

Thus, in today's times, multimodality molecular imaging plays vital role in the diagnosis and management of various oncologic and non-oncological diseases. Artificial intelligence is also being explored in Nuclear Medicine in planning, image acquisition, interpretation, and reporting PET/CT with immense future potentials.

## Radionuclide Therapy

A number of new radionuclides & radiopharmaceuticals have been developed for different therapeutic applications in nuclear medicine. The choice of a particular radiopharmaceutical is dependent upon to a large extent by the diagnosis and character of the disease, the appropriate emissions, linear energy transfer, and physical half-life and by the carrier used to selectively transport the radionuclide to the desired site [24].

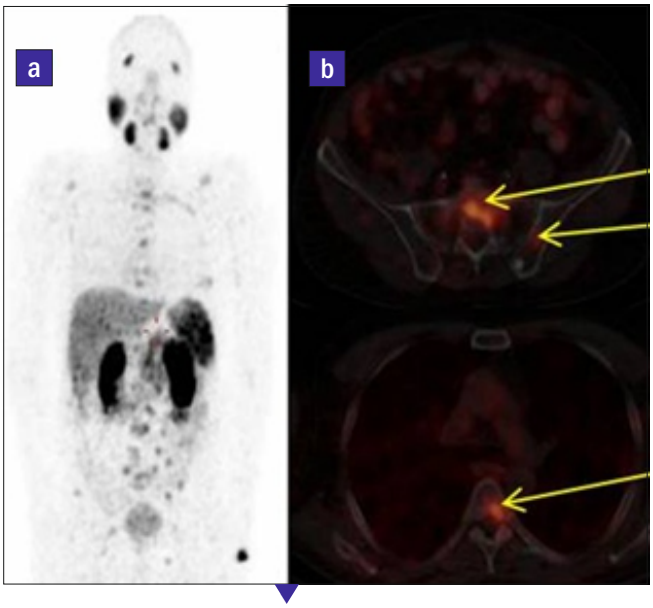


*$^{68}$Ga-PSMA-11 PET/CT images of 72 year old man with castration resistant prostate adenocarcinoma, post radical prostatectomy, hormonal therapy and chemotherapy. Presented with raised serum PSA of 52 ng/ml. Images show multiple foci of increased tracer uptake in the bones as shown in MIP (a) and axial fused images of representative skeletal metastatic sites. The patient was subsequently referred for $^{177}$Lu-PSMA-617 therapy.*

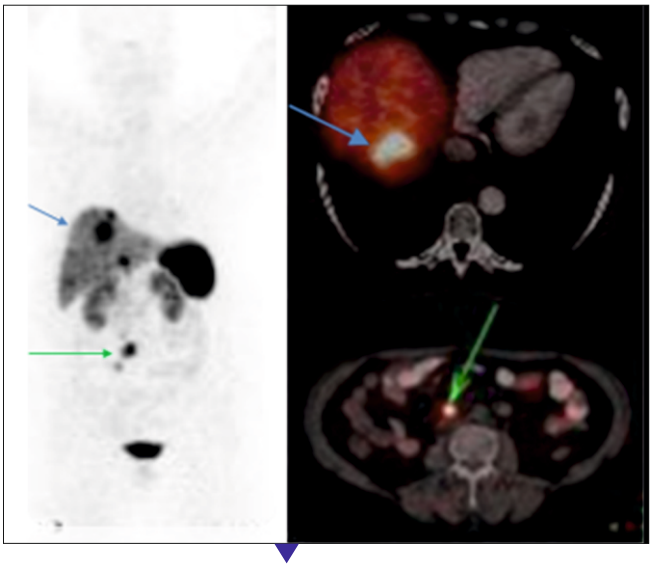

*$^{68}$Ga-DOTATATE PET/CT MIP and fused axial images of a 67 years old male with pancreatic neuroendocrine tumor (MIB1-20%), post-surgery, showing liver (blue arrow) and paraaortic lymph nodal metastasis (arrow). The patient was subsequently referred for PRRT.*

### Thyroid

Thyroid disorders have been successfully treated by means of administration of radioiodine ($^{131}$I-NaI) since the 1940s. The efficacy and safety of this treatment and the advantages over thyroid surgery made its success worldwide, and recommendations have been released by several scientific societies including the European Association of Nuclear Medicine and Molecular Imaging and the American Society of Nuclear Medicine. Radioactive I-131, given its abundant beta and gamma emissions and its mode of uptake similar to the normal physiological uptake of elemental iodine in the thyroid gland, has been a logical choice for treating a number of benign and malignant thyroid disorders. The

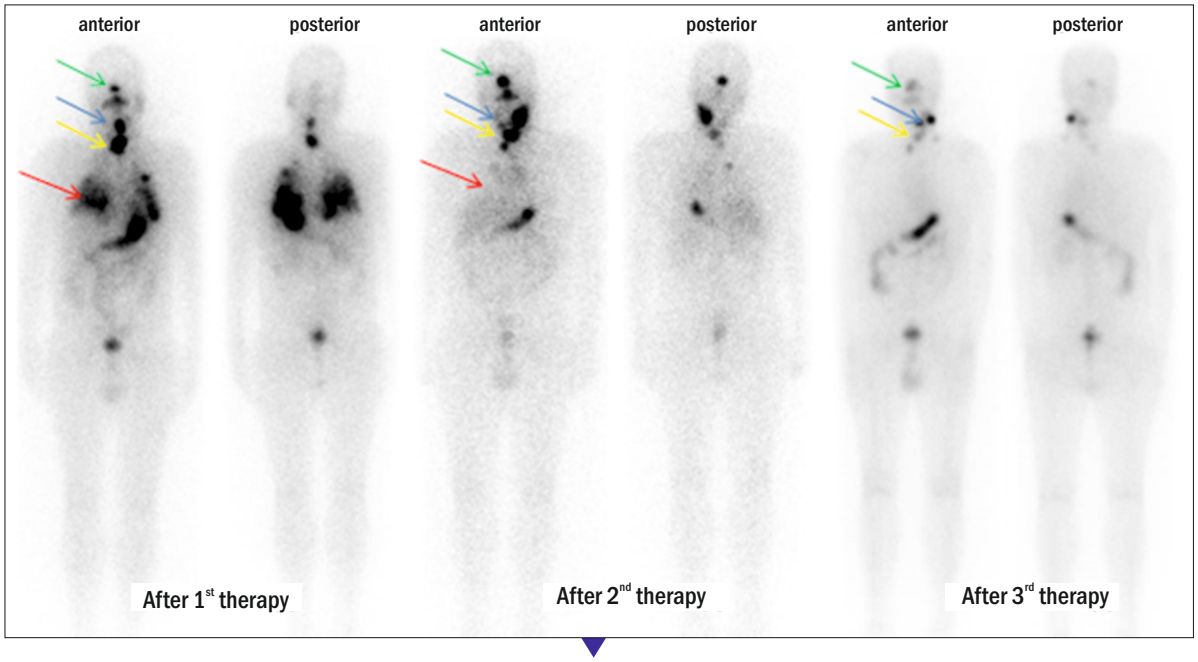


*Iodine-131post-therapy scan images of 31 years old male with papillary carcinoma thyroid with thyroid bed residual (yellow arrow) and metastatic disease in cervical nodes (blue arrow), both lungs (red arrow) and base of skull (green arrow) showing radiotracer uptake after 1st therapy. Images after 2nd therapy and 3rd therapy show decrease in the cervical nodes and base of skull metastases and resolution of lung metastases (cumulative I-131 dose 721 mCi).*

indications for $^{131}$I treatment of thyroid benign diseases include hyperthyroidism and subclinical hyperthyroidism (about 8–10 mCi), toxic nodular goiter and autonomously functioning toxic nodule (higher activities may be needed in the latter conditions). Differentiated thyroid cancers are typically iodine-avid and can be effectively treated with radioiodine. In most patients, radioactive iodine therapy (RAI) is done for ablation of residual tissue or with adjuvant intent in case of suspected persistent disease after surgery [25]. Post surgical I-131 ablation of normal thyroid remnants permits using the serum thyroglobulin as a tumor marker. I-131 ablation may also help treat microscopic disease. I-131 therapy has been used for locoregional neck, mediastinal, and distant thyroid cancer metastases, while it is not useful for treating patients with anaplastic, or medullary thyroid cancer. Patients with low risk and no known metastases are commonly treated with 30 to 50 mCi to ablate normal remaining thyroid tissue. Those with regional metastases typically receive 100 to 150 mCi and with distant metastases receive 200 to 250 mCi [26]. Over the years, radioiodine therapy of differentiated thyroid cancer has proven to be an effective and low-risk treatment for eradication of thyroid remnant after total thyroidectomy, to theoretically destroy suspected but unproven residual disease after surgery (adjuvant therapy) or in patients with metastatic disease with curative or palliative intent [25].

### *Peptide receptor radionuclide therapy (PRRT)*

The somatostatin receptor targeted PRRT is now considered as an important treatment modality for advanced, metastatic or inoperable, progressive Neuroendocrine neoplasms. $^{177}$Lu-DOTA-TATE and $^{90}$Y-DOTA-TOC/TATE (beta emitters) have received regulatory approvals in multiple countries, and more recently $^{225}$Ac-DOTA-TATE (alpha emitter) is used as an investigational agent. The efficacy of PRRT is assessed in 3 scales: symptomatic response and improvement in health related quality of life (HRQoL), biochemical response in terms of reduction/increase in tumor markers (serum CgA, 24 hours urinary 5-HIAA levels) and imaging response (by RECIST and PERCIST scales). The patients have shown remarkable symptomatic improvement and better quality of life (including those with functioning disease uncontrolled with SSAs such as long acting octreotide/lanreotide) [27]. A recent study reported symptomatic improvement in 90% of patients. The biochemical response in terms of reduction of serum CgA/urinary 5-HIAA is in around 60%-70% of patients. On imaging, partial objective response was seen in around 30% of patients (complete response in 2%-6%). Additionally, stable disease is documented on imaging (either RECIST or PERCIST scale assessment) in around 60% who had otherwise demonstrated progressive disease on octreotide or lanreotide [28].

### *PSMA based radioligand therapy (PRLT)*

Patients with metastatic castration resistant prostate carcinoma (mCRPC) are treated with androgen receptor signaling targeted inhibitors, such as abiraterone and

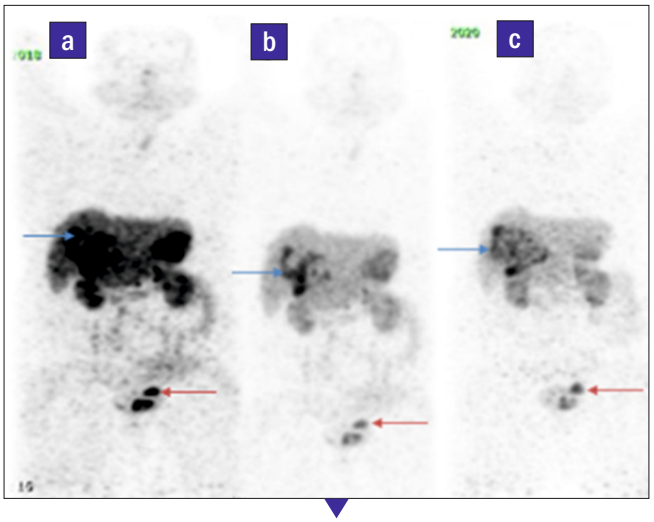


*$^{68}$Ga -DOTATATE PET MIP Images of 60 years old female with colorectal neuroendocrine tumour (MIB1 index: 20%) with liver metastases. $^{68}$Ga-DOTATATE MIP images at baseline (a) shows SSTR expressing rectal lesion and liver metastases. Images after 2 cycles of PRRT (177Lu-DOTA-TATE) (b) and 6 cycles of PRRT (c) show necrosis and disease stabilization.*

enzalutamide, and chemotherapy such as docetaxel and cabazitaxel. More recently, PSMA targeted therapy has been used. Patients with end-stage mCRPC responded better to treatment with $^{177}$Lu-PRLT than patients with mCRPC resistant to two lines of established drugs to third-line treatment [29]. A prospective study by Hofman et al showed that PRLT had an impressive response rate and tolerability. A preliminary presentation of a prospective randomized trial, TheraP, NCT03392428, ClinicalTrials.gov, supports that PRLT gives a better outcome than third-line treatment with cabazitaxel [30]. Oncologists can use the findings to optimize patient selection, predict treatment outcomes, and improve the effect of PRLT [31].

### *Radionuclide therapy for bone pain palliation*

The skeleton is a potential metastatic target of many malignant tumors. Up to 85% of prostate and breast cancer patients may develop bone metastases causing severe pain in many of them. In patients suffering from multilocular, mainly osteoblastic lesions and pain syndrome, systemic radionuclide therapy is recommended for pain palliation. Low-energy beta-emitting radionuclides ($^{153}$Samarium-ethylenediaminetetrameth-ylenephosphonate (EDTMP) and $^{89}$Strontium chloride) deliver high radiation doses to bone metastases and micrometastases in the bone marrow, but only negligible doses to the hematopoietic marrow. The response rate regarding pain syndrome is about 75%; about 25% of the patients may even become pain free. The therapy is repeatable, depending on cell counts. Concomitant treatment with modern bisphosphonates does not interfere with the treatment effects. Clinical trials using new radionuclides like $^{223}$Radium and/or combinations of chemotherapy and radionuclides are aiming at a more curative approach [32].

### *Radioimmunotherapy (RIT)*

RIT has been in use and has progressed significantly with the discovery of new molecular targets, the development of new stable chelates, the humanization of monoclonal antibodies (mAbs), and the use of pre-targeting techniques. Two products targeting the CD20 antigen are approved in the treatment of B cell lymphoma: $^{131}$I-tositumomab (Bexxar) and $^{90}$Y-ibritumomab tiuxetan (Zevalin). RIT can be integrated in clinical practice for treatment of patients with relapsed or refractory follicular lymphoma or as consolidation after induction chemotherapy in frontline treatment in FL patients. High-dose treatment, RIT as consolidation, RIT in the first-line treatment, fractionated RIT, and use of new humanized mAbs, in particular targeting CD22, showed promising results in B cell lymphoma. In solid tumors, that are more resistant to radiations and less accessible to large molecules such as mAbs, clinical efficacy remains limited. Pre-targeting approaches have been of potential in increasing the therapeutic index of radiolabeled antibodies. Finally, new beta emitters such as lutetium-177 (like $^{177}$Lu-Trastuzumab for breast carcinoma or $^{177}$Lu-Rituximab) with better physical properties will further enhance the safety and applicability of RIT. Moreover, alpha emitters such as Bismuth-213 or Astatine-211 offer the theoretical possibility to eradicate the last microscopic clusters of tumor cells, in the setting of consolidation. Personalized dosimetry protocols, particularly based on quantitative positron emission tomography (PET) imaging, is considered to be developed to optimize injected activity [33].

### *$^{131}$I- Metaiodobenzylguanidine (MIBG) therapy*

MIBG is structurally similar to the neurotransmitter norepinephrine and specifically targets neuroendocrine cells

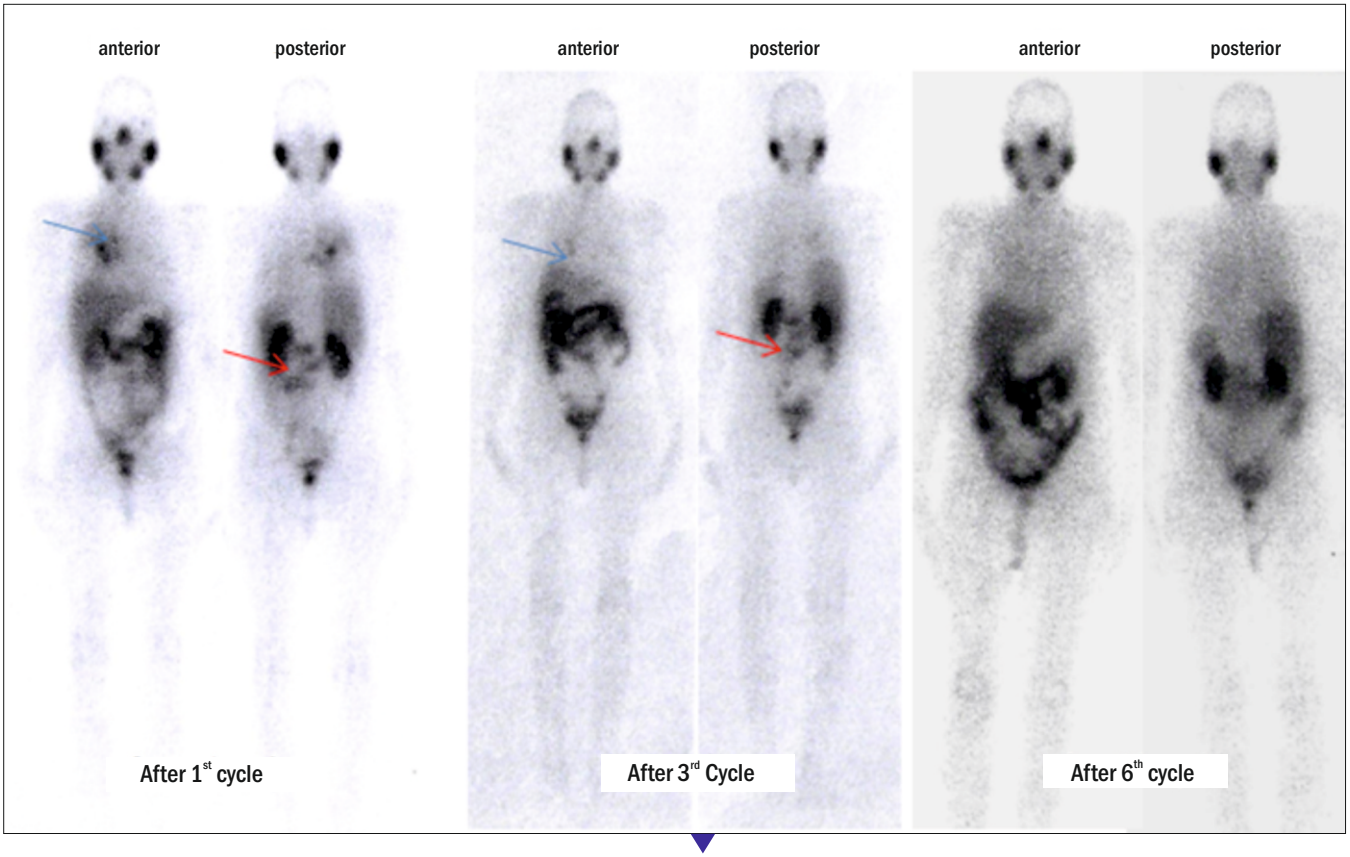


*Post $^{177}$Lu-PSMA-617 therapy scan images of 71 years old male with metastatic castration resistant prostate cancer with mediastinal nodes (blue arrow) and lower lumbar vertebral metastases (red arrow) showing radiotracer uptake in scan after 1st therapy. Images after 3rd cycle and 6th cycle show reduction and subsequent resolution of these lesions.*

including some neuroendocrine tumors. The indications of I-131 MIBG therapy include treatment-resistant neuroblastoma, unresectable or metastatic pheochromocytoma and paraganglioma, unresectable or metastatic carcinoid tumors, and unresectable or metastatic medullary thyroid cancer (MTC). I-131 MIBG therapy is one of the considerable effective treatments in patients with advanced neuroblastoma, pheochromocytoma, and paraganglioma. On the other hand, I-131 MIBG therapy is an alternative method after more effective novel therapies are used such as radiolabeled somatostatin analogs and tyrosine kinase inhibitors in patients with advanced carcinoid tumors and MTC [34].

### *Targeted alpha therapy*

Targeted alpha therapy attempts to deliver systemic radiation selectively to cancer cells while minimizing systemic toxic effects and may lead to additional treatment options for many cancer types. Alpha-emitting radionuclides have been approved for cancer treatment since 2013, with increasing degrees of success, as new targets, synthetic chemistry approaches, and alpha particle emitters are identified. From a radiobiological perspective, alpha particles are more effective at killing cells compared to low linear energy transfer radiation. The short range of alpha particles makes them a potent tool to irradiate small lesions or treat solid tumors by minimizing unwanted irradiation of normal tissue surrounding the cancer cells, assuming a high specificity of the radiopharmaceutical and good stability of its chemical bonds. Clinical approval of $^{223}RaCl_2$ in 2013 was a major milestone. In addition, $^{225}$Ac-PSMA-617 treatment benefit in metastatic castrate-resistant prostate cancer patients, refractory to standard therapies, is another remarkable achievement [35].

Thus, the therapeutic applications of systemic radiopharmaceuticals have been in use since many decades and are rapidly progressing to achieve more efficacy and treatment response in various tumors like thyroid cancer, prostate cancer, neuroendocrine tumors, and more. Newer approaches like targeted alpha therapy are opening new avenues of treating a variety of cancers while sparing the surrounding normal tissue most effectively.

## References


[1] https://www.iaea.org/sites/default/files/gc/gc54inf-3-att1_en.pdf

[2] Kapoor V., McCook BM., Torok FS. An introduction to PET-CT imaging. Radiographics. 2004 Mar-Apr; 24(2):523-43. doi: 10.1148/rg.242025724. PMID: 15026598.

[3] Shahhosseini S. PET Radiopharmaceuticals. Iran J Pharm Res. 2011 Winter; 10(1):1-2. PMID: 24363674; PMCID: PMC3869596.

[4] Duncan K. Radiopharmaceuticals in PET imaging. J Nucl Med Technol. 1998 Dec;26(4):228-34; quiz 242. PMID: 9884933.

[5] Shivamurthy VK., Tahari AK., Marcus C, Subramaniam RM. Brain FDG PET and the diagnosis of dementia. AJR Am J Roentgenol. 2015 Jan; 204(1):W76-85.

[6] Galldiks N., Lohmann P., Albert NL, Tonn JC, Langen KJ. Current status of PET imaging in neuro-oncology. Neurooncol Adv. 2019 May 28;1(1):vdz010. doi: 10.1093/noajnl/vdz010. PMID: 32642650; PMCID: PMC7324052.

[7] Lee WW. Recent Advances in Nuclear Cardiology. Nucl Med Mol Imaging. 2016 Sep; 50(3):196-206. doi: 10.1007/s13139-016-0433-x. Epub 2016 Jul 13. PMID: 27540423; PMCID: PMC4977260.

[8] 18F-fluorodeoxyglucose (FDG) PET and PET/CT Practice Guidelines in Oncology A summary of the recommendations and practice guidelines of professional groups (2013). Practice guidelines from the SNM, National Comprehensive Cancer Network (NCCN) summarized for major cancer types. (2013) https://www.snmmi.org/Membership/Content.aspx?ItemNumber=5181

[9] Agrawal A., Rangarajan V. Appropriateness criteria of FDG PET/CT in oncology. Indian J Radiol Imaging. 2015 Apr-Jun; 25(2):88-101. doi: 10.4103/0971-3026.155823. PMID: 25969632; PMCID: PMC4419439.

[10] Israel O., Kuten A. Early detection of cancer recurrence: 18F-FDG PET/CT can make a difference in diagnosis and patient care. J Nucl Med. 2007 Jan; 48 Suppl 1:28S-35S. PMID: 17204718.

[11] Khan K., Athauda A., Aitken K., Cunningham D., Watkins D., Starling N., Cook GJ., Kalaitzaki E, Chau I, Rao S. Survival Outcomes in Asymptomatic Patients With Normal Conventional Imaging but Raised Carcinoembryonic Antigen Levels in Colorectal Cancer Following Positron Emission Tomography-Computed Tomography Imaging. Oncologist. 2016 Dec; 21(12):1502-1508. doi: 10.1634/theoncologist.2016-0222. Epub 2016 Oct 14. PMID: 27742904; PMCID: PMC5153343.

[12] ElHariri, M.A.G., Harira, M. & Riad, M.M. Usefulness of PET–CT in the evaluation of suspected recurrent ovarian carcinoma. Egypt J RadiolNucl Med50, 2 (2019). https://doi.org/10.1186/s43055-019-0002-2.

[13] Kostakoglu L, Fardanesh R, Posner M, et al. Early detection of recurrent disease by FDG-PET/CT leads to management changes in patients with squamous cell cancer of the head and neck. Oncologist. 2013; 18(10):1108-1117. doi:10.1634/theoncologist.2013-0068

[14] An insight into PET-CT based radiotherapy treatment. planning. Ramachandran Prabhakar et al. Cancer Therapy Vol 5, 519-524, 2007

[15] Specht L, Berthelsen AK. PET/CT in Radiation Therapy Planning. Semin Nucl Med. 2018 Jan; 48(1):67-75. doi: 10.1053/j.semnuclmed.2017.09.006. Epub 2017 Oct 10. PMID: 29195619.

[16] PET Molecular Imaging–Directed Biopsy: A Review. Baowei Fei and David M. Schuster American Journal of Roentgenology 2017 209:2, 255-269.

[17] Diagnostic Value of 18F-FDG PET/CT in Patients with Carcinoma of Unknown Primary Mol Imaging RadionuclTher 2018;27:126-132 DOI:10.4274/mirt.64426 ArzuCengiz, SibelGöksel, YakupYürekli Adnan Menderes.

[18] Kouijzer IJE, Mulders-Manders CM, Bleeker-Rovers CP, Oyen WJG. Fever of Unknown Origin: the Value of FDG-PET/CT. Semin Nucl Med. 2018 Mar; 48(2):100-107. doi: 10.1053/j.semnuclmed.2017.11.004. Epub 2017 Dec 8. PMID: 29452615.

[19] Yu WY, Lu PX, Assadi M, et al. Updates on 18F-FDG-PET/CT as a clinical tool for tuberculosis evaluation and therapeutic monitoring. Quant Imaging Med Surg. 2019; 9(6):1132-1146. doi:10.21037/qims.2019.05.24.

[20] Fitzpatrick C, Lynch O, Marignol L. 68Ga-PSMA-PET/CT Has a Role in Detecting Prostate Cancer Lesions in Patients with Recurrent Disease. Anticancer Res. 2017 Jun; 37(6):2753-2760. doi: 10.21873/anticanres.11627. PMID: 28551611.

[21] Ceci, F., Fanti, S. PSMA-PET/CT imaging in prostate cancer: why and when. Clin Transl Imaging 7, 377–379 (2019).

[22] Walker RC, Smith GT, Liu E, Moore B, Clanton J, Stabin M. Measured human dosimetry of 68Ga-DOTATATE. J Nucl Med. 2013 Jun; 54(6):855-60. doi: 10.2967/jnumed.112.114165. Epub 2013 Mar 20. PMID: 23516312; PMCID: PMC4472480.

[23] Musafargani, S., Ghosh, K.K., Mishra, S. et al. PET/MRI: a frontier in era of complementary hybrid imaging. European J Hybrid Imaging 2, 12 (2018).

[24] Srivastava S, Dadachova E. Recent advances in radionuclide therapy. Semin Nucl Med. 2001 Oct; 31(4):330-41. doi: 10.1053/snuc.2001.27043. PMID: 11710775.

[25] Bombardieri, E., Seregni, E., Evangelista, L., CHIESA, C., Chiti, A. (Eds.) Clinical Applications of Nuclear Medicine Targeted Therapy,1st ed., 2018.SPRINGER.

[26] Harvey A. Ziessman, Janis P. O'Malley, James H. Thrall. NUCLEAR MEDICINE: THE REQUISITES, 4th ed., 2014.Elsevier Mosby, Philadelphia.

[27] Basu S., Parghane RV., Kamaldeep, Chakrabarty S. Peptide Receptor Radionuclide Therapy of Neuroendocrine Tumors. Semin Nucl Med. 2020 Sep; 50(5):447-464. doi: 10.1053/j.semnuclmed.2020.05.004. Epub 2020 Jul 3. PMID: 32768008.

[28] Thapa P., Ranade R., Ostwal V., et al: Performance of 177Lu-DOTATATEbased peptide receptor radionuclide therapy in metastatic gastroenteropancreatic neuroendocrine tumor: a multiparametric response evaluation correlating with primary tumor site, tumor proliferation index, and dual tracer imaging characteristics. Nucl Med Commun 37:1030-1037, 2016.

[29] von Eyben, F.E.; Roviello, G.; Kiljunen, T.; Uprimny, C.; Virgolini, I.; Kairemo, K.; Joensuu, T. Third-line treatment and (177)Lu-PSMA radioligand therapy of metastatic castration-resistant prostate cancer: A systematic review. Eur. J. Nucl. Med. Mol. Imaging 2018, 45, 496–508.

[30] Hofman, M.; Emmett, L.; Sandhu, S.; Iravani, A.; Joshwa, A.; Goh, J.; Patterson, D.; Tan, S.; Kirkwood, S.; Ng, S.; et al. ASCO20. A randomized phase II trial of 177Lu-PSMA 617 (Lu-PSMA) theranostics versus cabazitaxel in metastatic castration-resistant prostate cancer (mCRPC) progressing after docetaxel: Initial results (ANZUP protocol 1603). J. Clin. Oncol. 2020.

[31] von Eyben FE., Bauman G., von Eyben R., Rahbar K., Soydal C., Haug AR, Virgolini I, Kulkarni H, Baum R, Paganelli G. Optimizing PSMA Radioligand Therapy for Patients with Metastatic Castration-Resistant Prostate Cancer. A Systematic Review and Meta-Analysis. Int J Mol Sci. 2020 Nov 28; 21(23):9054. doi: 10.3390/ijms21239054. PMID: 33260535; PMCID: PMC7730994.

[32] Fischer M., Kampen WU. Radionuclide Therapy of Bone Metastases. Breast Care (Basel). 2012; 7(2):100-107. doi:10.1159/000337634.

[33] Kraeber-Bodéré, F. et al. "New Advances in Radioimmunotherapy for the Treatment of Cancers." (2015).

[34] Kayano D, Kinuya S. Current Consensus on I-131 MIBG Therapy. Nucl Med Mol Imaging. 2018;52(4):254-265. doi:10.1007/s13139-018-0523-z.

[35] Guerra Liberal FDC, O'Sullivan JM, McMahon SJ, Prise KM. Targeted Alpha Therapy: Current Clinical Applications. Cancer BiotherRadiopharm. 2020 Aug; 35(6):404-417. doi: 10.1089/cbr.2020.3576. Epub 2020 Jun 16. PMID: 32552031.

# Rapid Hazard Assessment

7

# Earthquake Location using Genetic Algorithm

**Ajit Kundu* and Pratap Mane**

*Seismology Division, Electronics and Instrumentation Group, Bhabha Atomic Research Centre, Trombay – 400085, INDIA*

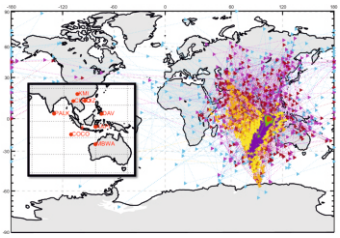

*Optimization in 2D search space*

ABSTRACT

For achieving accurate, bias-free earthquake locations genetic algorithm (GA) has been used. This algorithm minimizes the misfit between observed and calculated arrival times of P waves recorded on a multi-station network. The location parameters of 16 earthquakes that occurred at and around the Sumatra region have been estimated using P onsets recorded at around 10 stations of the Global Seismographic Network (GSN) surrounding the Sumatra region. The study shows that most of the estimates are accurate enough except for one event which reclines far outside the network. This method is very efficient for estimating the location of events that occurs well inside the recording network.

KEYWORDS: *Earthquake, Genetic algorithm, Global Seismographic Network*

## Introduction

The most fundamental problem in seismology is the estimation of earthquake location. The earthquake location is defined by the earthquake hypocentre and the origin time. The hypocentre is the physical location, usually given in latitude, longitude, and depth below the surface. Reliable knowledge of hypocentre and origin time has tremendous importance for the studies such as the determination of earthquake magnitude, focal mechanism, and stress conditions around the source which are crucial for rapid hazard assessment and emergency responses.

The shape of the seismograms depends vastly on the relative positions of the recording instruments and source. The process of earthquake location using these seismograms is an inverse problem. The depth-dependent gradients and discontinuities in the velocity distribution within the Earth make this inverse problem highly non-linear and non-trivial to solve.

Mathematical fundamentals of earthquake location methods were established more than a century ago. These are namely, graphical methods [1], simple grid searches [2] and the linearized inversion method [3]. Since then various location methods have been developed to improve the accuracy of the location. These improvements have enabled semi-automation of the event location process, which is employed at many earthquake centres worldwide (e.g. the International Seismological Centre (ISC), the United States Geological Survey (USGS), and National Earthquake Information Centre (NEIC)).

Based on the number of earthquakes to locate, location techniques can be broadly classified into two groups, namely, single–event location techniques [4-10] that locate one event at a time and multiple–event location techniques [11-13] that locate multiple events simultaneously. Depending on the spatial type, there are the absolute location that is determined with respect to a fixed geographic coordinate system and a fixed time standard, and the relative location that is computed with respect to another event (an earthquake or explosion) which might have an uncertain absolute location [4]. Moreover, relying on the methodology employed, location techniques can be linear, nonlinear and probabilistic.

The genetic algorithm (GA) is a global optimization technique and a useful tool for solving non-linear problems with many local minima or maxima. It was developed by Holland [14]. For the present study, GA has been used to minimize the misfit between observed and calculated arrival times to determine earthquake location parameters. The novel feature of GA is that it works with many estimates of the location at once and uses the properties of the cluster of estimates to drive the optimization process and reach finally to the global minimum. In this study, 16 events of various depths and magnitudes (Mw>6) from in and out of the Sumatra region have been selected. The selected (around 10) recording stations of GSN well surrounds the Sumatra region. GA generates a pool of location parameters, uses a 3D velocity model to compute arrival times (i.e., P onsets) at the selected stations and minimizes the misfit between observed and calculated arrival times to estimate the location parameters. The study reveals that the estimated parameters are accurate

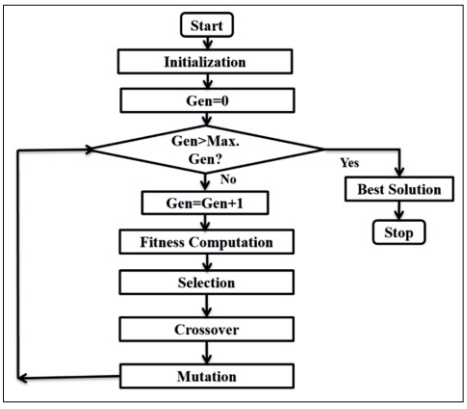


*Fig.1: Working of GA. Gen and Max. Gen represent generation and maximum value of generation respectively.*

**Author for Correspondence: Ajit Kundu*
*E-mail: ajitkun@barc.gov.in*

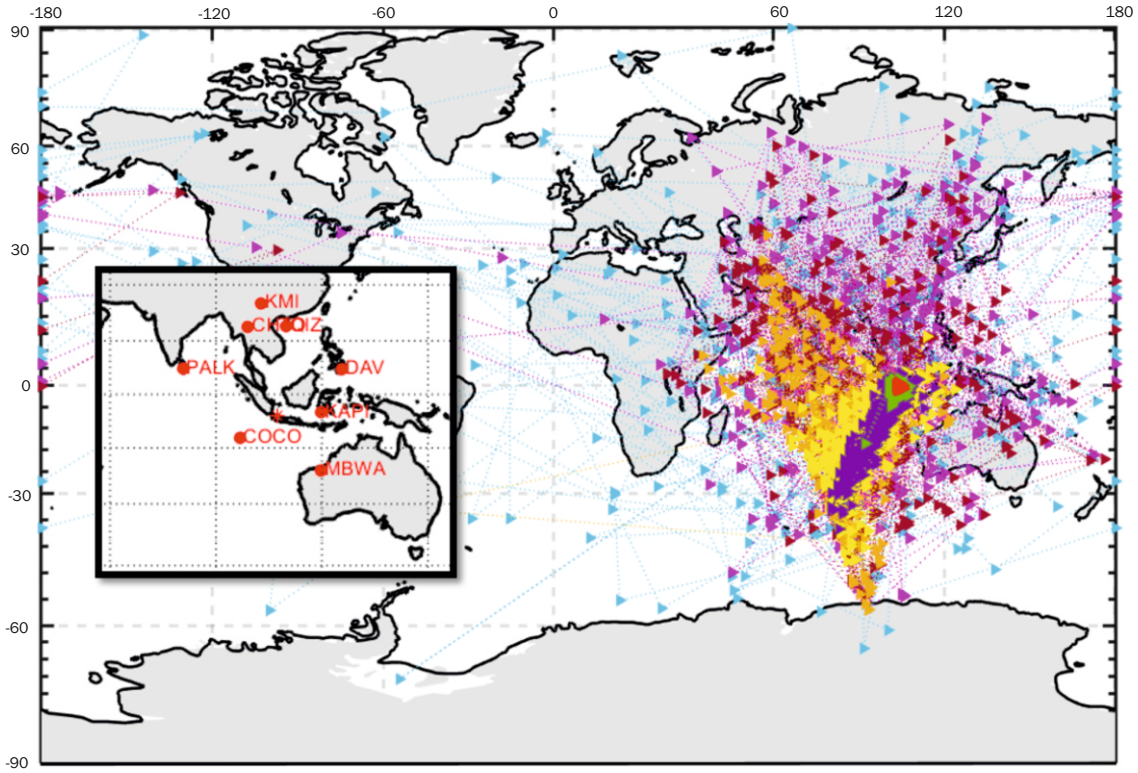


*Fig.2: Optimisation in 2D search space. Triangles with colours cyan, magenta, tamarillo, orange, yellow, indigo, green and red represent search points corresponding to generations 1, 2, 3, 5, 6, 7, 9 and 11 respectively.*

enough for those events that are well inside or very near to the network. For the events far outside the network, depth and origin time estimations are quite erroneous though the estimated latitude and longitude are reasonably good. This signifies that the events occurring inside the monitoring network are accurately located using this technique.

## Methods

For accurate estimation of location of seismic events using genetic algorithm, the design of fitness function (FF) plays a vital role. In this study it is formulated as

$$FF = \text{std}\left(t^{o}_{arrival} - t^{c}_{arrival}\right)$$

where std is standard deviation, $t^{o}_{arrival}$ is the arrival time of P waves observed at recording stations and $t^{c}_{arrival}$ is the calculated arrival times at those stations using the GA estimated locations parameters (i.e., latitude, longitude, depth and origin time) and 3D velocity model.

## Working of GA

The working of GA has been recounted in a flow chart as portrayed in Fig.1. GA actuates with the random initialization of a population which propagates itself through selected criteria and is changed by the application of well-developed genetic operators. The population consists of chromosomes and the number of chromosomes is called population size. A chromosome is a collection of bits representing the location parameters. The initial search domains for latitude, longitude, depth and origin time are -90° to 90°, -180° to 180°, 0 to 794 km and 30 minutes before the onset of the first coming P wave to the onset of the last coming P wave in a network respectively. These search spaces are typically represented by 8, 9, 10 and 11 bits respectively. So a chromosome is a bit-string of length 38 (8+9+10+11=38). The population size is mostly problem dependent. For the present study, it varies between 340 to 345 which are obtained on a trial basis. Thus, GA starts with a population that consists of 340 (say typically) chromosomes each 38-bit long. A single iteration of a genetic algorithm is based on three stages namely, selection (or replication), crossover (or recombination) and mutation. Selection begins with the evaluation of FF. For this, each chromosome is decoded to obtain the values of the location parameters. With knowledge of observed arrival times and

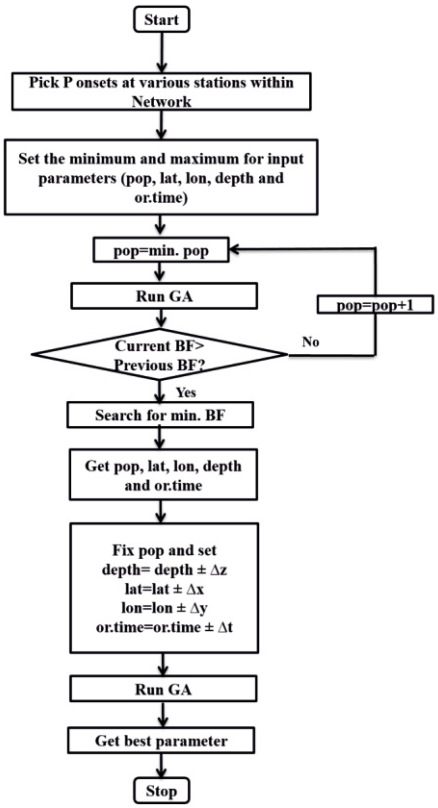


*Fig.3: Location estimation method. The parameters pop, min, BF, lat, lon, and or.time represent the population size, minimum, best fitness, latitude, longitude and origin time respectively. The step values Δx, Δy, Δz and Δt correspond to latitude, longitude, depth and origin time respectively.*

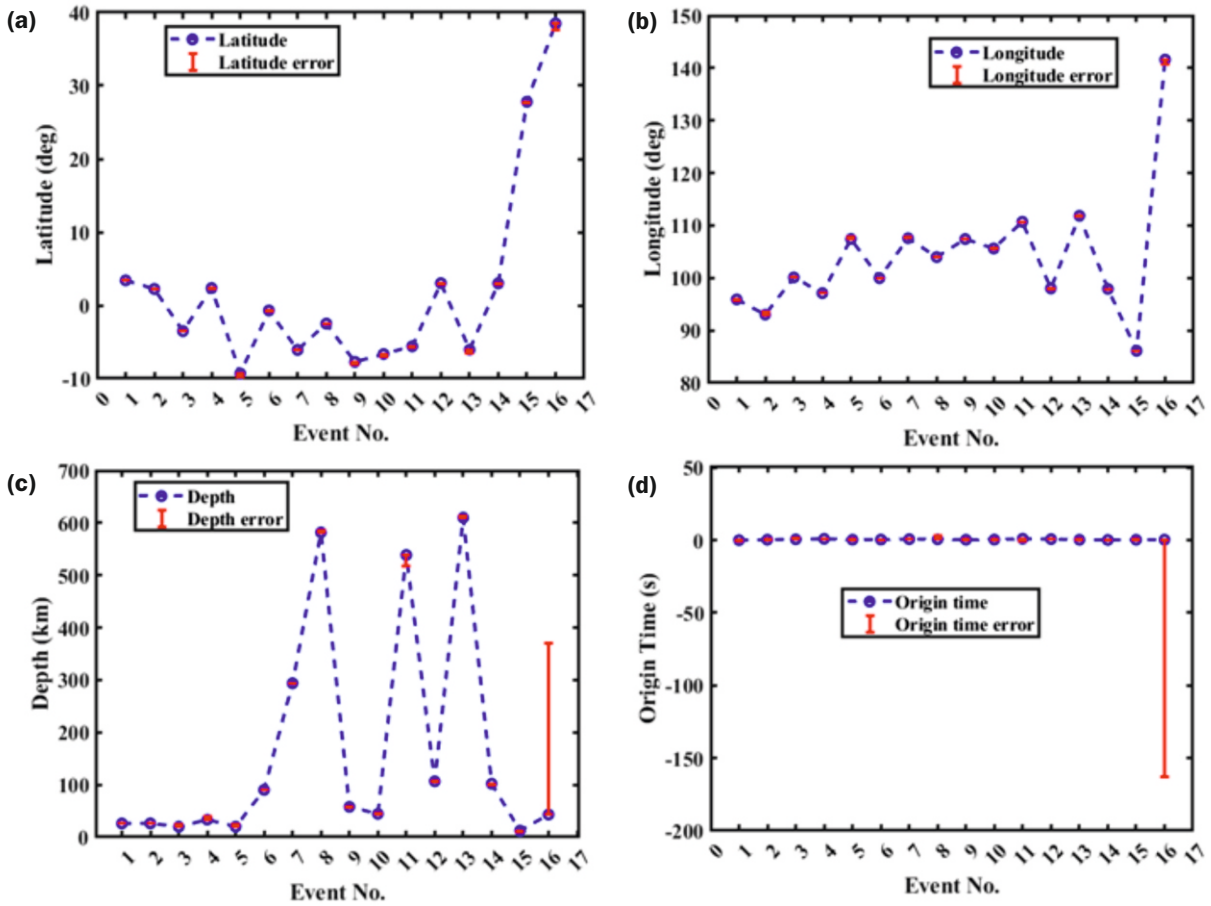


*Fig.4: Errors in latitude, longitude, depth and origin time estimation for 16 events are plotted in (a), (b), (c) and (d) respectively. Origin time has been normalized to unity. The positive and negative error barsindicate over-estimation and under-estimation respectively.*

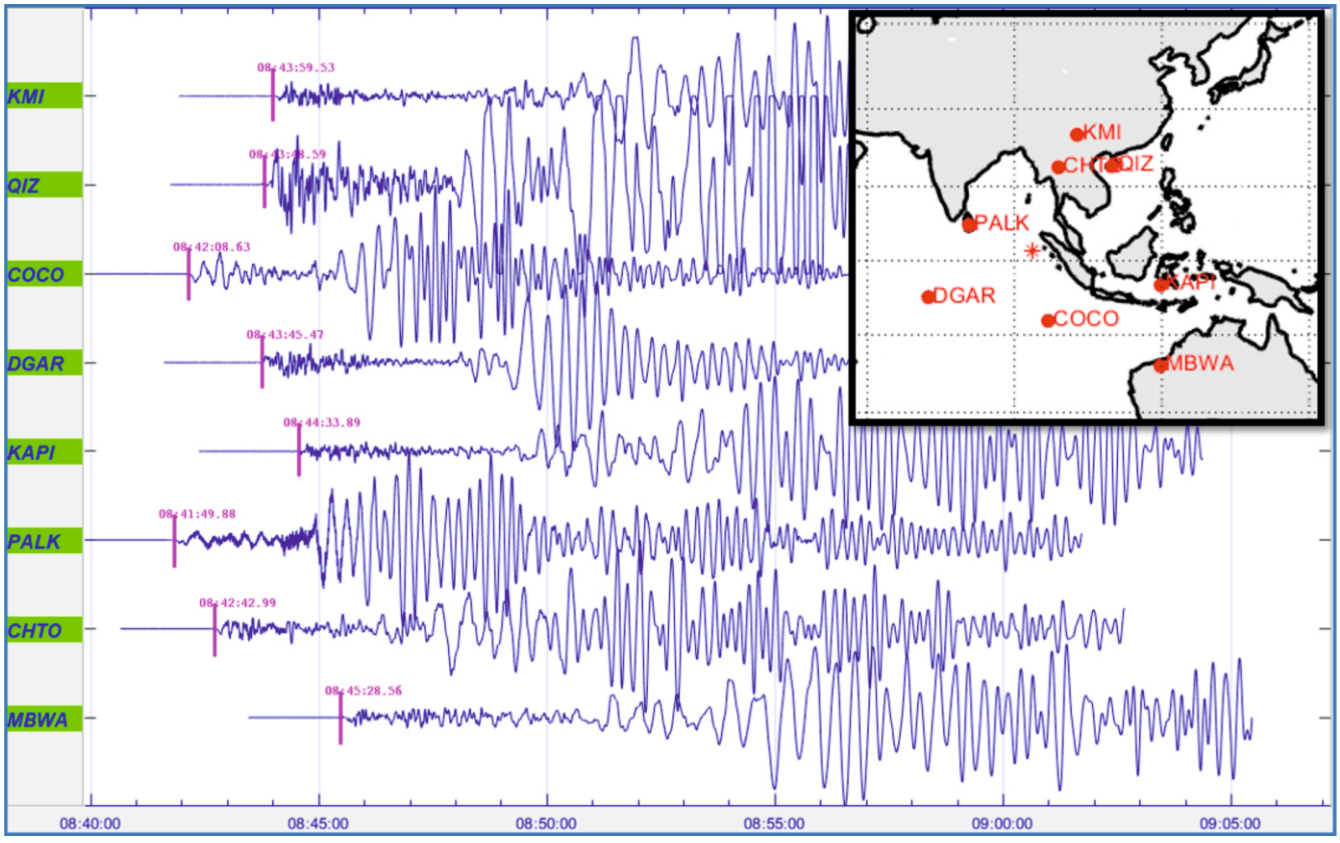


*Fig.5: Signal plots with marked P onsets and the network (shown in right corner panel).*

calculated arrival times (obtained using decoded location parameters and a 3D velocity model), FF is evaluated and assigned to each of the chromosomes in the population. The selection of best chromosomes can be done using a variety of selection algorithms such as roulette wheel, proportionate selection, linear rank selection, tournament selection and

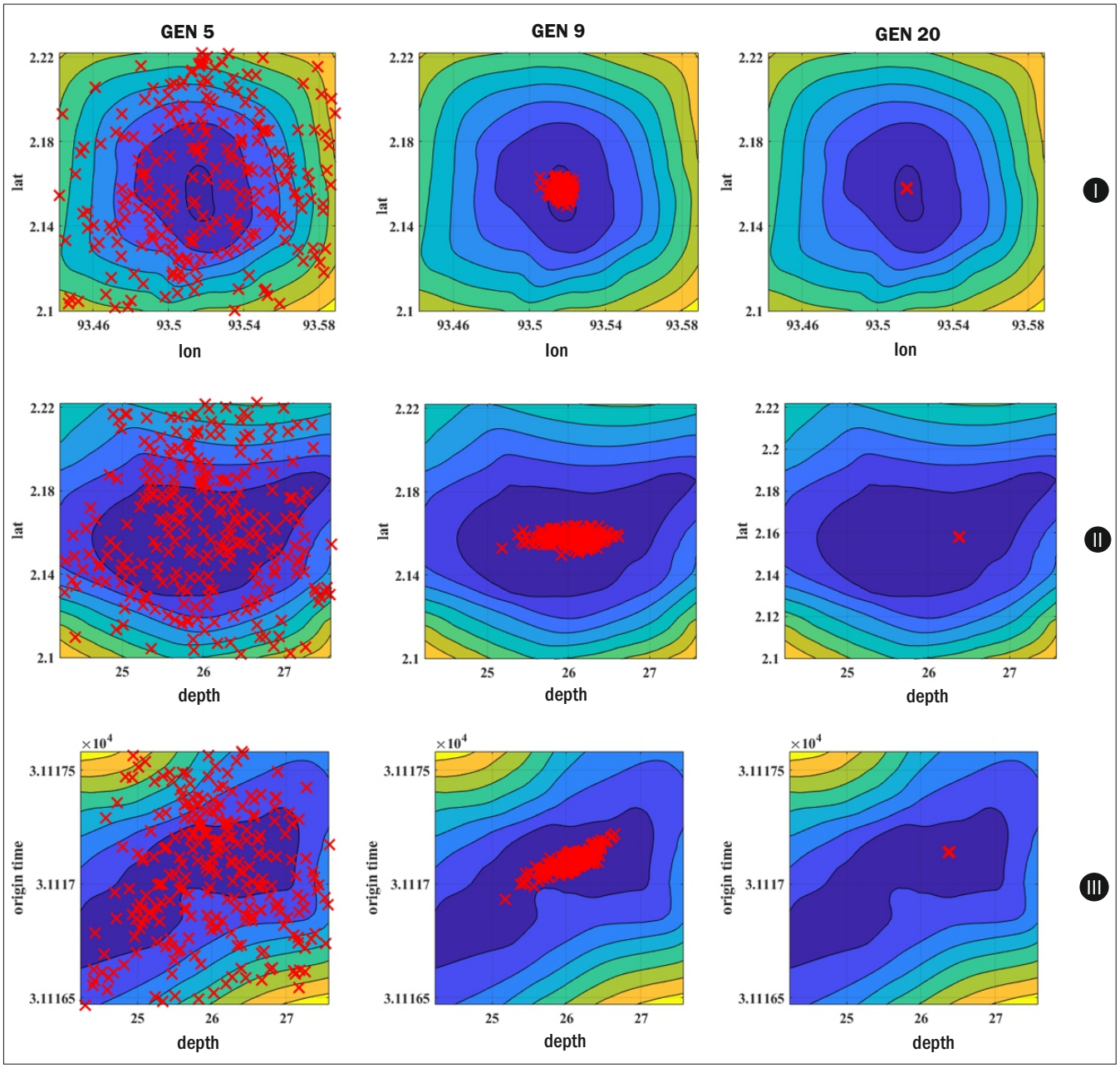


*Fig.6: Horizontal panels I, II and III correspond to search spaces latitude-longitude, latitude-depth and origin time-depth respectively for three generation stages (GEN= 5, 9 and 20).*

stochastic remainder selection [15]. For the present study, the most popular tournament selection algorithm has been used. The primary objective of the selection stage is to emphasize better chromosomes in a population. It does not create any new chromosomes; instead, it eliminates the bad chromosomes and selects relatively good chromosomes from a population and makes multiple copies of them. The creation of new chromosomes is performed by crossover and mutation. The crossover stage basically produces better off-springs. It selects two parents based on crossover probability and randomly picks a point (called crossover point) between two genes to slice each of the parent chromosomes into two parts. Then it combines the first part of the first parent and the second part of the second parent to get the first off spring Similarly, it combines the first part of the second parent and the second part of the first parent to get the second offspring. These off-springs will not be identical to any particular parent provided the parents are distinct but will instead combine the parental traits in a novel manner. The off-springs are expected to be better solutions (or chromosomes) as they are a result of the recombination of highly fit parents. It is noted that in the present study the crossover operation uses the intermediate crossover function with probability 0.95. However, every crossover may not create a better solution. Bad solutions, if created, are likely to get eliminated during the next selection process and good solutions are likely to get more chances to achieve a crossover with other good solutions in subsequent generations. Thus more and more solutions in the population are likely to have similar chromosomes. Crossover is used to create new solutions from the population's genetic information. However, these new solutions have no un-inherited or new inheritance information and the number of alleles (e.g., Blue eyes (eye colour), brown hair (hair colour)) is constantly decreasing. This process results in the contraction of the population to one point without searching the promising part of the search space and GA may get trapped in local minima. Whereas, the one goal of every learning algorithm is to search always in regions not viewed before. Therefore, it is necessary to enlarge the information contained in the population. This goal is achieved by using mutation. The

*Table 1: Event parameters as reported by IRIS along with the parameters estimated by GA.*

| Evt No. | Date | IRIS | | | | | GA | | | |
|---|---|---|---|---|---|---|---|---|---|---|
| | | Or. Time | Lat (deg) | Lon (deg) | Depth (km) | Mw | Or. Time | Lat (deg) | Lon (deg) | Depth (km) |
| 1 | 2004-12-26 | 00:58:52 | 3.4125 | 95.9012 | 26.1 | 9 | 00:58:51.44 | 3.421 | 95.681 | 25.97 |
| 2 | 2012-04-11 | 08:38:37 | 2.2376 | 93.0144 | 26.3 | 8.6 | 08:38:37.14 | 2.158 | 93.515 | 26.37 |
| 3 | 2010-10-25 | 14:42:22 | -3.5248 | 100.104 | 20 | 7.8 | 14:42:23.22 | -3.465 | 100.19 | 23.73 |
| 4 | 2010-04-06 | 22:15:02 | 2.3601 | 97.1113 | 33.4 | 7.8 | 22:15:01.63 | 2.276 | 97.075 | 39.78 |
| 5 | 2006-07-17 | 08:19:26 | -9.3178 | 107.424 | 20 | 7.7 | 08:19:26.71 | -9.77 | 107.86 | 24.21 |
| 6 | 2009-09-30 | 10:16:10 | -0.7071 | 99.9678 | 90.2 | 7.6 | 10:16:9.45 | -0.846 | 99.865 | 90.61 |
| 7 | 2007-08-08 | 17:04:58 | -6.089 | 107.584 | 293.8 | 7.5 | 17:04:58.22 | -6.071 | 107.79 | 292.69 |
| 8 | 2004-07-25 | 14:35:17 | -2.4931 | 103.975 | 581.9 | 7.3 | 14:35:19.61 | -2.489 | 104.05 | 585.43 |
| 9 | 2009-09-02 | 07:55:01 | -7.7346 | 107.411 | 57.8 | 7 | 07:55:01.19 | -8.002 | 107.39 | 56.99 |
| 10 | 2000-10-25 | 09:32:24 | -6.655 | 105.619 | 44.3 | 6.8 | 09:32:24.17 | -7.066 | 105.45 | 46.9 |
| 11 | 2020-07-06 | 22:54:47 | -5.5956 | 110.695 | 538.73 | 6.7 | 22:54:45.53 | -5.821 | 110.69 | 517 |
| 12 | 2011-09-05 | 17:55:12 | 3.0253 | 97.9991 | 106.6 | 6.7 | 17:55:12.31 | 2.781 | 97.904 | 108.02 |
| 13 | 2019-09-19 | 07:06:33 | -6.0708 | 111.842 | 610 | 6.1 | 07:06:33.66 | -6.589 | 111.7 | 613.61 |
| 14 | 2012-06-23 | 04:34:53 | 3.0022 | 97.9116 | 101.9 | 6.1 | 04:34:53.29 | 2.855 | 97.862 | 98.67 |
| 15 | 2015-05-12 | 07:05:18 | 27.802 | 86.126 | 12.3 | 7.2 | 07:05:18.35 | 27.576 | 86.168 | 10.062 |
| 16 | 2021-03-20 | 09:09:44 | 38.5 | 141.6 | 43 | 7 | 09:07:00.61 | 37.61 | 140.7 | 370 |

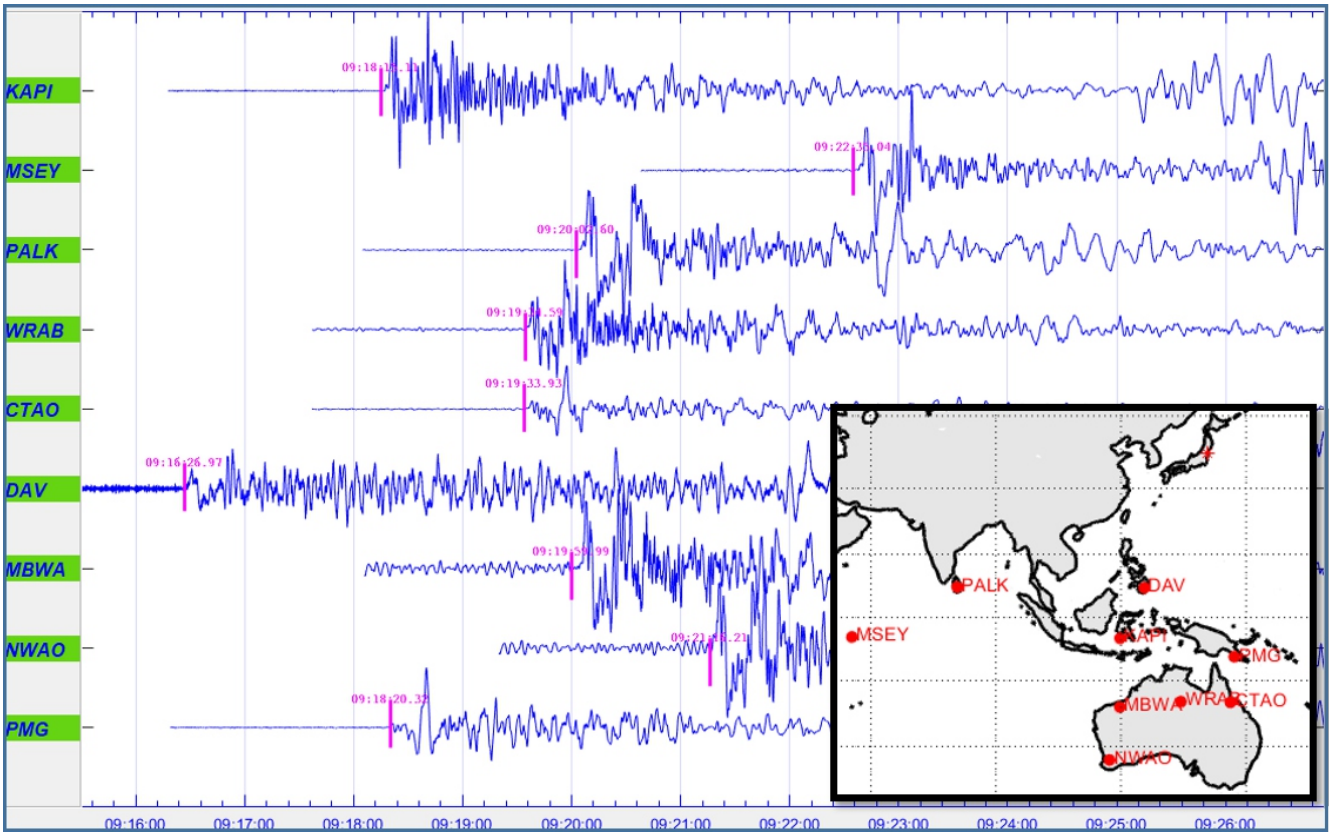


*Fig. 7: Signal plots with marked P onsets and the network (shown in right corner panel).*

mutation is carried out by flipping some bits of the chromosomes based on mutation probability. For the present study, the mutation operation makes use of the uniform mutation function with probability 0.002. It maintains the diversity of the population so that GA would not get trapped in partial solutions. The algorithm stops when stopping criteria (such as the number of generations reaches maximum generation) is met providing the best solutions i.e., the best estimates of location parameters.

To visualize the working of GA, a search space optimisation plot has been shown in Fig.2. To start with GA searches the whole space with search points indicated by the triangles with cyan colour. As the generations proceed the search space reduces and finally converge to a single point as shown by the triangle with red colour. The network chosen for this search space optimisation has been shown in the left panel of Fig.2. Using this optimisation capability of GA a method has proposed for earthquake location as described in the next section.

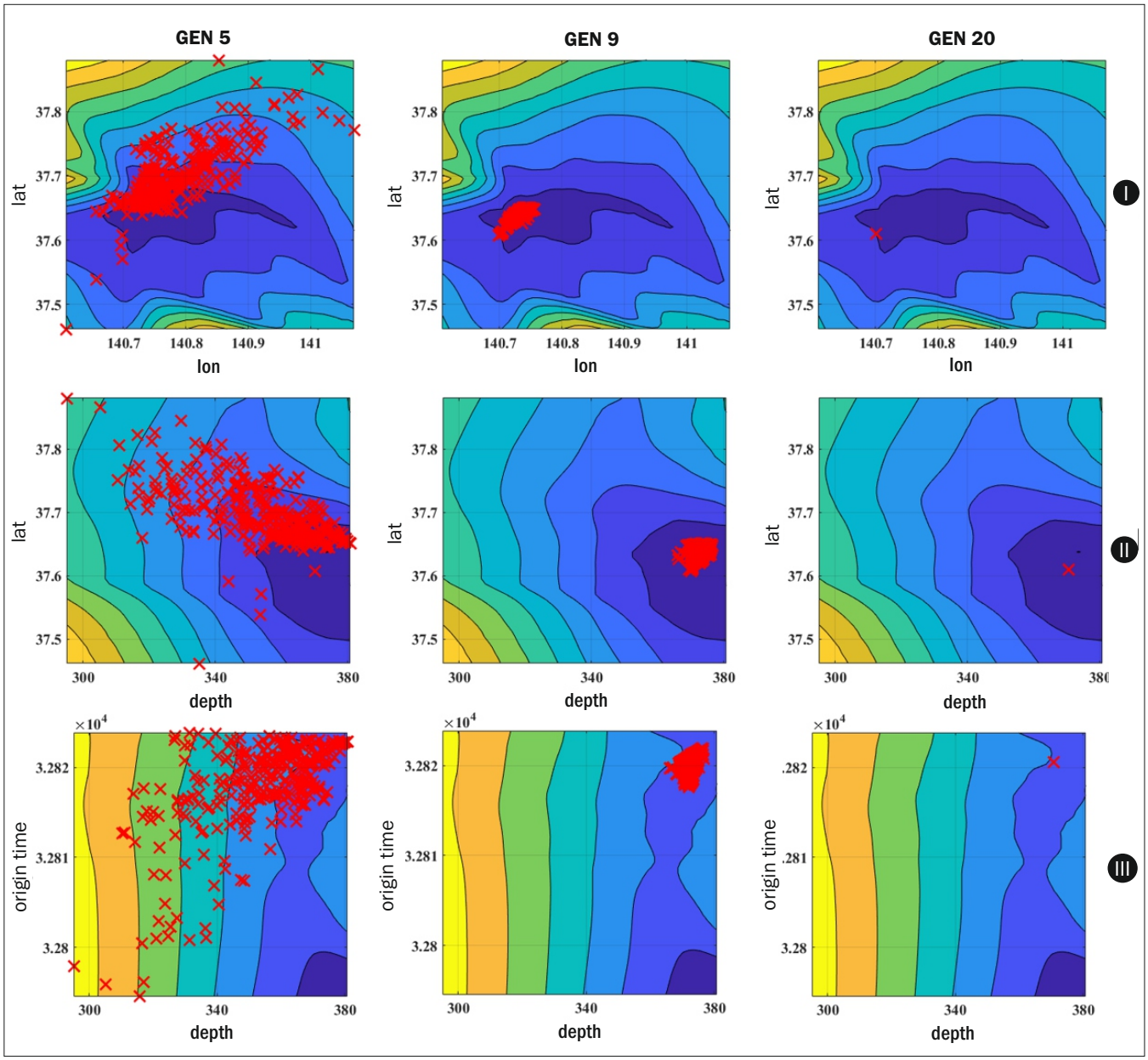


*Fig.8: Horizontal panels I, II and III correspond to search spaces latitude-longitude, latitude-depth and origin time-depth respectively for three generation stages (GEN= 5, 9 and 20).*

### Location estimation

The method of estimation of location has been shown in Fig.3. Initially, onsets of P waves recorded at various stations of a network are picked up. Then, the maximum and minimum ranges of the parameters to be estimated are assigned as mentioned in section 2.1. The range for population size has been considered from 340 to 345. Fixing the parameter ranges, GA is started with the lowest population size. The best fitness (BF) value of the fitness function for each step of the population loop is checked. If it is found that the BF value of the current step is greater than that of the previous step the loop is broken and the minimum value of BF is searched to find the optimum values for the parameters considered in the problem. Fixing the population size at optimum value, the latitude, longitude, depth and origin time are reset at latitude±Δx, longitude±Δy, depth±Δz and origin time±Δt where Δx, Δy, Δz and Δt may be typically taken as $3^0$, $3^0$, 20 km and 30 minutes respectively. With these new parameter settings, GA is again run to obtain the final estimates of the location parameters.

### Results

To study the efficacy of the algorithm we have downloaded the waveform data of 16 events that occurred in and outside the Sumatra region from IRIS (Incorporated Research Institutions for Seismology) website as given in Table 1. Out of 16, 14 data (Events 1 to 14) were from the Sumatra region. Event 15 was from Nepal and Event 16 was from Japan. The recording stations were selected such that the network formed by them well surrounds the first fourteen events. Event 15 was very near to the network whereas Event 16 was approximately $34^0$ away from the periphery of the network. All events were of magnitude (Mw) greater than 6 and depths ranging from 12.3 km to 581.9 km. The location parameters of these events as estimated by GA are also noted in Table 1. The errors involved in the estimation of location parameters are shown in Fig.4. It is observed that the first 15 events are almost accurately located by GA. These events are located inside the network except Event 15 which reclines outside the network but very near the boundary of the network. For event 16, though the latitude and longitude estimates are

reasonable, the depth and origin time estimates are very poor as seen in Fig.4(c) and (d). The reason is that this particular event is very far away from the network for which GA fails to minimize the fitness function reasonably. To visualize GA estimation in search space two events namely, event 2 (well inside the network) and event 16 (far away from the network) have been considered as a case study and are discussed below in detail.

***Case study 1: Event inside the network (Event 2)***

The recording network as well as the recorded signals with P onset marking has been shown in Fig.5. The optimization in the search spaces like latitude-longitude, latitude-depth and origin time-depth has been shown through contour plots for generations 5, 9 and 20 respectively in Fig.6. The figure clearly shows that at generation 20 all the search space converges to a single point almost at the middle of the contour leading to an accurate estimate of location parameters. A similar picture has been obtained for all events lying inside or near the boundary of the network.

***Case 2: Event outside the network (Event 16)***

The recording network and the recorded signals with P onset marking have been shown in Fig.7. The optimization in the search spaces, namely, latitude-longitude, latitude-depth and origin time-depth has been shown through contour plots for generations 5, 9 and 20 respectively in Fig.8. For this event, though the spread of the search space reduces to a point at generation 20 but not at the centre of the contour, especially in the origin time-depth space leading to poor estimates of depth and origin time. The reason behind this is that event 16 is remotely located from the network.

## Conclusions

The present study takes the advantage of GA in estimating the location parameters. The advantage of GA for earthquake location is that they do not require derivative information and still have both a local and global search character. The study shows that for all the events located inside or near the boundary of the monitoring network, the location estimates are reasonably accurate whereas, for the event lying far outside the network, location estimates especially depth and origin time become erroneous. Thus we strongly believe that GA is a powerful tool for performing robust earthquake locations provided the monitoring region is well surrounded by recording instruments.

## Acknowledgements

Authors are thankful to Incorporated Research Institutions for Seismology (IRIS) for their open source GSN data, which was employed in this study. Authors would like to thank Dr. S. Mukhopadhyay, Shri A. Vijaya Kumar, Shri Ashish Gupta and Shri Abin C. Joy for the useful discussions. Authors also thank the reviewer for his valuable suggestions.

## References

[1] Milne, J.: Earthquakes and Other Earth Movements. Appelton, New York (1986)

[2] Reid, H.: The Mechanics of the Earthquake, Vol. II of The California Earthquake of April 18, 1906 (1910)

[3] Geiger, L.: Probability method for the determination of earthquake epicenters from the arrival time only. Bull. St. Louis. Univ 8, 60–71 (1912).

[4] Karasözen E, Karasözen B. Earthquake location methods. GEM-International Journal on Geomathematics. 2020 Dec;11(1):1-28.

[5] Klein, F.: User's guide to HYPOINVERSE–2000, a Fortran program to solve for earthquake locations and magnitudes (2002)

[6] Lee, W., Lahr, J.: HYPO71, a computer program for determining hypocenter, magnitude and first motion pattern of local earthquakes (1972)

[7] Lin, G., Shearer, P.: The COMPLOC earthquake location package. Seismol. Res. Lett. 77(4), 440–444 (2006). https://doi.org/10.1785/gssrl.77.4.440

[8] Lienert, B., Berg, E., Frazer, N.: "hypocenter": an earthquake location method using centred, scaled and adaptively damped least squares. Bull. Seismol. Soc. Am. 76, 771–783 (1986)

[9] Pavlis, G.L., Vernon, F., Harvey, D., Quinlan, D.: The generalized earthquake-location GENLOC package: an earthquake-location library. Comput. Geosci. 30(9), 1079–1091 (2004). https://doi.org/10.1016/j.cageo.2004.06.010

[10] Schweitzer, J.: HYPOSAT—an enhanced routine to locate seismic events. Pure Appl. Geophys. 158(1), 277–289 (2001)

[11] Douglas, A.: Joint epicentre determination. Nature 215, 47–48 (1967)

[12] Dewey, J.W.: Seismic studies with the method of joint hypocenter determination. Ph.D. thesis, University of California (1971)

[13] Pujol, J.: Joint event location—the JHD technique and applications to data from local seismic networks. In: Thurber, C.H., Rabinowitz, N. (eds.) Advances in Seismic Event Location, pp. 163–204. Springer, Dordrecht (2000). https://doi.org/10.1007/978-94-015-9536-0_7

[14] Holland, J. H. (1975). Adaption in Natural and Artificial Systems, The University of Michigan Press, Ann Arbor.

[15] Chaturvedi DK. Soft computing. Studies in Computational intelligence. 2008;103:363-381.

# Fluorescence based Sensors for Heparin

## ▪ A widely used blood anticoagulant

Prabhat K. Singh

Heparin is one of the most widely used blood anti-coagulant and an antithrombotic drug. Heparin treatment is required to maintain blood fluidity, and to prevent blood clot formation during major surgical procedures that require extracorporeal circulation, for example, hemodialysis or cardio-pulmonary bypass surgeries. Considering the raising instances of cardiovascular diseases and the maturing population, an estimated one billion doses of Heparin are produced every year. This has led to a rapid increase in the development of Heparin market. Heparin is generally administered in ranges of 1.7–10μM (0.2–1.2 U/mL) for long-term post-operative care and 17–67μM (2–8 U/mL) during cardiovascular surgery. However, Heparin overdose can lead to serious adverse effects, such as, Heparin-induced thrombocytopenia, hemorrhages, osteoporosis and hyperkalemia. Thus, it is vital to detect and control the Heparin level and its activity during and after surgery, and to manipulate the amount of Heparin used for anticoagulation therapy.

We have developed a fluorescence-based sensor for Heparin detection where we have utilized a tetraphenylethylene derived AIEgen, named tetrapyridinium-tetraphenylethylene (TPy-TPE), for sensing Heparin. TPy-TPE carries four positive charges and forms aggregates in presence of negatively charged Heparin to form highly emissive aggregates of TPy-TPE (Scheme 1). Most importantly, the tetracationic nature of TPy-TPE provides a stronger binding affinity towards Heparin compared to the previously reported monocationic or dicationic fluorophores. The improved interaction between Heparin and TPy-TPE has proved to be advantageous in terms of improved sensitivity (lower LODs in aqueous and serum samples), higher fluorescence enhancement and better performance in complex matrices. While TPy-TPE is utilized for Heparin determination, its sole U.S. Food and Drug Administration (FDA) authorized antidote, Protamine, and Heparinase, which specifically degrades Heparin to produce clinically important Low Molecular Weight Heparin (LMWH) have also been detected through our probe molecule. Overall, the photophysical investigation for the detection of Heparin is a successful attempt and is expected to enhance Heparin related biosensing research in the biomedical fields.

In another contribution, we report a naked-eye detection of Heparin in aqueous and in complex human plasma samples by using a cyanine based probe, TO-PRO-3, which records a huge blue shift (~115 nm) in its absorption maximum, and marks the highest reported absorption spectral shift for any Heparin sensing system, known till date leading to visual detection of Heparin (Scheme 2). The probe has been also shown to be useful for sensing the only clinically approved Heparin antidote, Protamine as well as a Heparin degrading enzyme, Heparinase, which serves as an important biomarker for inflammation. Overall, we have been able to develop a very simple, highly sensitive and selective assay for a widely used blood anti-coagulant drug, Heparin, which can even perform well in complex bio-samples and promises potential applications in real life scenario and Heparin related biochemical research.

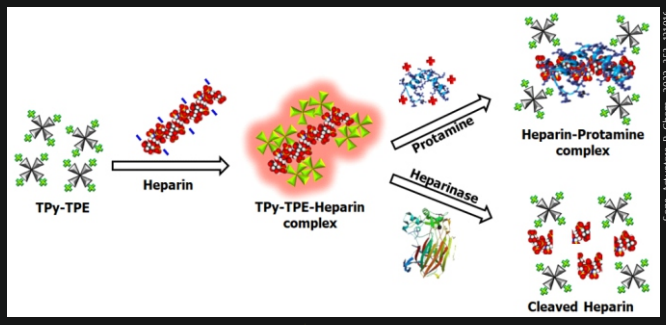


Sens. Actuators, B: Chem., 2022, 353, 131016

▲ Scheme 1: Schematic representation of Fluorescence turn-on detection of Heparin.

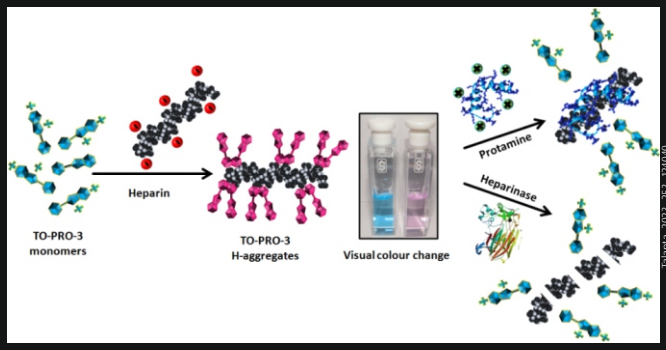


Talanta, 2023, 253, 124040

▲ Scheme 2: Schematic representation of visual detection of Heparin.

The author is a Professor of Homi Bhabha National Institute situated in Mumbai.

Dr. Prabhat K. Singh, is currently working as a Scientific Officer/G at Radiation and Photochemistry Division, Bhabha Atomic Research Centre (BARC), Mumbai, India. His current research interest includes ultrafast spectroscopy, supramolecular chemistry and use of self-assembled materials for designing optical sensors for bio-sensing and chemo-sensing applications. Prof. Singh has authored about 115 publications in peer-reviewed international journals. He is a recipient of young scientist award of Department of Atomic Energy, Indian Science Congress Association (ISCA) and National Academy of Science, India (NASI). In recognition of his work, he was selected as a Member of Indian National Young Academy of Sciences (INYAS), and National Academy of Sciences, India (NASI) recently. Prof. Singh is also a member of prestigious Global Young Academy, Berlin, Germany.


**Santoshi Prabhu** (*Consultant, BARC Hospital, Mumbai*)
santoshi@barc.gov.in
**Nigamananda Mishra** (*Head, Department of Obstetrics and Gynaecology, BARC Hospital, Mumbai*)
mishran@barc.gov.in

The World Health Organization (WHO) considers Infertility as a 'disease of human reproductive system'. Around 186 million individuals are affected due to infertility globally with an impact on their personal and social life. Depending on whether pregnancy has been attained in the past, infertility can be considered Primary Infertility i.e. when a pregnancy has never been achieved or secondary infertility- when at least one prior pregnancy has been achieved.

Ideal fertility care should comprise of prevention, diagnosis and treatment of infertility. Due to cost involved, fertility care is rarely given priority in national universal health coverage benefit packages. In May 2014, considering the high cost involved in advanced Assisted Reproductive Technology (ART) treatment: In-vitro fertilization (IVF); the Contributory Health Services Scheme (CHSS) permitted reimbursement of expenses to a great extent to infertile couples in whom conventional treatment had failed. This conventional treatment in many cases includes least invasive, effective, simple relatively cheap first line basic ART procedures like Intra-uterine insemination (IUI).

Although the Department of Gynaecology at BARC Hospital, provided preventive and diagnostic measures including treatments like ovulation induction, the facility of basic ART procedure of IUI was not available in-house. As a result, many patients had to undergo multiple cycles of IUI at their own expense. To prevent direct referral to high cost advance procedure of IVF, bypassing the adequate trial of basic IUI procedures and prior to labelling a case as clear failure to conventional treatment it was essential to provide this dedicated ART facility with in-house IUI services. Hence, in July 2017, the Fertility Clinic was inaugurated at BARC Hospital.

The clinic has been approved for all ART procedures under PCPNDT act by the Government of Maharashtra. At present, IUI procedures are performed at this clinic. IUI is an OPD procedure which does not need anaesthesia.

In patient selection criteria for IUI, patent fallopian tube and presumptive proof of ovulation is mandatory with other indications being mild male factor, cervical factor, immunological factor or unexplained infertility. Ovulation is induced to time ovulation and follicular monitoring is performed to assess the response. Injection hCG 10,000 International Units (IU) is given once follicular size is at least 18 mm in diameter and endometrial thickness is more than 6 mm. IUI is usually timed 36 to 40 hours post hCG administration.

Normally, semen contains spermatozoa in seminal plasma. Seminal plasma leads to reduction in sperm motility. Semen needs to be processed prior to IUI so as to remove decapacitating factors, reduce concentration of reactive oxygen species, remove leukocytes and immature sperms which account for cytotoxic factors. The aim of sperm preparation is to isolate sperm fraction that contains highly motile, mostly morphologically normal sperms free of other debris and cells.

IUI is the procedure of deposition of this processed sperm isolate, directly in to the uterus at the anticipated time of ovulation. The rationale of IUI is to expose oocyte to more sperms near the site of fertilization and improve chances of conception.

The Fertility Clinic is equipped with a consulting room, semen collection room, semen processing laboratory (IUI lab) and a dedicated IUI room for performing procedures under aseptic precautions.

**Consulting room:** The room has privacy for interviewing and examining the couple. It is computerized for maintaining records of investigations, treatment and procedure details. Facility for follicular monitoring prior to and after ovulation induction is available in the consulting room. The procedure of IUI is performed in this consulting room.

**Semen collection:** Considering the psychological stress at the time of semen collection, a dedicated room has been established which ensures enough privacy and an appropriate environment where the husbands come only after a prior appointment. It is located close to IUI lab and has attached wash basin and washroom facility. For the procedure of semen collection a sterile, wide mouthed, non-toxic and disposable container is provided in the clinic.

**IUI lab:** A sterile area is necessary for semen processing close to semen collection room and consulting room where the actual insemination procedure is performed. Ultraviolet light is used to create a sterile area in the laboratory.

Good laboratory practice (GLP) guidelines as described internationally along with safe disposal of biological waste are strictly followed in the laboratory. The equipments include phase contrast microscope, test tube warmer, centrifuge machine, stainless steel top workstation with sterile laminar flow hood and a refrigerator.

Semen analysis is performed using phase contrast microscope, which has 10x, 20x, 40x and 100x objectives. Semen is examined for count, motility, morphology and other components such as pus cells. Although expensive, a very accurate Makler Counting Chamber is used for this purpose.

A stainless-steel top workstation equipped with sterile laminar flow hood is used to effectively minimise contamination at the process of sperm preparation.

The data obtained till December 2021 shows that 528 patients were registered at fertility clinic, 4269 follicular studies were done and 559 IUI cycles were performed with success rate of 16.24%. M. Schorsch et al analyzed 4246 inseminations cycles and reported overall pregnancy rate between 7.5 and 10% in women aged up to 40 years, even with several insemination cycles [1]. Success of IUI program of fertility clinic goes to expertise, clean environment, proper instruments, disposables, media, standard protocols and strict quality control. The clinic aims to provide more advanced ART treatment in future.

## Reference

[1] Schorsch M., Gomez R., Hahn T., Hoelscher-Obermaier J., Seufert R., Skala C. Success Rate of Inseminations Dependent on Maternal Age? An Analysis of 4246 Insemination Cycles. Geburtshilfe Frauenheilkd. 2013 Aug; 73(8):808-811. doi: 10.1055/s-0033-1350615. PMID: 24771935; PMCID: PMC3859121.

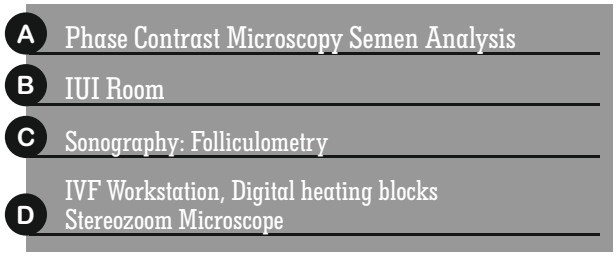

trombay colloquium*
June 12 • 2023

# Energy Management
## Indian Perspectives

India, growing exponentially in science, technology and innovation, has thoughtfully coined the theme of the G20 Presidency as One Earth, One Family, One Future. Energy management in India includes efforts to generate, convert and effectively store usable forms of energy. An "Energy Mix" comprising both conventional and renewable energies in a practically realisable ratio has to be maintained for a balanced life.

**Dr. N. Kalaiselvi**
**Director General, CSIR**
**and Secretary, DSIR**
**Government of India**

*The Trombay Colloquium is a key window of opportunity for the BARC community to brainstorm with eminent individuals belonging to a wide spectrum of science and allied domains. Prominent scientists and technologists are invited to BARC Trombay to deliver captivating talks on emerging domains of science, and the transformative effect of new technological innovations.


Photo courtesy of Doordarshan, Ministry of Information and Broadcasting, Govt. of India.

# Govt. of India inaugurates new facilities of DAE

**SIRD Editorial Team**
Bhabha Atomic Research Centre, Trombay - 400 085, India

The National Technology Day is celebrated each year on May 11th to mark the country's successful nuclear experiments in Pokhran during the year 1998.

Importantly, the year 2023 marks the completion of 25 years of this unique national achievement.

On this occasion, the Prime Minister of India laid the foundation stone and dedicated to the nation multiple projects worth more than Rs 5800 crore related to scientific and technological advancement in the country.


*First Day cover released during NTD 2023 event marking completion of 25 years of Operation Shakti.*

The facilities of Department of Atomic Energy (DAE) dedicated to the nation at the Technology Day event-2023 include Fission Molybdenum-99 Production Facility, Mumbai; Rare Earth Permanent Magnet Plant, Visakhapatnam; National Hadron Beam Therapy Facility, Navi Mumbai; Radiological Research Unit, Navi Mumbai; Homi Bhabha Cancer Hospital and Research Centre, Visakhapatnam; and Women & Children Cancer Hospital Building, Navi Mumbai.

Besides these, the Govt. of India also laid the foundation stone remotely for various pan-India facilities, including Homi Bhabha Cancer Hospital in Odisha's Khurda district; Laser Interferometer Gravitational wave observatories at Hingoli in Maharashtra as part of LIGO-India project; Platinum Jubilee Block of Tata Memorial Hospital at Parel in Mumbai.

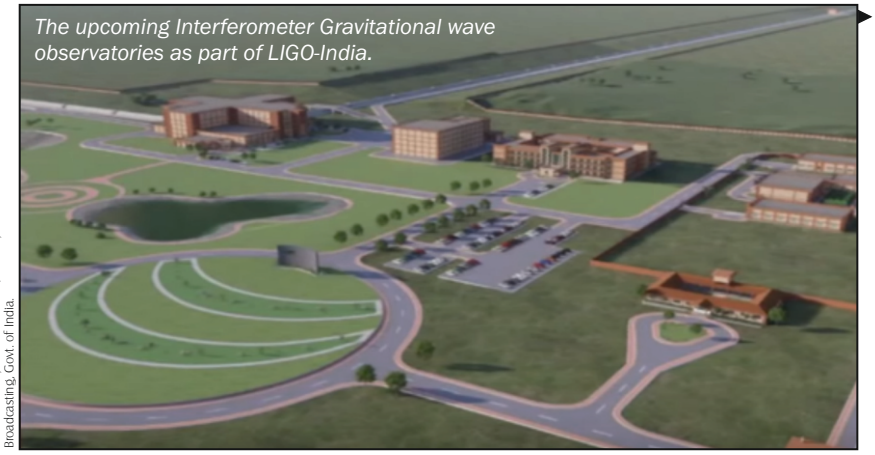

*The upcoming Interferometer Gravitational wave observatories as part of LIGO-India.*

Photo courtesy of Doordarshan, Ministry of Information and Broadcasting, Govt. of India.

**LIGO-India**, to be developed in Hingoli, Maharashtra, will be one of the handful Laser Interferometer Gravitational wave observatories in the world. It is an extremely sensitive interferometer of 4 km arm length capable of sensing gravitational waves generated during the merger of massive astrophysical objects such as black holes, and neutron stars. The LIGO-India will work in synchronization with two observatories operating in the United States - one in Hanford, Washington and the other in Livingston, Louisiana.

**Rare Earth Permanent Magnets** are produced primarily in developed countries. The facility for the production of the Rare Earth Permanent Magnet has been developed in Bhabha Atomic Research Centre at Visakhapatnam. The facility has been established based on indigenous technology and using indigenous Rare Earth material extracted from indigenous resources. With this facility, India will join a select group of nations with the capacity to produce Rare Earth Permanent Magnets.

*Bird's eye view of Rare Earth Permanent Magnets production facility of BARC Visakhpatnam.*

Photo courtesy of Doordarshan, Ministry of Information and Broadcasting, Govt. of India.


*The National Hadron Beam (Proton) Therapy Facility of Tata Memorial Centre, Navi Mumbai.*

Photo courtesy of Doordarshan, Ministry of Information and Broadcasting, Govt. of India.

**The National Hadron Beam (Proton) Therapy Facility** of Tata Memorial Centre, Navi Mumbai is a state-of-the-art facility which works to undertake highly precise delivery of radiation to the tumour with minimal dose to the surrounding normal structures. The precise delivery of dose to target tissue reduces the early and delayed side effects of radiation therapy.

**The Fission Molybdenum-99 Production Facility** is situated in BARC Trombay. Molybdenum-99 is the parent of Technetium-99m, which is used in more than 85% of imaging procedures for the early detection of cancer, heart disease etc. The facility is expected to enable about 9 to 10 lakh patient scans per year. The laying of the foundation stone and dedication of several Cancer Hospitals and facilities will decentralize and enhance the provisioning of world-class cancer care in different regions of the country.

*DAE facility for processing of Fission Molybdenum-99.*

Photo courtesy of Doordarshan, Ministry of Information and Broadcasting, Govt. of India.

## Reports from conferences, theme meetings and workshops

# PCSE-2023

# National Workshop on

## *Parallel Computing in Science and Engineering*

A one-day national workshop entitled *"Parallel Computing in Science and Engineering (PCSE-2023)* was organized at Multipurpose Hall, TSH, BARC, Mumbai on April, 19, 2023. The workshop was organized by Chemical Engineering Division, Computer Division and Computational Analysis Division, BARC in association with Board of Research in Nuclear Sciences, Department of Atomic Energy.

Dr. S. Mukhopadhyay, Director, E&IG, BARC, and Chairman (PCSE '23), delivered the welcome address of the workshop. In his inaugural speech, chief guest Dr. A. K. Mohanty, Director, BARC advocated the needs of high performance computing, comprising mainly of CPU-GPU based Parallel Computing and Quantum Computing for solving complex domain problems. He further emphasized on the need for a strong collaboration between the community of users and developers of high performance computers in science and engineering in their efforts for developing an in-house 'Exascale' computational facility. The proceedings of the workshop was released by Director, BARC. The vote of thanks was delivered by Dr. Sk. Musharaf Ali, Head, AMCAS, ChED, and Convener (PCSE '23). About 135 delegates from DAE and non-DAE institutes participated in the workshop. Total 9 invited lectures at the workshop covered various aspects of Parallel Computing and Quantum Computing, including application of computational power at the Petaflop and Exaflop scale for use in physics, chemistry, biology and engineering.

Experts from various institutes such as IPR, CDAC-Pune, and BARC covered various aspects in their presentations at the workshop. In the concluding session, Shri K. Rajesh, Head, Computer Division summarized briefly all lectures covered in the workshop; and Shri K. T. Shenoy, Director, Chemical Engineering Group, BARC spoke on the collaboration between the supercomputing facility team and users for addressing real-time chemical engineering problems in the department.

Main Photograph: Senior officials of BARC, IPR and workshop participants pose for a group photo on the sidelines of one-day national workshop on Parallel Computing in Science and Engineering (PSCE-2023).
Inset photograph caption: Dr. A.K. Mohanty (centre) releasing the proceedings of workshop during the program's inaugural session.

**Reports from conferences, theme meetings and workshops**


# Symposium on
## *Advancements & Innovations in Hot Cell Systems*

The Nuclear Recycle Group of Bhabha Atomic Research Centre (BARC) has recently organized a three-day symposium to discuss and showcase new "advancements and innovations in technologies for hot cell engineering systems of nuclear facilities". The 'HOTCELLTECH-2023' symposium during 25-27 May, 2023 saw participation of more than 275 delegates from DAE bodies and Industry.

The BRNS-sponsored symposium' included an inaugural session, nine technical sessions and a concluding session. This symposium witnessed wholesome participation from domain experts from BARC, IGCAR, BRIT and Industry partners. The scientific and technical aspects of hotcell technologies were covered in the form of 34 technical paper presentations during the symposium. These presentations, covered topics including hot cell engineering and remotization, challenges and innovations in Master-Slave manupulators, radiation shielding window glass technology, post irradiation examination of fuels etc. The contributory papers were compiled together and published in the proceedings during the inaugural session.

The keynote address of the event was delivered by chief guest Shri B. C. Pathak, Chairman & Managing Director of NPCIL. Shri Vivek Bhasin, Director of NFG and RD&DG addressed the gathering present during the inaugural session of the symposium through his introductory remarks. Smt. S. Manohar, Director, NRG delivered the welcome address. Shri Y. C. Shivakumar, Head, TDD, NRG, and Convenor of the symposium presented the vote of thanks (inaugural session) followed by concluding remarks by Shri P. D. Maniyar, Convenor of the Symposium Technical Committee.

Participants of HOTCELLTECH-2023 symposium pose for group photo. Inset (From left to right): Smt. Smita Manohar, Director, NRG, Shri Vivek Bhasin, Director, NFG, program chief guest Shri B. C. Pathak, and Shri Y. C. Shivakumar releasing a volume with information on proceedings of the symposium.

## Reports from conferences, theme meetings and workshops


Dr. R. Chidambaram, Former Chairman AEC (in brown jacket) and senior officials of BARC releasing the abstract book during the inaugural session of HV-ESCA 2023 at DAE Convention Centre in Anushaktinagar.

# HV-ESCA 2023

# National Symposium on

## *High Voltage - Energy Storage Capacitors & Applications*

A national symposium *High Voltage - Energy Storage Capacitors and its Applications (HV-ESCA-2023)* was organized by Beam Technology Development Group and Electronics & Instrumentation Group, BARC during June 22-24, 2023 at DAE convention Centre in Anushaktinagar, Mumbai. The symposium was sponsored by BRNS and the Power Beam Society of India assisted the organizers in planning the symposium.

From the total 110 contributory papers/abstracts received for the symposium, 104 papers were accepted for oral/poster presentation. The symposium covered three keynote lectures and 13 invited talks by Professors from IITs/IISc, senior scientists from DAE & DRDO as well as experts from industry.

The technical papers identified for discussion at the symposium were featured in an abstract book, which was unveiled by program chief guest Dr. R. Chidambaram, Former Chairman, AEC during the inaugural session.

The three keynote lectures delivered in the plenary session of the symposium are: *A Glimpse into 40 years of Life in Pulsed Power Technology* by Shri G. P. Srivastava, Former Director, E&IG and CMD, ECIL; *High Power Electromagnetic Environment, Interaction, Coupling, Effects & Mitigation* by Dr. D. C. Pande, LRDE, DRDO; and *Evolution of Pulsed Power in BARC* by Dr. K. C. Mittal, Former Head, APPD, BARC.

A technical visit to high-voltage facilities at Hall-9 & Hall-4 in BARC was arranged for the benefit of symposium participants by BTDG and E&IG. An exhibition was set up at the symposium venue to showcase BARC technologies in the domain of High Voltage - Energy Storage Capacitors. It was inaugurated by Dr. Jayakumar, Controller, BARC.

The Guest of Honour, Shri Clement Verghese, Chairman, BARC Safety Council, handed over awards and certificates of appreciation to the meritorious candidates. Two best oral presentations and 13 best posters were selected.

Dr. P. H. Ron, Former Head, APPD, BTDG, BARC graced the event as the chief guest of the valedictory function on 24th of June during which, he released a book on Pulsed Power and Applications edited by Dr. R. I. Bakhtsingh and Dr. Archana Sharma of BTDG and published by Scientific Information Resource Division, BARC.

The proceedings of the symposium were uploaded online in PSI website (www.powerbeamsociety.in).

**Symposium topics**

- Pulsed power generators
- Recent Trends in dielectric materials
- High current and high energy capacitor banks
- Upcoming topologies & control in power Modules
- Neutron and X-ray generators
- Electron beam accelerators and applications
- Rail and coil gun technology
- Electromagnetic welding
- New developments in high voltage switches
- Trending applications of pulsed power
- High voltage safety and standards
- EMI &EMC


Dr. P. H. Ron (third from left), Former Head, APPD and senior officials of E&IG, BSC and BTDG releasing a book on Pulsed Technology Development in BARC during the symposium valedictory function.

# OBITUARY

## Dr. S. K. Sikka

# A doyen of high pressure physics in India

*Dr. S. K. Sikka receiving the Lifetime Achievement Award from Former Prime Minister of India.*

We are deeply saddened by the news of passing away of one of our dearest and esteemed colleagues, Dr. S. K. Sikka. His sudden demise ended our long and close association with him for almost five decades. During this period, we have known him as a prolific scientist as well as a caring colleague. Dr. Sikka's early contributions to the 'phase problem' in neutron crystallography had been accepted as teaching aids by the International Union of Crystallography. His contributions to national Security by being a member of Pokhran I & II teams, particularly to the development of the thermonuclear test device, would always be remembered in India. During his 42-year career in Bhabha Atomic Research Centre (BARC), he contributed immensely to the field of High Pressure Physics.

Dr. Sikka was a distinguished scientist and Director of Atomic and Condensed Matter Physics group of BARC. In 2002, he accepted the role of Scientific Secretary to the Principal Scientific Adviser to Government of India. Later, he came back to BARC for a short period (2010-2013) as a Homi Bhabha Chair Professor of the Department of Atomic Energy (DAE). During this brief period, he continued to enthuse several colleagues with his scientific insights and work.

Dr. Sikka was widely honored for his scientific contributions through several reputed awards, including Padma Shri, Fellowship of all the three National Science Academies, and the Lifetime Achievement Award of the Department of Atomic Energy.

Due to his spontaneous and supportive nature, he also endeared himself to many colleagues and friends. He will always be remembered by us and his other colleagues & friends for his enormous scientific contributions and his helpful nature.

May his soul rest in peace and God offer sufficient strength to his family members to bear this grievous loss.

**S. M. Sharma,** Former Director, Physics Group, BARC;
**R. Chidambaram,** Former Chairman, AEC & Former PSA to GoI.

This page is intentionally left blank

This page is intentionally left blank


Commemorative coin unveiled during the National Technology Day 2023 marking 25th anniversary of Operation Shakti.

Edited & Published by
Scientific Information Resource Division
Bhabha Atomic Research Centre, Trombay, Mumbai-400 085, India
BARC Newsletter is also available at URL:https://www.barc.gov.in